Study of Conventional Annealing and Laser Annealing of Vitreloy1b Zr-based BMG

UNIVERSITY OF BIRMINGHAM

by

JONATHAN PAVEY

A thesis submitted to

The University of Birmingham

for the degree of

MRes in the Science and Engineering of Materials

School of Metallurgy and Materials

University of Birmingham

Edgbaston Birmingham

B15 2TT

September 2013

PREFACE

The majority of the work presented in this thesis was carried out by the author in the Department of Metallurgy and Materials, The University of Birmingham, from September 2011 to September 2012, under the supervision of Dr I. T. H. Chang.

A small section of the experimental work (laser machining) was carried out by Professor Stefan Dimov's colleagues in the Department of Mechanical Engineering, Cardiff University.

The work presented within this thesis is original and where work has been drawn upon by others this has been acknowledged within the text. This work has not been submitted for any degree at this or any other university.

Part of the present work has been submitted as a conference paper to be presented at the 4M 2013 conference in Spain, 8th - 10th October 2013.

The title of this paper is *Laser machining of a Zr-based bulk metallic glass with nano-second laser* and its authors are Pavey, J., Penchev, P., Dimov, S., Chang, I., Petkov, P., and Kolew (to be published in 4M 2013 conference proceedings).

ABSTRACT

The machining response of a Zr-based amorphous alloy ($Zr_{44}Ti_{11}Cu_{10}Ni_{10}Be_{25}$) when subjected to nano-second laser machining is investigated. The surface integrity of laser machined fields in two sets of experiments is studied using scanning electron microscopy (SEM) followed by subsequent X-ray diffraction (XRD) analysis to observe any phase changes. The study shows that the highly attractive short-range atomic ordering of the material can be preserved by optimizing the laser machining conditions. It was demonstrated that the surface roughness achievable after nano-second laser machining was comparable with that attainable in micro milling.

This thesis also investigates the effects of an additional annealing stage using two different techniques. Previous research has shown that when certain amorphous alloys are reheated into their supercooled liquid region, surface features can be erased under the action of surface tension forces [1]. This study performs annealing experiments using a hot plate setup as well as an in-situ hot stage microscopy setup. The results reveal that no subsequent erasure of features was seen for the Zr-based amorphous alloy and this is attributed to the fast oxidation rate associated with the alloy preventing a surface smoothening effect from occurring.

ACKNOWLEDGMENTS

I would first like to thank my supervisor, Dr Isaac Chang for his patience and dedication towards this project. His academic knowledge and guidance have been invaluable.

A special thank you goes to Professor Stefan Dimov from the Mechanical Engineering Department along with his colleagues from Cardiff University for their experimental work and outstanding knowledge on laser machining.

I would also like to acknowledge the excellent technical staff working within the Materials and Metallurgy department who aided me in my research work.

Finally, I would like to thank my family for their constant support and encouragement towards each and every venture I pursue.

CONTENTS

1. INTRODUCTION

In recent years metallic glasses have gained considerable interest due to their highly attractive combination of mechanical properties including high hardness, fracture toughness and fatigue strength [2, 3]. Additionally, the amorphous nature of these materials means they lack any long range atomic ordering, lattice defects and grain boundaries making them promising materials for producing micro/nano-scale components used in MEMS (micro-electro-mechanical systems) and microsystems [4].

To benefit from the superior properties exhibited by metallic glasses, it is of prime importance to maintain their short-range atomic ordering during processing. Various thermoplastic forming (TPF) processing methods have been developed including compression and injection moulding [5, 6], blow moulding [7], extrusion [8, 9], miniature fabrication (hot embossing) [4, 6, 10-13] and write/erasing [1, 14].

The surface roughness of metallic glasses is expensive to control, particularly for micro/nano devices where the surface roughness is of primary importance [15]. A recent study by Kumar and co-workers showed that the surface roughness of a Pt-based amorphous alloy could be smoothed following annealing due to surface tension forces alone [1]. This process has potential for producing ultra-smooth master moulds and for re-writable storage data; however further research using other BMG formers would be beneficial.

Also of current interest is the machinability of metallic glasses. It has been shown that traditional machining methods produce defects such as crystallisation, burr, and spatter

[16]. However the use of unconventional machining methods such as ultra-short pulsed laser ablation (eg pico-second and femto-second) have been effectively used without triggering crystallisation and with negligible heat affected zones (HAZ) [17-21]. This type of processing is very expensive and therefore in order to broaden the usage of laser machining for micro structuring metallic glasses, research should focus on the use of nano-second (ns) and micro-second (ms) pulses which are financially more cost effective and also associated with higher material removal rates [18].

1.1 Aims of Thesis

The aim of this thesis was to validate a process for producing bulk metallic glasses with ultra-smooth surfaces, whilst maintaining the highly desirable amorphous structure. The first part of this thesis explored structuring the surface of a Zr-based alloy using nanosecond laser ablation.

The second part of this thesis attempted to smooth the surface of a Zr-based alloy by surface tension forces using two different annealing techniques.

1.2 Objectives

1. To perform nanosecond laser machining to the $Zr_{44}Ti_{11}Cu_{10}Ni_{10}Be_{25}$ alloy without triggering crystallisation of the amorphous structure.
2. To perform annealing experiments at a range of times and temperatures to produce a smooth surface whilst avoiding crystallisation of the amorphous structure.
3. To characterise the BMG samples before and after annealing using XRD analysis, SEM and Taylor-Hobson surface roughness measurements.

2. LITERATURE REVIEW

2.1 History of BMGs

The very first metallic glass was discovered by Duwez and co-workers in 1960 when they performed rapid quenching to $Au_{80}Si_{20}$ which resulted in an amorphous structure [22]. They found that when the alloy was cooled at very high rates of 10^5-10^6 K/s this allowed for crystallisation to be bypassed. This discovery prompted the beginning of research on the formation of metallic glasses and the search for compositions with high glass-forming abilities. A few years later in 1969, Chen and Turnbull showed that metallic alloys with a high ratio of glass transition temperature (T_g) to melting temperature (T_m) showed good glass-forming abilities [23, 24]. These early metallic glasses however showed limited applications and their production was restricted to thin ribbons and films.

In 1974, Chen made use of suction-casting methods to produce Pd-Cu-Si rods with a 1mm diameter using a cooling rate of just 10^3 K/s [25]. Within the literature a metallic glass alloy capable of a critical casting thickness >1mm is termed a 'bulk' metallic glass (BMG). Thus, Chen and co-workers are considered one of the first to pioneer BMGs. Turnbull et al. predicted that the ratio between the T_g and the T_l (liquidus temperature) $T_{rg} = T_g/T_l$, could be used as a criterion to determine the glass-forming ability of an alloy[23]. Later in 1982, Chen and Turnbull revisited experimenting with the well-known Pd-Ni-P alloy and this time they found that by using boron oxide fluxing when the value of T_{rg} could reach 2/3 when the heterogeneous nucleation was suppressed, and they were able to produce bulky glass ingots of centimeter size at a cooling rate of 10 K/s [26, 27]. At the time, this research was perceived to be merely academic curiosity

and the huge potential of BMGs for widespread applications was not recognised. The rapid developments made in critical casting thickness for metallic glasses since their discovery in 1960 can be seen in figure 1.

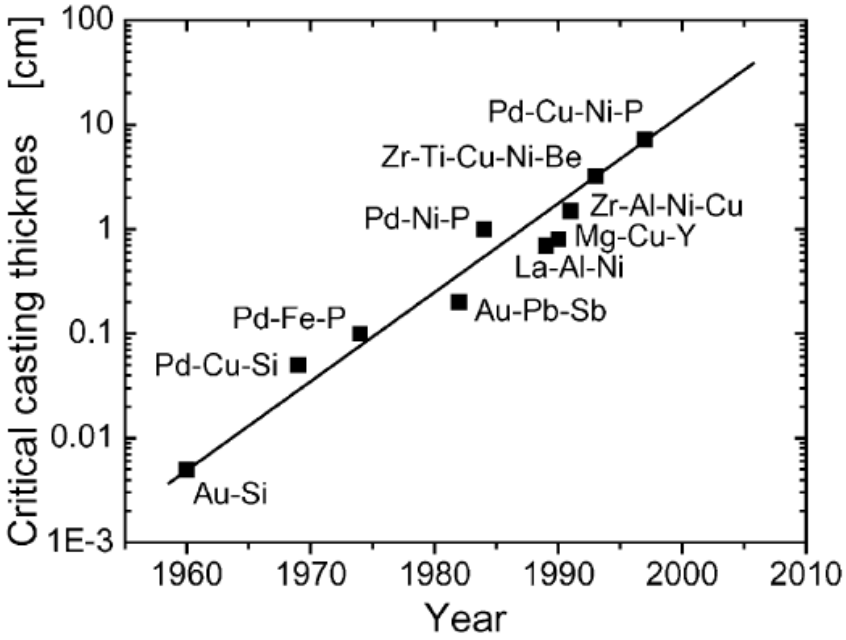

Figure 1. Developments in critical casting thickness for metallic glasses since their discovery in 1960 [7]

In the late 1980's the Inoue group at Tohoku University began to investigate with the use of various rare-earth materials alloyed with Al and ferrous metals. They reported exceptional glass forming abilities for BMG formers based on lanthanum [28], magnesium [29] and zirconium [30]. Also at this time, Johnson's group at Caltech were becoming increasingly interested in the prospects of using BMGs for engineering applications. They developed a range of ternary and quinary alloys based on higher order alloys including Zr, Ti, Cu, Ni, Be. In 1993, the Johnson group developed the quinary alloy $Zr_{41.2}Ti_{13.8}Cu_{12.5}Ni_{10}Be_{22.5}$ $[(Zr_3Ti)_{55}(Be_9Cu_5Ni_4)_{45}]$ which was reported as one of the first metallic glass with a relative casting thickness of several centimetres

[31]. This alloy has since become one of the most studied BMGs and is known industrially as Vitreloy 1 (Vit1).

Over the last two decades a wide range of BMGs have been discovered including Fe-based [32, 33], Pt-based [34], Ti-based [35, 36], Cu-based [37, 38], Ca-based [39], Ce-based [40], Mg-based [41, 42] and Au-based alloys [5, 43]. Recently, the research direction on BMG, has moved away from producing BMGs with high critical casting thicknesses and instead towards improving properties such as strength, plasticity and low temperature formability. These developments are expected to provide a new range of applications for BMGs in the future.

2.2 Glass-forming ability of bulk metallic glasses

Since their discovery, most of the research into BMGs has focused on their thermophysical properties such as viscosity, relaxation, diffusion as well as their thermodynamic properties. Until recently studies were unable to report on findings within the supercooled liquid region (SCLR) which is the region between the glass transition temperature (T_g) and the crystallisation temperature (T_x). This was due to a lack of thermal stability in the SCLR with respect to crystallisation which meant research was limited to temperatures below or in the vicinity of the T_g.

However, novel BMG-forming liquids have enabled researchers to study the behaviour of BMGs using much broader times and temperature ranges. Consequently it is possible to study the formation of BMGs using time-temperature-transformation (TTT) diagrams such as that shown in figure 2 for Vitreloy 1 [44] .

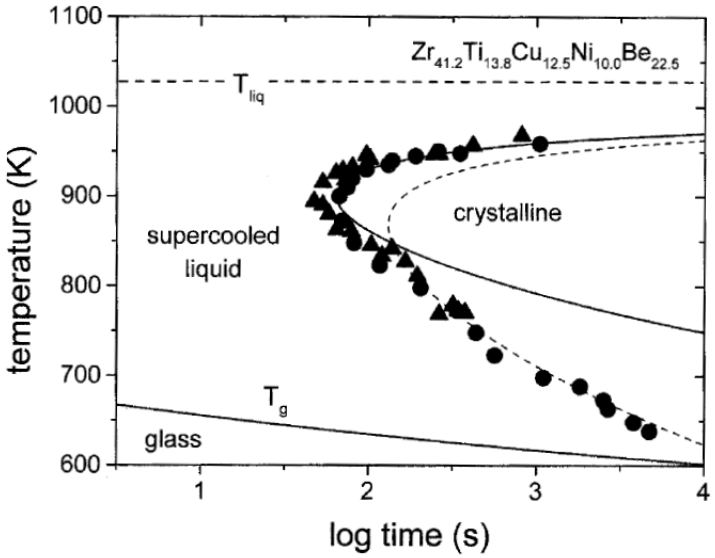

Figure 2. TTT diagram for the crystallisation of Vitreloy 1. [44]

The amorphous phase is produced when the nucleation and growth of the crystalline phase is suppressed by rapid cooling of the liquid melt. The C-curve seen in figure 2 represents the competition between the increasing driving force for crystallisation and the slowing of kinetics (effective diffusivity) of the atoms. The driving force is controlled by the degree of undercooling from the liquidus temperature, and the kinetics are controlled by the annealing temperature. So at the high temperature range, the onset time for crystallisation is long, this is due to a lower driving force resulted from small degree of undercooling. Whereas at the low temperature, the onset time for crystallisation is also long due to the slow kinetics at lower annealing temperatures. The nose of this TTT curve signifies where crystallisation occurs fastest because of the combination of a large driving force and high atomic mobility. This must be avoided at all times if the material is to remain amorphous. Rapid quenching of the liquid melt allows the alloy to bypass the curve and eventually become frozen in a random

disordered atomic configuration. This metastable solid state is known as the glassy state.

Assuming steady-state nucleation, the nucleation rate can be determined by the product of the thermodynamic contribution (driving force for crystallisation) and the kinetic contribution (diffusivity or viscosity) as

$$I_s = A \cdot D_{eff} \exp(-\Delta G^*/kT) \quad (1)$$

where T is temperature, k is the Boltzmann's constant, ΔG is the activation energy, D_{eff} is the effective diffusivity and A is a constant. Based on these considerations, the glass forming ability (GFA) of BMGs can be put down to understanding the thermodynamic, kinetic and structural factors [44].

Several theories have been proposed in order to understand the GFA of BMGs. Turnbull suggested that for glass formation to occur and for the material to remain amorphous, the ratio between the T_g and the liquidus temperature (T_l) must be equal to or greater than 2/3 [45]. This ratio is often referred to as the reduced glass transition temperature (T_{rg}). The criterion suggests that for such a liquid its crystallisation will be sluggish meaning crystal nucleation will be suppressed as a result of a lower driving force for nucleation.

Inoue and co-workers proposed another theory consisting of three empirical rules needed to achieve high GFA [46]. They suggested that alloys satisfying each empirical

rule have different atomic configurations in the liquid state compared to those of the corresponding crystalline phases.

These rules are as follows-

1. Multicomponent alloy systems consisting of three or more elements

2. Significant difference in atomic sizes between the constituent elements with size ratios greater than 12%

3. Negative heats of mixing among the main constituents, i.e. the materials have a strong affinity with one another

Furthermore, Greer predicted that the GFA of BMGs increases with the addition of more elements [47]. Known as the 'confusion principle' this theory suggests that a larger number of elements within the alloy system destabilizes the competing crystalline phases, therefore the tendency for crystallisation.

2.2.1 Thermodynamic aspects

When a melt is cooled below its liquidus temperature (T_l) an increase in the driving force for crystallisation is observed. This can be approximated by the Gibbs free energy difference (ΔG) between the supercooled liquid and the crystal. Generally it has been shown that high GFA is achieved by small values of ΔG. These values can be determined by integrating the specific heat capacity difference between the SCL and crystal and considering the effects of the fusion heat.

2.2.2 Kinetic aspects

In terms of kinetics, viscosity is considered the key parameter that determines GFA. The equilibrium viscosity data can be measured using the Vogel-Fulcher-Tammann (VFT) equation [48]

$$\eta = \eta_0 \cdot \exp[D^* \cdot T_0/(T - T_0)] \quad (2)$$

where η is the viscosity and the pre-exponential factor η_0 is the viscosity at infinite temperature which is kept fixed at a value of 4×10^{-5} Pa s. The D* parameter represents the kinetic fragility of the material and T_0 is the temperature at which the barriers with respect to flow would reach infinity [48]. It has been shown that the melt viscosity is approximately three orders of magnitude greater for BMGs in comparison to pure metals [49]. During cooling, increases in the viscosity decrease the mobility observed in the supercooled liquid state. Therefore sluggish kinetics are observed for BMGs leading to retarded crystal nucleation and growth kinetics.

2.3 Properties

The material properties of BMGs are defined by their structural arrangement. In comparison to conventional metals which display an orderly crystalline arrangement, the atoms within BMGs are randomly arranged. This structure, known as amorphous, results in superior properties to conventional metals [49].

BMGs have no grain boundaries or crystal defects such as dislocations, and consequently they do not deform in the same manor to crystalline metals [49]. Instead upon yielding they deform by shear localization which leads to the formation of shear

bands. These bands are typical narrow approximately 10 nm thick [50]. Heat is generated by the high shear rate which causes the bands to dilate leading to a low shear resistance and higher shear rate. This mechanism usually occurs along one dominant shear band and can result in catastrophic failure [51-55]. However, research has shown that when using BMGs on small scales significant global plasticity is observed and catastrophic failure is avoided [56, 57].

BMGs have a unique combination of properties including enhanced strength, toughness, elasticity and corrosion resistance [2, 3]. It is not uncommon for the strengths of BMGs to be 2 or 3 times greater than their crystalline counterparts for example titanium has an approximate strength of 790MPa where as a Zr-based alloy produced by liquidmetal technologies has reported strengths of 1900MPa. The characteristic mechanical properties associated with the Zr-based alloy Vitreloy 1 are shown in table 1[58, 59].

Table 1. Mechanical properties of Vit1 [59]

Property	**Value**
Elastic strain limit, ε_{el}	2%
Tensile yield strength, σ_y	1.9 GPa
Young's modulus, Y	96 GPa
Shear modulus, G	34.3 GPa
Poisson's ratio, v	0.36
Vickers hardness	534 kg/mm^2
Fracture toughness, K_{1c}	55–59 MPa m$^{1/2}$
Thermal expansion coefficient	10.1×10^{-6} K^{-1}
Density	6.11 g/cm^3

2.4 Processing of BMGs

Two principally different processing methods exist for BMGs. The first method is direct casting, a commonly used net-shaping technique for conventional metals, although

certain limitations exist for the production of BMGs [6]. Alternatively BMGs can be processed via TPF. This process involves reheating BMGs into their SCLR where they exist as highly viscous metastable liquids. These high viscosities enable BMGs to experience considerable plastic strain under applied pressure, thus enabling processing routes similar to plastics to be used [6, 60].

The main challenge when processing BMGs by direct casting or TPF is avoiding crystallisation. This can only be achieved by choosing appropriate cooling and heating paths which could introduce crystallisation. To avoid crystallisation, heating and cooling paths must be selected which avoid the crystallisation curve shown in figure 3 [6]. Path 1 in figure 3 indicates the slowest cooling rate used to avoid crystallisation; critical cooling rates equal to or faster than this represent paths used for direct casting, operated from a temperature above Tx. Path 2 on the other hand indicates the path used for TPF processes operated from a temperature below Tx, where fast cooling and forming are decoupled. Path 2 benefits from a much longer processing window which results in improved control over the process. Furthermore, the availability of slow cooling can eliminate internal stresses, enabling components to be produced with high dimensional accuracy and complex geometries [6].

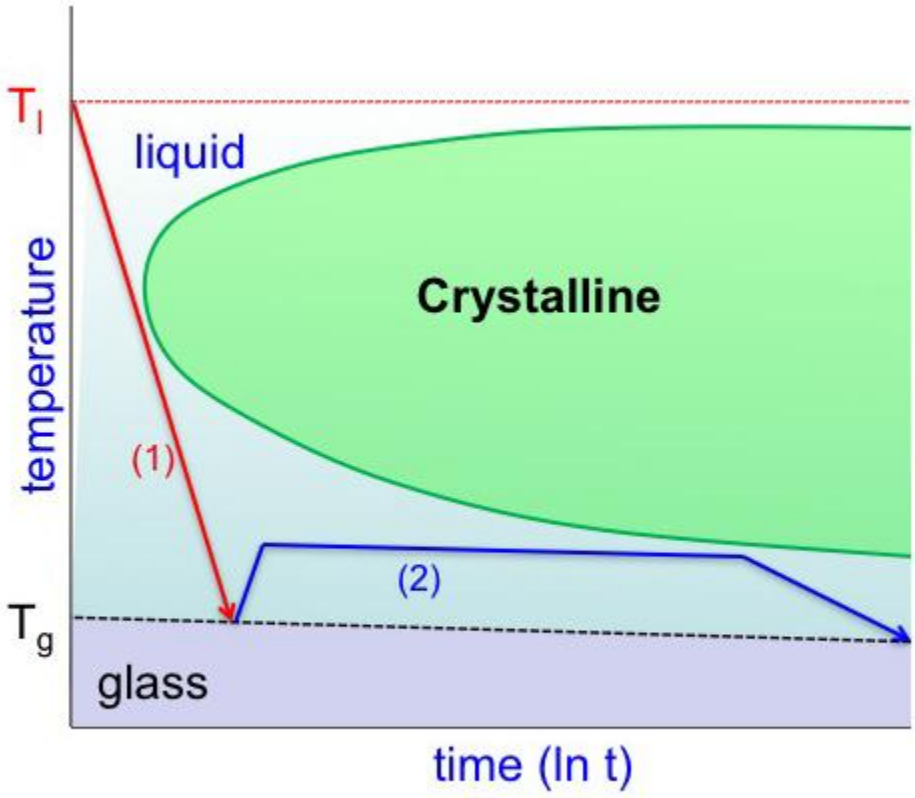

Figure 3. Schematic time-temperature-transformation for BMG formers. Path 1 shows the cooling paths used for direct casting. Path 2 indicates the two-step process where fast cooling and forming are decoupled used for TPF **[6]**

2.4.1 Direct Casting

In order to produce good quality castings, slow cooling and small temperature gradients are required. However in order to avoid crystallisation during direct casting fast cooling and forming must be performed simultaneously. These contradicting practices therefore require a careful balance of processing parameters including casting temperature, mould temperature and mould design in order to produce a high quality castings [60]. As a result it is particularly difficult to produce complex geometries using direct casting [5].

There are two main casting methods which have been used as net-shape processes to fabricate BMGs; suction and die casting. Inoue and co-workers showed that the fabrication of a Zr-based alloy via suction casting could produce high quality parts with

low porosity, compared to its die cast counterpart which showed a higher porosity [61]. Die casting on the other hand benefits from its ability to be scaled up for the mass production particularly for small and medium sized parts. Liquidmetal Technologies are one company who currently use die casting to mass produce Zr-based parts such as electronical casings for phones, camera and flash drives [60].

There are several benefits when using the casting to process BMGs, these include the low melting temperatures associated with BMGs which reduce tooling costs and decrease production times [62]. Additionally, studies have reported as low as 0.4% shrinkage for Zr-based amorphous alloys following casting as opposed to typical shrinkage of approximately 5% for conventional alloys [6]. Schroers summarized the advantages and disadvantages based on direct casting methods shown in table 2.

Table 2. Advantages and disadvantages of the use of direct casting for BMGs [62]

Advantages of Direct Casting	Comment	Disadvantages of Direct Casting	Comment
Low melting temperature	Composition dose to eutectic composition	Cooling and forming are coupled	Metastable nature of BMG fast cooling
Low shrinkage		Processing environment	
	Absence of first-order phase transition during solidification	can influence crystallisation kinetic	Most BMGs are reactive and vacuum/inert conditions are
One-step process		High viscosity	required; costly high purity ingot materials
Homogeneous microstructure		Internal stresses	The low fluidity of BMG liquids makes casting more difficult
	No directional growth, no crystals, no intrinsic size limitation	BMGs contaminate during processing	The required fast cooling results in internal stresses
Mechanical properties are already mature in the as-cast state	No subsequent heat treatment		Limited reusability of material

2.4.2 Thermoplastic Forming

The ability to process materials in the SCLR region was first recognized in 1978 [63], but the technique was not fully utilised using BMGs until the discovery of BMGs which showed higher formability. Over the last 20 years a wide range of TPF methods have been used to processes BMGs including compression and injection moulding [5, 6], blow moulding [7], extrusion [8, 9], miniature fabrication (hot embossing) [4, 6, 10-13] and write/erasing [1, 14]. These methods have been used to produce BMGs with features on the length scale from 50nm to 5cm [6, 11, 60, 64].

All TPF processes use an amorphous BMG 'feedstock' material the form of which can vary. Such forms include powders, rods, disks, plates, and pre-shaped parisons [62]. All these feedstocks share one common feature in that they are exceptionally easy to cast using standard TPF methods. The forming of the feedstock is subsequently processed within the SCLR where the forming pressure is greater than the flow stress for the BMG. In most cases TPF of BMGs can be performed in air [6], which is a reflection of BMGs insensitivity to heterogeneous influences on the crystallisation within the SCLR. Figure 4 displays the temperature dependence of the crystallisation time and viscosity for Vit 1b characterized by the filling length. It can be seen that filling lengths increase with an increase in temperature. Additionally, as the temperature increases the viscosity decreases. Similarly as the temperature increases the material become more viscous. However higher temperature shorten the time before crystallisation occurs. The graph suggests that for maximum formability the highest possible temperature should be selected whilst avoiding crystallisation [6].

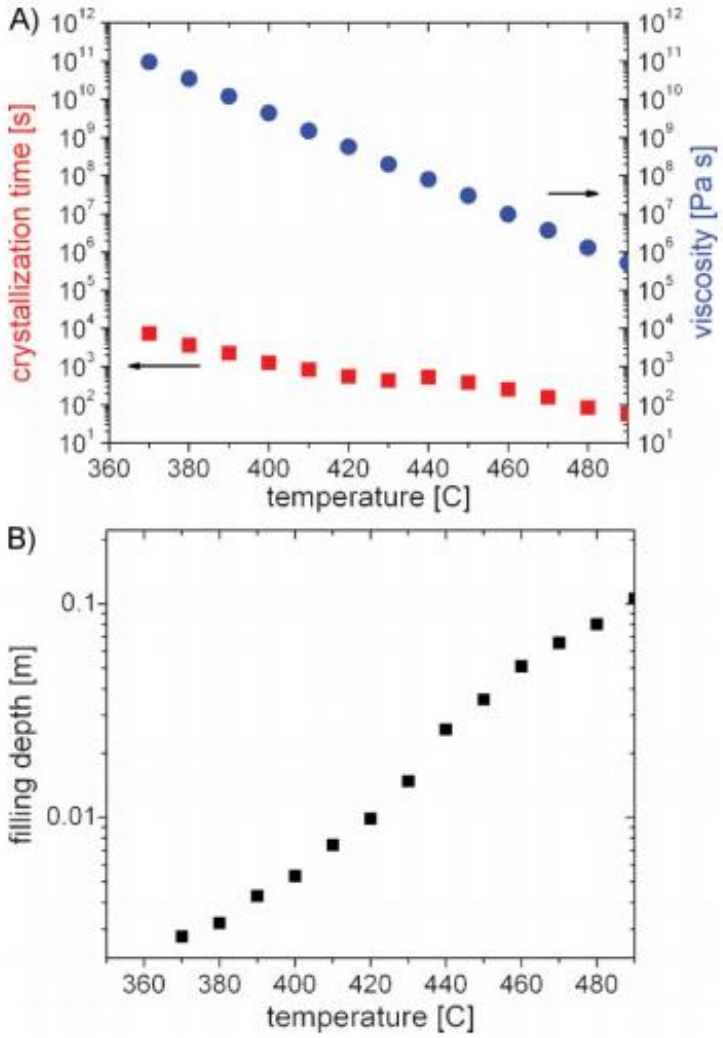

Figure 4A. TTT diagram showing the onset time for crystallisation and the temperature dependent viscosity for Vit1reloyb. **Figure 4B.** Shows the filling length as a function of temperature indicating isothermal formability. Figure 4 is taken from [62] who reproduced the graphs with permission from [65, 66]

Table 3. Advantages and disadvantages based on TPF methods [62]

Advantages of TPF-Based Processing Casting	Comment	Disadvantages of TPF-Based Processing Casting	Comment
Forming and fast cooling decoupled	Wide range of complex shapes can be net-shaped	Two- or more- step process	A requirement from the decoupling of cooling and forming
Highest dimensional accuracy	Due to negligible stresses and negligible solidification shrinkage		
Insensitive to heterogeneous influences	Predictable and robust process. Allows to process in air		
Novel and unique process 'green' process	Due to low processing temperature and pressure, ability to net-shaping	Novel and unique process	Requires the development of novel processing methods
Low capital investment	Also allows small series and custom shaped parts		

2.4.2.1 Compression moulding

Compression moulding is commonly used for plastic processing but has recently been used for net shaping BMGs. [6] The process involves placing a BMG feedstock material into a mould and reheating it into the SCLR. There is a time/flow stress trade-off when selecting the forming pressure. The pressure must be greater than the flow stress in order to achieve the required strain before the onset of crystallisation. Figure 5A shows a schematic illustration of the compression moulding process.

Compression moulding has been performed using $Pt_{57.5}Cu_{14.7}Ni_{5.3}P_{22.5}$[6] and $Au_{49}Ag_{5.5}Pd_{2.3}Cu_{26.9}Si_{16.3}$[5] as feedstock materials. Both were in the form of particles with diameter of approximately 1mm. It was shown that the compacted parts exhibited mechanical properties close to that of the original metallic glass and good dimensional accuracy and surface finish were achieved. Perfect replication of features measuring 4μm thick and 12μm long has been performed, these protrusions also showed features

of approximately 100nm which were replicated from the original mould [6]. Figure 5B shows $Pt_{57.5}Cu_{14.7}Ni_{5.3}P_{22.5}$ pellets used as the feedstock material.

It is important to choose the correct moulding pressure when performing compression moulding. The pressure not only depends on the formability of the BMG in the SCLR but the geometry of the final part [62]. An example of this can be seen in figure 5C which has a thickness of 1mm and was processed using a forming pressure of 250MPa whereas figure 5D shows a thickness of 3mm and was processed at 20MPa.

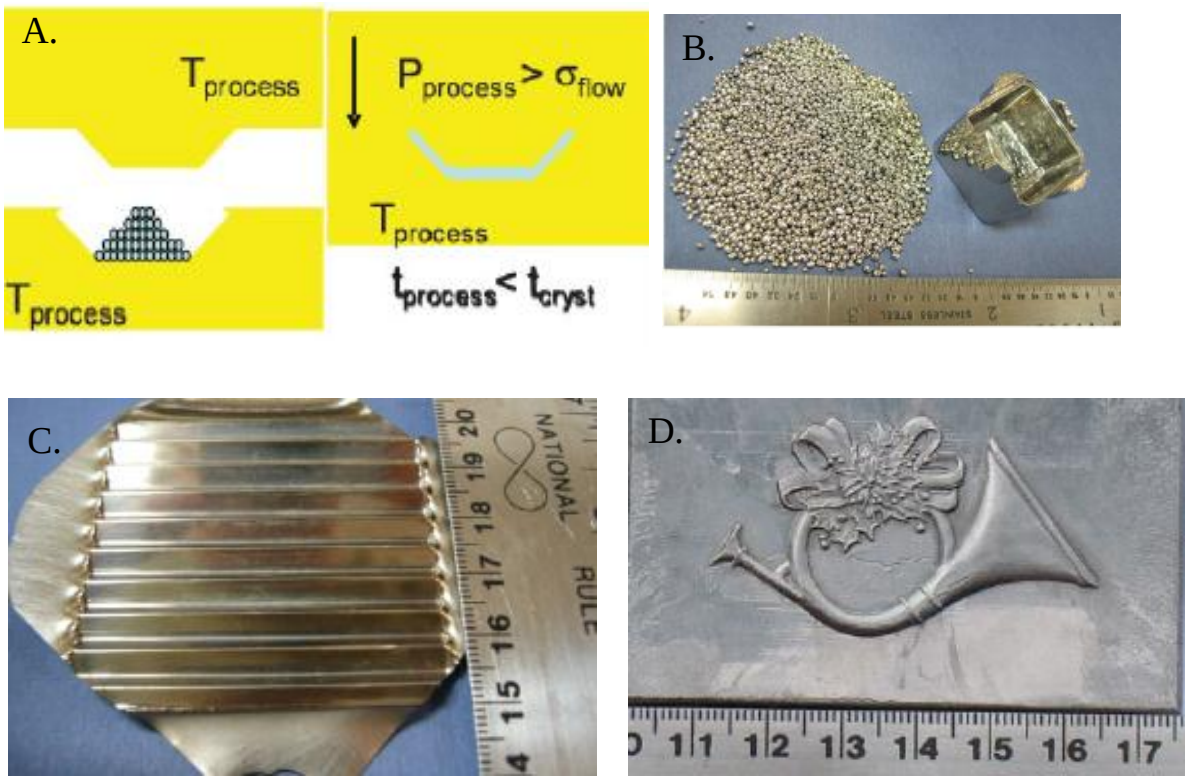

Figure 5. Compression moulding BMGs A. Compression moulding process B. BMG pellets used as feedstock material C. Vitreloy1b specimen formed from a flat sheet into a corrugated structure D. A Vitreloy1b embossing mould with pattern design created from a flat sheet [62]

2.4.2.2 Miniature fabrication

Advancements in miniature fabrication over the last 20 years has led to particularly interest in producing micro-electromechanical systems (MEMS), medical devices and complex electronic devices. As discussed, BMGs benefit from a homogenous and isotropic structure, an excellent combination of mechanical properties over conventional materials and the opportunity to produce stress-free components. Consequently, significant attention has been given to developing ways to fabricate miniature BMG components of which the process is described below.

2.4.2.2.1 BMG formers for miniature fabrication

In order to choose a BMG former for miniature fabrication it is important to consider various processing characteristics, including the thermoplastic formability, moulding temperature and certain properties which may be needed for specific applications such as strength and elasticity [67]. The forming ability of a BMG in its supercooled liquid state is given by its temperature dependence of viscosity and crystallisation time. Schroers produced an accurate way of assessing the thermoplastic formability which also takes into account the wetting behaviour between the BMG and mould[68]. The method involved heating a fixed volume of BMG through its SCLR whilst under a constant load of 4500N. This gave a reading of the diameter of the disc, termed d, which is used as the measure of formability. Alloys with particularly high formability include $Zr_{44}Ti_{11}Cu_{10}Ni_{10}Be_{25}$ [65], $Pt_{57.5}Cu_{14.7}Ni_{5.3}P_{22.5}$ [34] and $Au_{49}Ag_{5.5}Pd_{2.3}Cu_{26.9}Si_{16.3}$ [43]

2.4.2.2.2 Micro-moulding Process

Figure 6 depicts the basic principle of TPF-based miniature fabrication for BMGs. [67] A hard mould is first chosen; commonly silicon however other mould materials include

nickel, steel, alumina, carbon and some high-temperature polymers. These moulds have the desired pattern on them often created using lithography (liga), electro-plating or micromachining [69].

The moulds are then heated to the required temperature and the BMG is then placed on top and heated to a stable temperature[67]. Once the BMG has softened into a viscous liquid, pressure is applied to force the BMG into the mould pattern. It is important to minimize temperature variations during fabrication as these can affect the viscosity. For this reason the system should be well insulted to prevent any unwanted variations. Additionally, if an overshoot in temperature occurs the material may crystallize immediately degrading its mechanical properties and changing the flow behaviour of the material. The TPF temperature is chosen using the temperature dependence of viscosity and crystallisation time as shown in figure 4. Schroers suggests that if one wishes to achieve maximum formability it is best to choose the highest possible temperature for processing that will avoid crystallisation [6].

Following the micromoulding process the BMG can be removed by one of two methods. The substrate can either be separated using a chemical solution such as KOH or POH which etches away the silicon and results in a patterned substrate as shown in figure 6b. Alternatively, if 3D BMG microparts are required a hot scrapping method can be used [4]. This involves reheating the BMG back into the SCLR and then a sharp knife is used to remove the material outside of the mould. The mould is subsequently etched away leaving the 3 dimensional BMG microparts.

Saotome and co-workers were the first to practice miniature fabrication by TPF on a variety of BMG alloys including Zr-based [11], Pt-based [64], Pd-based [70] and La-based [71]. This work inspired many other research groups to investigate miniature fabrication through TPF. Studies have reported replication of features using this method on scales from down to 100nm [67]. Several studies have shown particular interest into BMGs which exhibit particularly high formability to produce components with high-aspect-ratio features; these alloys include $Zr_{44}Ti_{11}Cu_{10}Ni_{10}Be_{25}$, $Pt_{57.5}Cu_{14.7}Ni_{5.3}P_{22.5}$, and $Au_{49}Ag_{5.5}Pd_{2.3}Cu_{26.9}Si_{16.3}$ [5, 6, 60, 66].

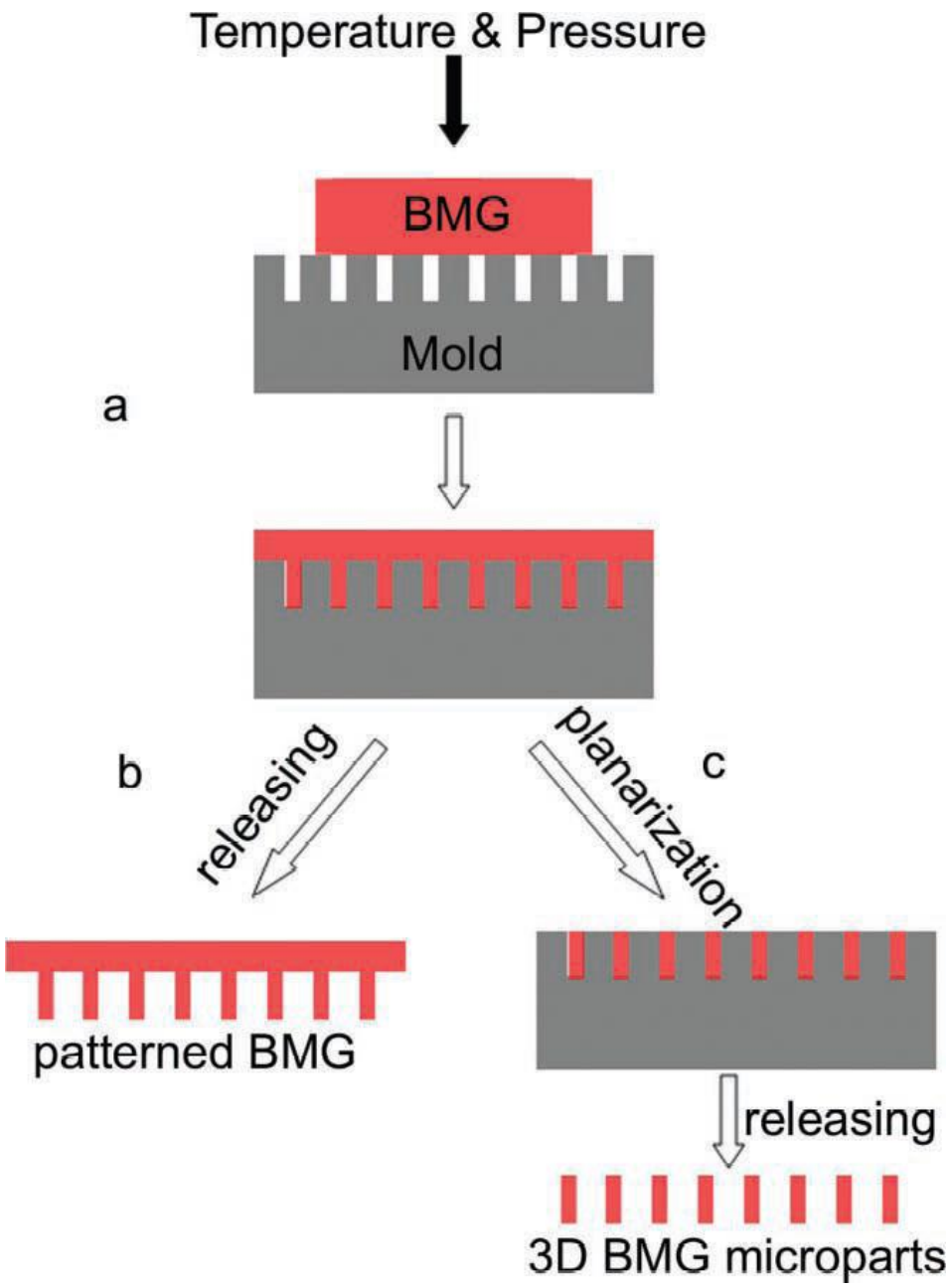

Figure 6. Diagram of the TPF micromoulding process. a) The BMG and mould are heated then pressure is applied and the viscous BMG fills the mould cavity b) Separating of the mould and BMG leaving surface features on the BMG surface c) Removal of the BMG layer by hot cutting or polishing producing 3 dimensional microparts [67]

2.4.2.3 Surface Finish

The attainable surface finish is always a concern when fabricating parts by micro- and nano-manufacturing. Planar polishing is one technique which can improve the surface finish, however, this method is not appropriate for non-planar geometries with recessed regions [67]. The surface finish of BMG components often depends on the mould surface. Although the patterning of commonly used metal moulds is limited by their finite grain size [69].

Kumar et al. [1] developed a self-smoothening process whereby miniature parts could be processed in a subsequent annealing step following the moulding process. They showed that when reheating a Pt57.5Cu14.7Ni5.3P22.5 into its SCLR the viscosity became sufficiently low for surface tension forces driven by viscous flow to have a smoothening effect to features on the surface without triggering crystallisation. The annealing time and temperature for this phenomenon must be chosen carefully so that dimensional accuracy is retained and crystallisation avoided. Figure 7 shows the results of the study showing initial microfeatures of 6μm which were almost fully erased following annealing at 270^{o}C for 1200s.

Kumar and co-workers developed a model to calculate erasing time t_e to the size of different surface features:

$$t_e = \frac{9nh_0}{\gamma} \tag{3}$$

where h_0 represents the initial height γ is the stress exerted by the surface tension and η is viscosity. This new concept has been linked with two main prospective applications, firstly for use as ultrahigh density re-writable data storage. Secondly, as a surface smoothening process for complex miniature parts [1]. This could considerably decrease the costs associated with mould making because less expensive moulds could be used during TPF.

Research published using this technique is currently limited to Pt-based alloys which show excellent formability[68]. Further studies should focus on applying this technique to other BMG formers such as Zr-based amorphous alloys.

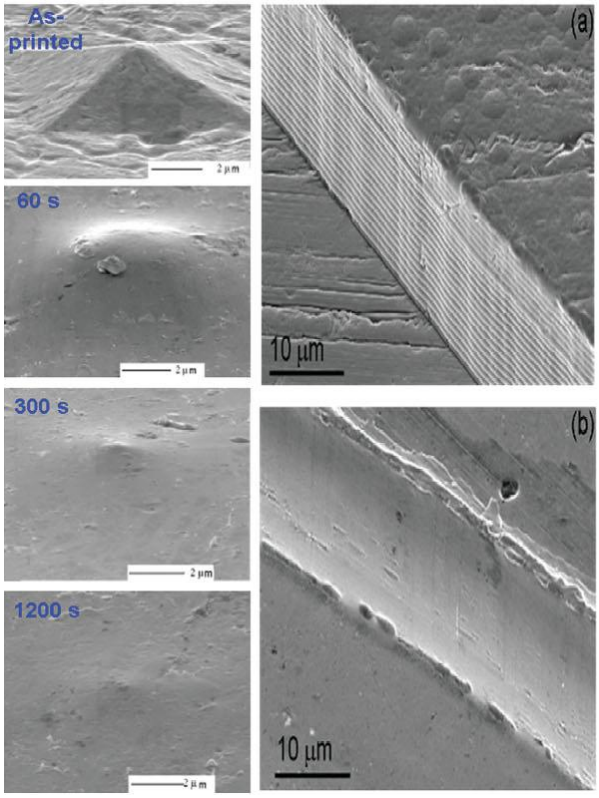

Figure 7. SEM images of microfeatures on a Pt-based amorphous alloy which have been smoothed by annealing in the SCLR [1]

The most commonly used measurement for surface roughness is the roughness average (Ra) sometimes known as the arithmetic mean roughness value (AA). It represents the arithmetic mean of the profile departure away from the mean line within a given sampling length (see figure 8) and is calculated using the following equation

$$R_a = \frac{1}{L}\int_0^L |Y(x)|dx \tag{4}$$

where L is the sampling length and Y is the ordinate of the profile curve.

Ra is a highly stable and repeatable parameter however does not give a true picture of the actual surface profile. This means that two surfaces with a very different surface profile can have the sample Ra value.

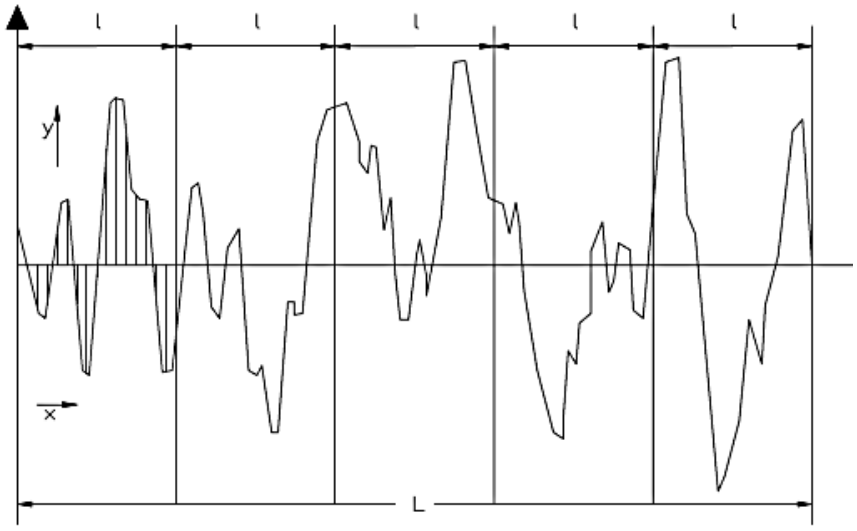

Figure 8. Profile of a surface showing the departure away from the mean line [72]

2.4.2.4 BMG as a mould material

BMGs fulfil all of the ideal requirements to be used as mould materials and therefore have grown in interest to be used as master moulds. These requirements include high strength, high hardness and the ability to be manufactured economically and precisely when used at temperatures below their T_g [62]. Besides from their excellent mechanical properties, BMGs are also intrinsically free from grain size limitations.

Figure 9 shows that BMGs have the ability to be used as mould materials at temperatures below T_g.

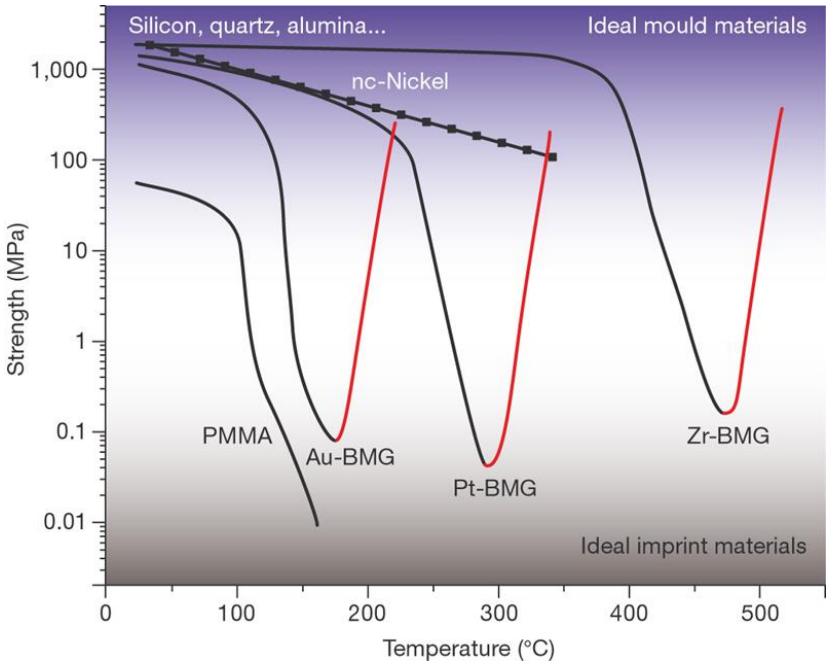

Figure 9. The temperature- yield strengths for various mould materials [69]

BMGs have also gained attention as potential mould inserts for injection moulding. Current micro-injection moulding techniques rely largely on steels to provide durability and strength however due to their inherent crystalline structure and grain size it is difficult to produce tools with small features.

Gilchrist et al [73] at University College Dublin performed micro injection moulding using a BMG insert to investigate the replication of micro and nanoscale features. The mould cavity comprised of a steel mould which was embedded with a BMG insert with the composition $Zr_{47}Cu_{45}A_{l8}$. Various submicron and nanoscale features were machined into the BMG insert using FIB, these included the University college Dublin logo.

The study analysed the loss of features on the BMG insert after roughly 10,000 and 20,000 moulding cycles. It was shown that after 10,000 cycles the BMG insert can retain precise features however after more than 20,000 cycles features deteriorate and can be destroyed. However, it should be noted that prior moulding trials had been performed using the mould and thus further work is needed to analyse the fatigue behaviour of BMGs under repeated heating and moulding trials.

This study shows that BMGs offer a huge potential for use as multi-scale tools. These master tools could be used as a method for fabricating high-volume, low-cost polymeric components for MEMS and information storage devices.

2.4.3 Machining

Applications such as MEMS and micro sensor systems require high dimensional accuracy. Thus similarly to direct casting and TPF when using machining methods to structure BMGs it is imperative to avoid micro-structural damage and intrinsic property change. It is particularly important to avoid crystallisation as the material will lose its unique set of properties.

When using conventional machining methods on BMGs such as cutting tools and laser machining with long pulses (longer than 10picoseconds) defects have been observed including crystallisation, burr (rough and random edges) and spatter (surface covered in droplets of material) [74-76]. Focused ion beam (FIB) is one conventional machining method which had shown the ablity to produce accurate machining on the nanometer scale whilst retaining an amorphous structure [77]. However, unfortunately FIB is also associated with low machining rates and in return high costs which make the process inappropriate for mass production.

In recent years the use of non-conventional machining processes in particular ultra-short pulsed laser ablation has drawn increased interest. Studies have shown that when processing various BMGs using by laser machining using femto-second (fs) and pico-second (ps) pulses the amorphous structure can be retained and result in negligible heat affected zones (HAZ) [17, 19-21]. These study show that short pulses preserve the amorphous structure because the irradiation time during each pulse is shorter than the electron cooling and lattice heating times for the BMG. The process is therefore carried out with almost no thermal effects, which prevents any changes to the microstructure. However, due to the high costs associated with ultra-short pulse lasers research in this area has been limited to laboratory research only.

As a result, research has been led towards the study of structuring BMGs with longer pulses within the nano-second (ns) and micro-second (μs) ranges where processing costs are much lower [18]. A longer pulse suggests a greater thermal load as the pulse energy is dissipated in the sample for much longer periods of time [17]. Therefore a

careful balance of processing parameters is required to avoid crystallisation. A large advantage exists for longer pulse durations (ns and µs laser ablation) in that much higher rates of removal can be achieved.

Some initial research has suggested that longer pulse durations are a promising technique towards micromachining BMGs. It has been showed that when performing µs laser ablation onto a Ni-based BMG they were able to avoid crystallisation and preserve the attractive mechanical properties [17]. Further research is needed to explore the use of ns and µs laser ablation for other BMG formers.

2.4.3.1 Pulsed Laser Micromachining

The process of pulsed laser machining uses computer-aided design (CAD) software to design the 3D surface profile which is fed to the laser. There are several advantages of this process including its ability to access areas deep within cavities and there are no issues of tool breakage and collision checking is not required [78].

Material is removed using a series of pulses which have a predetermined pulse length (duration) and repetition rate (frequency). High peak powers occur caused by the large amount of energy released in relatively short time periods. The laser ablation removes the material layer by layer until the desired 3D structure is produced. The choice of laser source is linked directly to the resulting surface integrity. Laser pulse durations range from µs to a few fs [78]. Recently fs and ps laser ablation has become commercially available and as mentioned above these methods have been used to structure various BMGs. Future research should however focus on the development of ns and µs laser ablation ranges due to their lower cost [18].

2.5 Applications

The attractive properties of BMGs make them suitable towards a large range of applications. Their ability to store large amounts of elastic energy makes them an ideal material for springs[79]. Also, the ability to return this elastic energy has led to their use in several sporting applications. Golf clubs and tennis rackets are some of the goods currently available, produced by Liquidmetal Technologies in California, USA [80]. Additionally, the high yield strength associated with BMGs is beneficial to almost all applications and has offered a whole new generation of materials for the application of aircraft, automobiles and medical applications at operating temperatures below T_g.

The drawbacks associated with BMGs include their brittle nature, high cost and processing difficulties. However, these can be overlooked when using them in miniature scales <1cm[67]. As a result BMGs lend themselves to miniature components such as micro electromechanical components (MEMS), biomedical devices, implants, RF dielectric switches, sensors and actuators.

Kumar and Schroers suggest that BMGs have the potential to be used in ultra-high density re-writable data storage. A current method for this is IBM's "millipede" system which utilizes a polymeric material, usually PMMA [81]. However, metallic glasses may be used as an alternative substrate material, since they possess a much higher thermal conductivity and possess the opportunity for surface tension-driven shape-recovery which may be used as a novel erasing mechanism [1]. Kumar and Schroers also suggest that the surface driven phenomenon provides the opportunity to precisely

control the dimensions of intentionally produced featured BMG surfaces on the micron-scale.

3. EXPERIMENTAL METHODS

The experimental research conducted in this study is split into two areas. The first area investigates the machining response of Vitreloy1b to nano-second laser machining and the second area studies the response of Vitreloy1b to annealing runs.

3.1 Material

The material used throughout this project is a Zr-based amorphous alloy, $Zr_{44}Ti_{11}Cu_{10}Ni_{10}Be_{25}$. The alloy was supplied by Liquidmetal Technologies and is commercially known as Vitreloy1b or LM1B. The material was received in sheet form with a 3mm thickness. The SCLR of a material can be defined as the temperature between its glass transition temperature T_g and crystallisation temperature T_x. The T_g for Vitreloy1b is 350^{o}C and the T_x is 471^{o}C [68].The mechanical properties of this alloy are particularly high for example its tensile yield strength is 1.9 GPa and its hardness is 540 Hv, making it attractive for producing high performance components [59].

3.2 Laser machining (laser annealing) of BMG

In order to investigate the machining response of the Vitreloy1b alloy to nano-second laser machining, two sets of experiments were conducted using laser machining. The process involves fast heating and quick cooling and therefore explores the kinetic element of crystallisation associated with BMGs.

Initial trials were used to optimise laser machining settings and to produce samples with as high as possible surface integrity. The best three settings were chosen and these were selected to conduct the first set of experiments. Square samples measuring 30x30 mm were cut from the as received material using wire electric discharge machining (EDM)

as described in the next sections. These samples were used to process three fields (the area which has been laser machined) with different surface roughnesses each measuring 10x10 mm. These were large enough so that material characterisation could be performed.

The results from the first set of experiments were subsequently used to create a further eight laser machining settings for the second set of experiments. The aim of these experiments was to obtain as high as possible surface integrity while eliminating any undesired effects of laser machining on the non-crystalline morphology of the Vitreloy1b amorphous alloy. Again, all eight fields were sufficiently large for characterisation processes to be performed

An SPI laser machine made in Southampton, UK was used for all processing. The laser system integrates a MOPA-based Yb fiber laser with a central wavelength of 1065 nm. The maximum average power of this laser source was 20W and its maximum repetition rate was 500 kHz. The pulse duration could be varied in the range from 20 to 200 nanoseconds. A 100 mm F-Theta lens was used to conduct the machining trails with the laser spot size of 45 µm. All machining was carried out at Cardiff University, School of Mechanical Engineering under the supervision of Professor Stefan Dimov's group.

3.3 Hot plate annealing (conventional annealing) of BMG

In order to investigate the response to conventional annealing, two Vitreloy1b samples processed by the first set of laser machining trials were heated to a temperature within the SCLR. This method involves slow heating and slow cooling and thus coincides with the thermodynamic element associated with the crystallisation of BMGs.

A Fast Heat Cube with ceramic band heater attachment with height 65 mm was wrapped around a mild steel block which measured 125 mm height and 80 mm height. The steel block was heated to the desired temperature within the SCLR (specifically 380^{o}C and 450^{o}C) and then allowed to equilibrate for 5 minutes. The temperature across the surface of the block was measured throughout using a thermocouple. BMG samples were then positioned onto the surface of the block for the desired time. Following each annealing run the BMG samples were removed and placed onto a steel block which was half submerged in a water bath to allow fast cooling. The hot plate annealing setup is shown in figure 10.

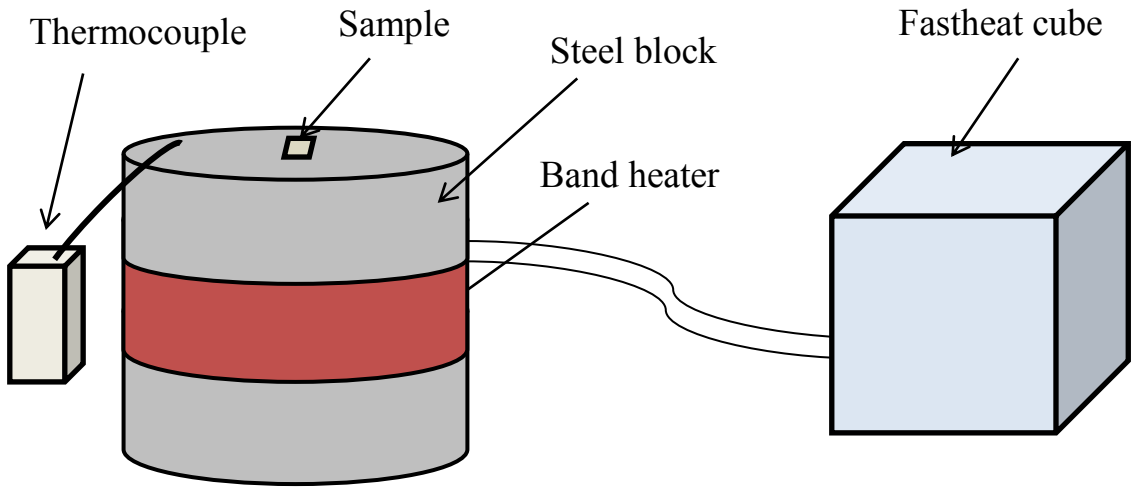

Figure 10. Schematic of the hot plate annealing setup

3.4 Vitreloy1b preparation before in-situ hot stage microscopy

3.4.1 Mould preparation

Commercial grade aluminium sheet from Birmingham University Metallurgy workshop with a thickness of 3 mm was cut into 10x10 mm squares using a manual sheet cutting machine. Samples were then ground using 1200 fine paper and polished using 6µm diamond suspension paste and finished with 0.5 µm polishing using colloidal silica. Each sample was then indented with a single indent using either Vickers hardness or mircohardness to produce a range of different sized indents. The loads used were 10kg, 1 kg, and 0.05 kg.

3.4.2 Cutting and polishing BMG for embossing

BMG samples with a thickness of 3 mm were cut using wire (EDM) to dimensions 5x5 mm. The machine used was an Agiecut Vertex made by Agie and the wire used was made from zinc coated in brass with a 0.1 mm diameter. The technology used for the machining was set to that similar for steel components with a thickness of 5 mm.

Grinding disks manufactured by Struers were then used to grind and polish the BMG alloy. MD-Primo, MD-Allegro and MD-Largo with a 6 µm suspension paste were used. Finally the BMG samples were finished with 0.5 µm polishing using colloidal silica.

3.4.3 Hot Embossing

The Vitreloy1b samples were embossed onto the aluminium moulds with the various indents using the TPF process hot embossing. The process was carried out in air at 440^{o}C under an applied pressure of 10 MPa for 100 seconds. A 125 mm diameter steel block with height 80mm and a punch diameter of 20 mm was used. The steel block was heated to temperature using a Fast Heat Cube with ceramic band heater attachment.

Once the samples were removed they were placed onto a steel block which was half submerged in a water bath to allow fast cooling.

3.5 Material Characterisation

3.5.1 Surface Topography

A Joel JSM 6060LV scanning electron microscope was used to observe changes in the surface features produced by laser machining. The secondary electron imaging mode was used to view the surface topography using magnifications of x1000 and x2500. The accelerating voltage was 20kV and the spot size varied from 8 to 15 nm.

3.5.2 X-ray Diffractometry (XRD)

XRD analysis was used in this work to observe if any crystalline phases were created following laser machining. An Inel Equinox 3000 machine was employed to characterise the laser machined area over a range of 2θ between 0-115^{o}C CuKa radiation with a Ni filter.

3.5.3 Surface Roughness

The roughness measurements were carried out using a Taylor-Hobson Talysurf 120 L Surface Texture Instrument. Sampling lengths of 0.8 mm and evaluation lengths of 4 mm were used for both 2D and 3Danalysis. Each measurement was taken 3 times and then an average was calculated.

3.5.4 Thermal analysis

A Netzsch differential scanning calorimeter was used in this study under an argon environment. A 15mg sample was placed in an alumina pan and heated at a rate of 10 K/min from 300^{o}C to 600^{o}C. Using computer software extrapolation lines from the dynamic heating trace were mathematically calculated to find the T_g and T_x.

3.5.5 In-situ hot stage microscopy

The samples used for in-situ hot stage microscopy were created as described above. The high temperature microscopy was performed using a Metallux 3 optical microscope with a Linkam TMS90 hot stage. A x50 lens and a x25 objective lens were used alongside an infinity 2 camera which was used to capture images approximately every minute. A water cooling system was employed together with a nitrogen flow in order to avoid overheating of the hot stage. Each run used heating and cooling rates of 50^{o}C per minute and the maximum temperature for these experiments reached 450^{o}C. The duration of each experiment varied with the longest being 10minutes and the shortest at 8minutes.

4. RESULTS

4.1 Laser machining

4.1.1 First set of laser machining trials

The laser settings used to conduct the first set of experiments onto the Vitreloy1b alloy are shown in Table 1. The selection of these initial parameters was based on some previous research using the same material. The research did not look at the effects of laser machining on crystallisation instead it focused on achieving a surface roughness Ra as low as possible. Unfortunately this research has not been published. Due to the time constraints of this study it was decided to use similar parameters as a starting point to assess surface roughness and the effects on crystallisation.

Table 4. Laser machining parameters for the first set of experiments

Parameters	Units	Field		
		1	2	3
Power	W	0.72	1.45	0.72
Repetition rate	kHz	40	250	40
Pulse Energy	µJ	18	5.8	18
Scanning speed	m/s	0.6	1	0.2
Fluence	J/cm^2	1.87	0.60	1.87
Track distance	µm	15	6	5
Layer thickness	µm	1	0.15	0.3
Peak Power	W	77	218	77

4.1.1.1 Surface Topography

Figure 11 shows the SEM images of the laser machined Vitreloy1b using the laser settings in Table 1. Field 1 clearly shows a sequence of well-formed overlapping circular craters each with a radius of approximately 15 µm. The distance between each pulse is called the pulse distance which is set by the ratio of scanning speed to

frequency. The distance between each track is the track distance, also called the hatch distance. For field 1 the distance between each track is set at 15 µm .

In comparison to filed 1 the lateral crater distance is smaller for field 2 due to the differences in beam scanning speed and repetition rate. There is far greater overlap between the pulses. Additionally the track distance for field 2 is shorter and therefore the single craters are not as visible and far more overlap between each crater is seen. Similarly to field 1, field 2 has maintained a highly ordered and regular structure with clear parallel tracks. The approximate width of the part of each crater that can be seen is 3 µm across and 6 µm in height.

The laser settings used for field 3 have produced a somewhat different surface morphology in comparison to fields 1 and 2. Although tracks are still apparent, individual craters are no longer recognisable and some melting has occurred creating a more random and ragged arrangement. This may be explained by the slower scanning speed which means the surface experiences greater heat absorption.

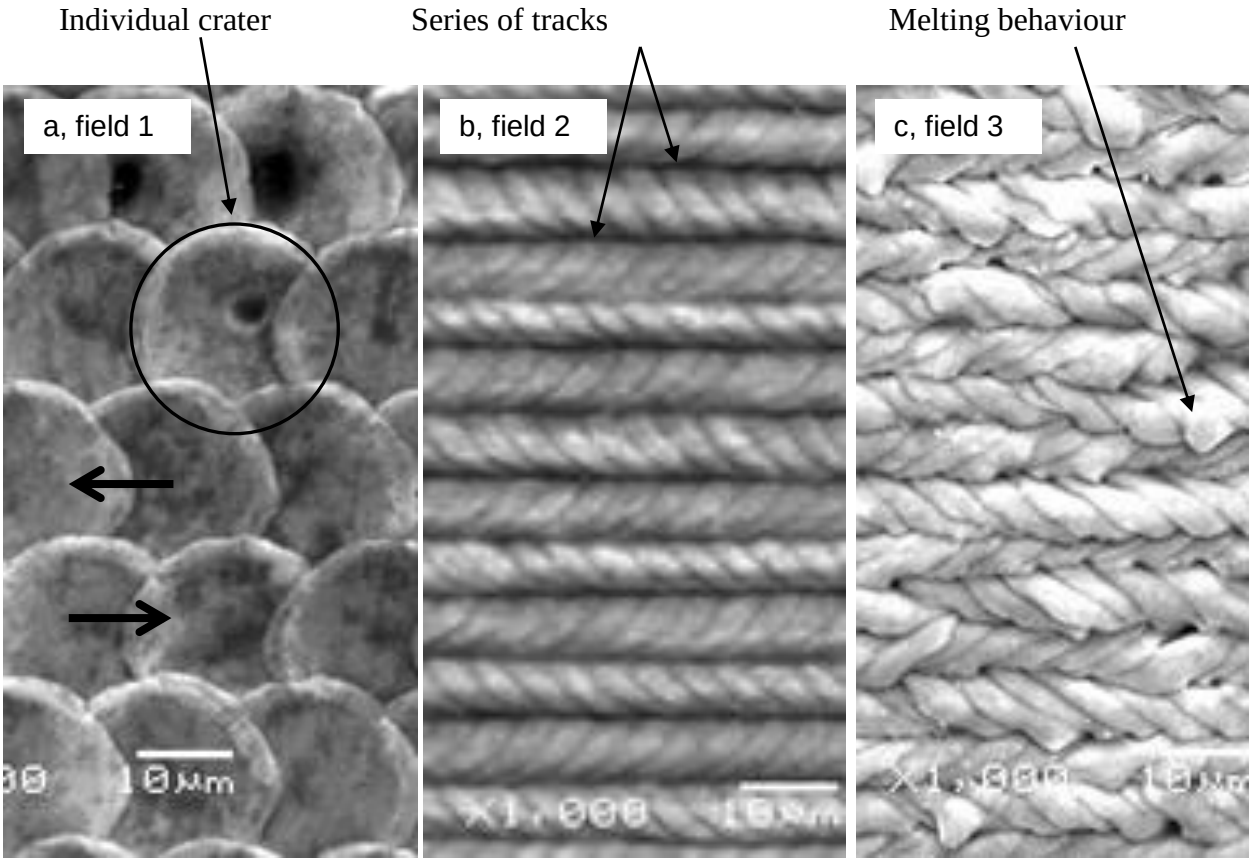

Figure. 11. SEM images of laser machined fields 1 (a) arrows identify the direction of the laser scan, 2(b) and 3(c)

4.1.1.2 X-ray Diffraction Studies

Figure 12 displays the XRD traces for the laser machined samples. The XRD trace for the as-received Vitreloy1b amorphous alloy depicts broad peaks in the 2θ range of 30 to 50^{o}. The broad diffraction hump without any appreciable crystalline peaks in the XRD pattern indicates that the as-cast sample is basically amorphous. The XRD trace for field 1 shows a predominantly amorphous structure but a sharp peak is observed at 2θ 27^{o} suggesting the onset of crystallisation has started. Within the literature following annealing the first crystalline peaks are those of a quasicrystalline phase [82, 83]. These peaks suggest that although the material is predominately amorphous some crystallisation has been triggered.

Field 2 shows several more sharp peaks which suggest more crystallisation has begun. The second crystallisation phase associated with Vitreloy1b is the crystallisation of the stable phases in particular Be_2Zr, Zr_2Ni, Zr_2Cu and NiTi [83]. But the crystallisation has not yet completed so the residual amorphous structure remains as indicated by the presence of broad peaks.

The trace for field 3 depicts the loss of the broad peaks, instead the trace shows a series of sharp peaks which suggest complete crystallisation has occurred and the material is no longer amorphous.

a, as-received

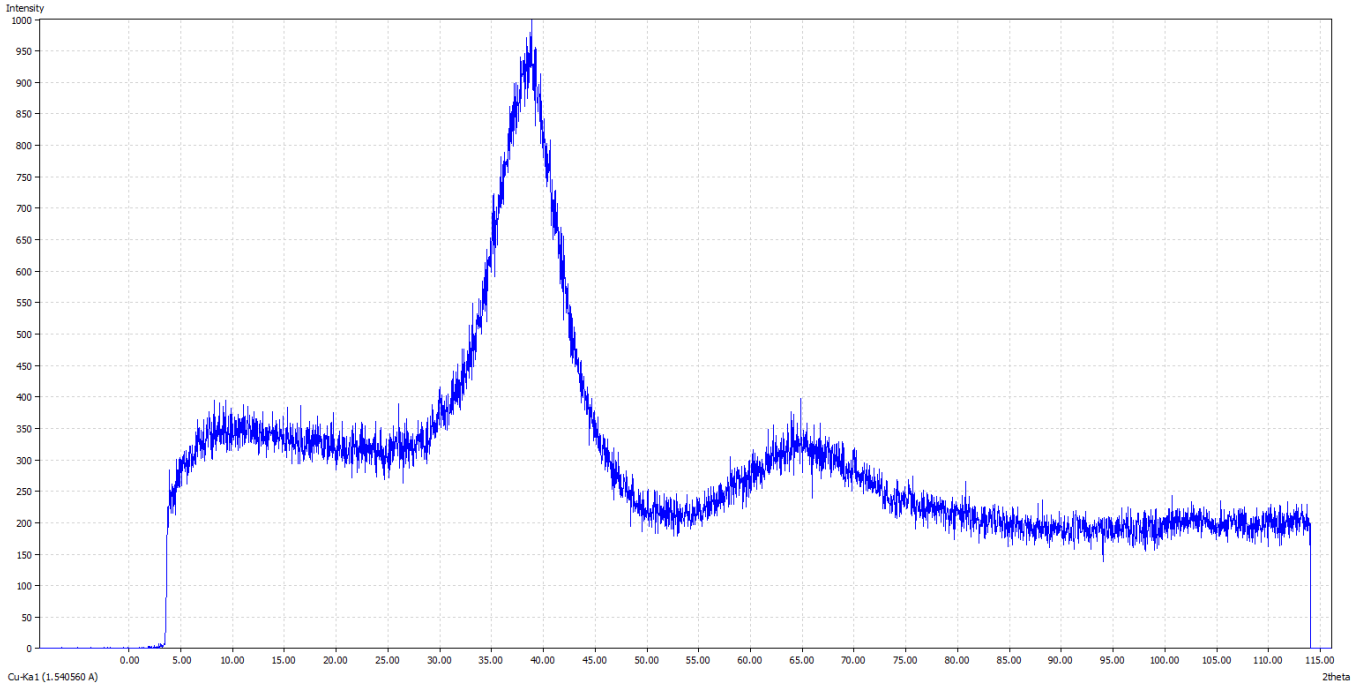

b, field 1

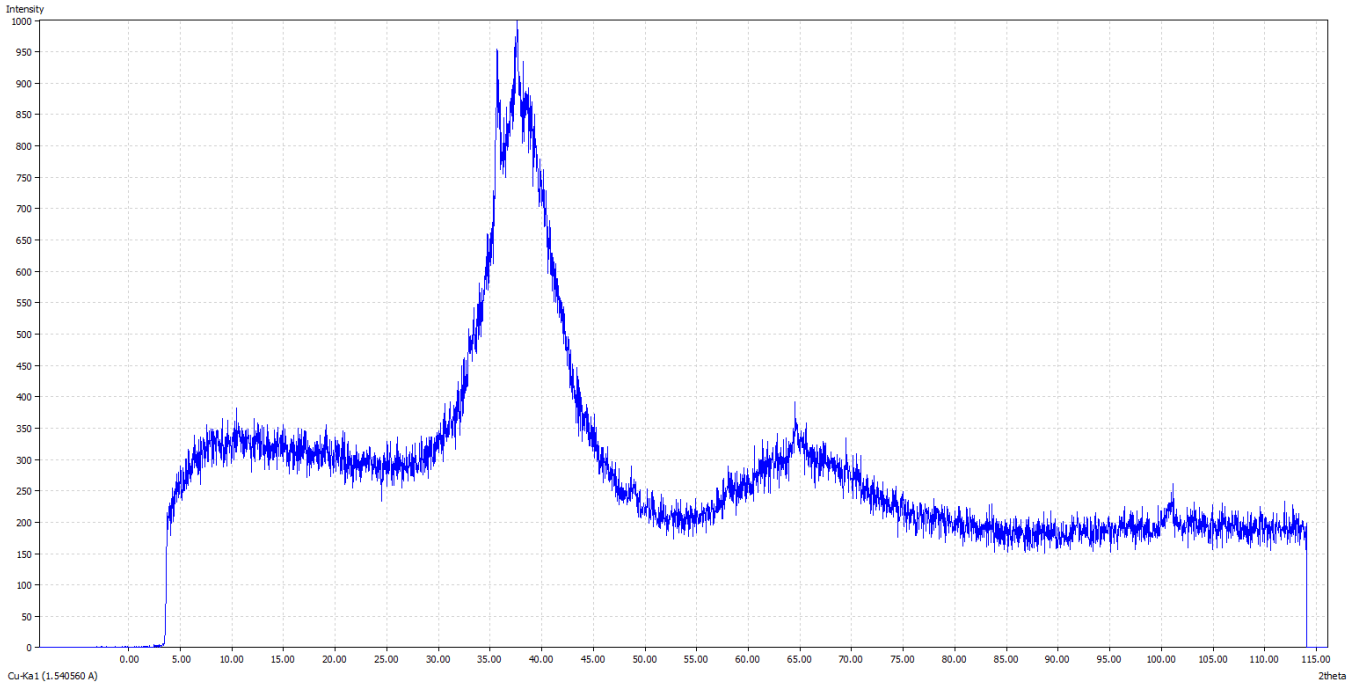

c, field 2

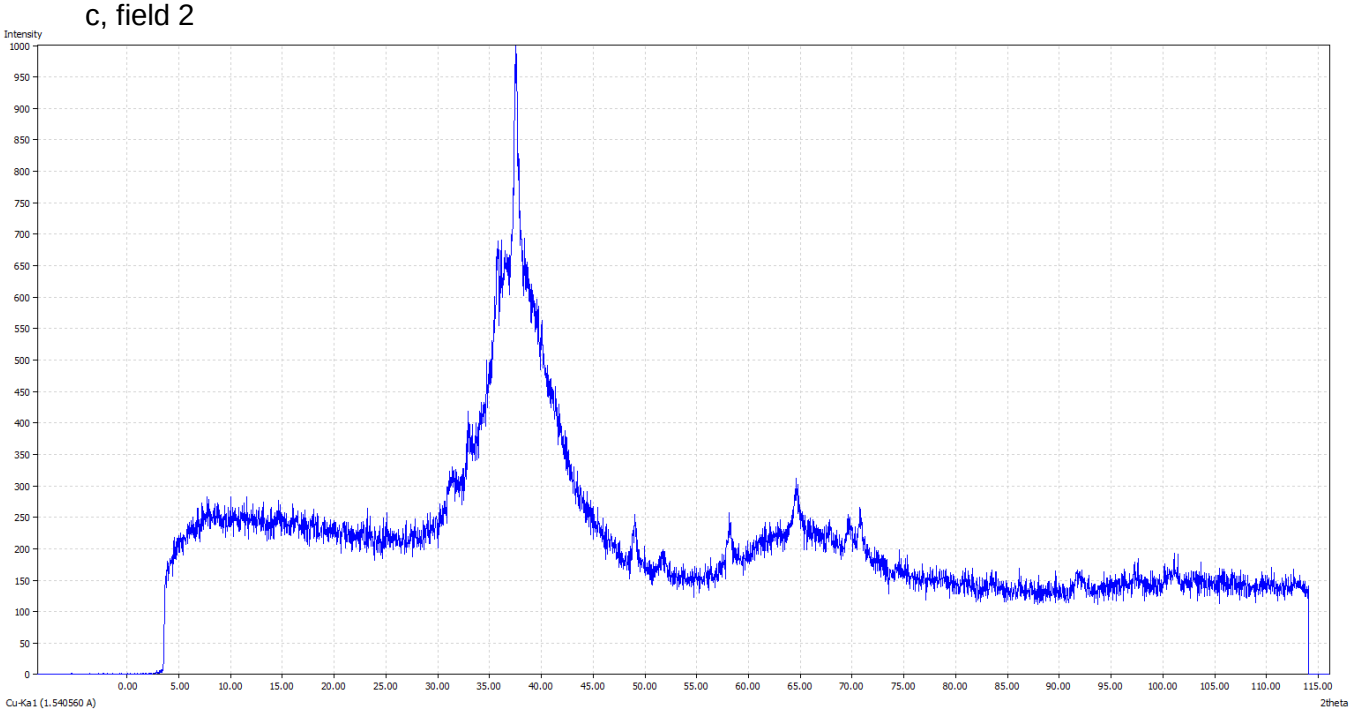

d, field 3

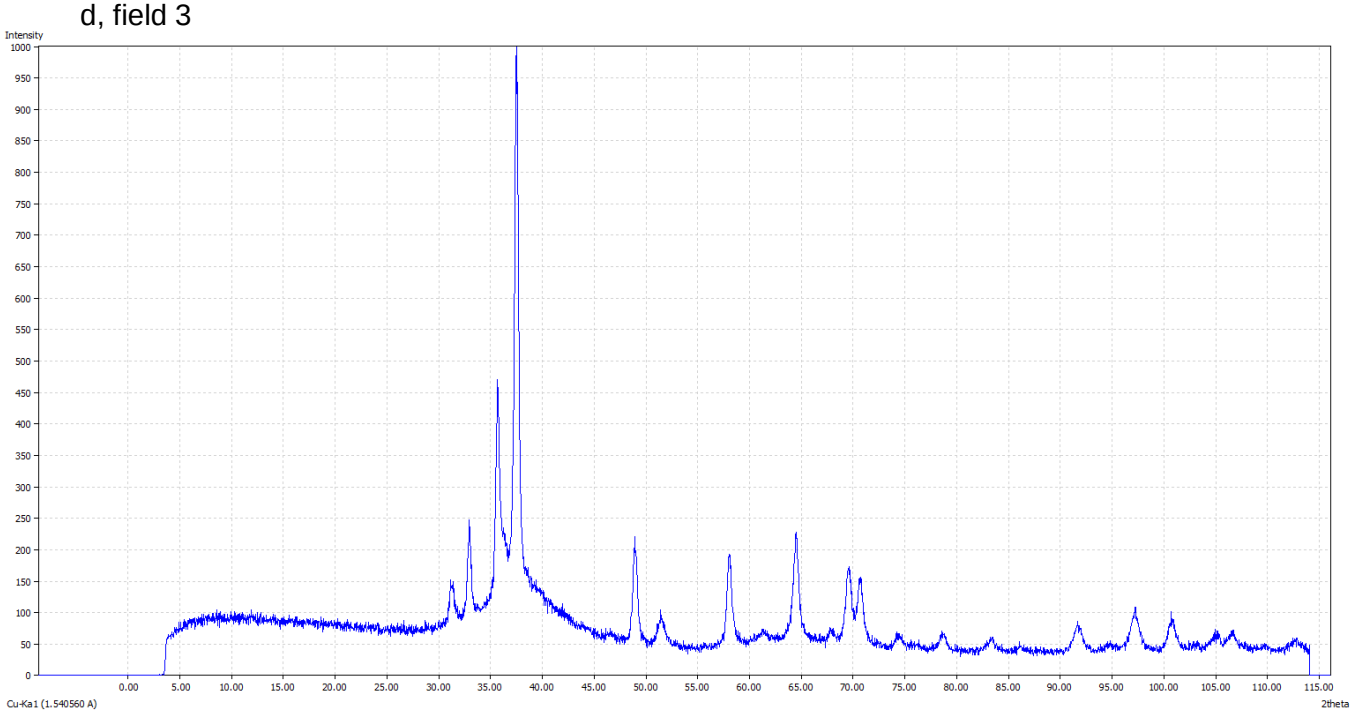

Figure 12. XRD pattern for laser machined fields: (a) as-received material, (b) field 1, (c) field 2, (d) field 3

4.1.1.3 Surface Roughness

The Taylor-Hobson measurements presented in table 2 show that field 2 produced the lowest surface roughness with a Ra of 0.16 µm. This may be attributed to the short distance observed between each crater. Field 3 produced the highest surface roughness of Ra of 0.26 µm.

Table 5. Taylor-Hobson surface roughness measurements for laser machined fields

Field	Surface roughness Ra (µm)
1	0.22
2	0.16
3	0.26

4.1.2 Second set of laser machining trials

The results gathered from the first three laser machining trails were analysed in order to create eight new machining settings. Co-workers at Cardiff University attempted to create a theoretical model to calculate the thermal model of each sample. However, since the creation of such model requires time and efforts which were not feasible within this study, instead it was hypothesised that increasing the peak power in the second set of trials would reduce the amount of thermal diffusion and in turn avoid crystallisation. Few studies have performed ns laser machining onto BMGs and thus a variety of different processing parameters to analyse which could produce the lowest surface roughness whilst maintaining an amorphous structure.

The settings for the second set of trials are shown in table 6. Unfortunately due to the time necessary for performing XRD analysis of the laser machined fields only eight

settings were used and it was not possible to conduct a systematic search for optimal settings in the whole space of laser machining parameters.

Table 6. Laser machining parameters for second trials

Parameters	Units	Field							
		1	2	3	4	5	6	7	8
Power	W	1.77	2.13	0.16	3.01	2.62	5.3	0.25	1.96
Repetition rate	kHz	100	100	10	100	167	167	17	250
Pulse Energy	µJ	17.7	21.3	16	30.1	15.7	31.7	14.7	7.8
Scanning speed	m/s	1	1	0.1	1	1	1	0.1	1
Fluence	J/cm^2	1.84	2.21	1.66	3.13	1.63	3.30	1.53	0.85
Track distance	µm	10	10	10	10	6	6	6	4
Layer thickness	µm	0.3	0.5	0.3	0.3	0.3	0.8	0.3	0.3
Peak Power	W	222	445	334	1890	983	1990	922	491

4.1.2.1 Surface Topography

Figure 13 shows the SEM images for fields 1 to 8 produced using the laser settings listed in table 3. Field 1 depicts clear signs of ejection of semi-vaporized material from the laser material interaction area through melt expulsion resulting in a surface morphology which is highly non-uniform. When a higher laser peak power is used the material starts splashing and builds a ragged recast layer. In comparison to the results from the first set of trials in figure 11, no parallel tracks created by the individual craters

are visible. A similar surface morphology is observed for fields 2, 3, 4, 6 and 7 where each field shows a highly random splash like surface.

The surface morphology for field 5 is more comparable to that of field 3 in the first set of experiments where although the individual craters cannot be distinguished there is some uniformity and the parallel tracks are visible. Field 8 on the other hand shows the most uniform surface morphology. It shows are very similar appearance to field 2 from the first set of experiments with visible highly overlapping craters in a series of parallel tracks.

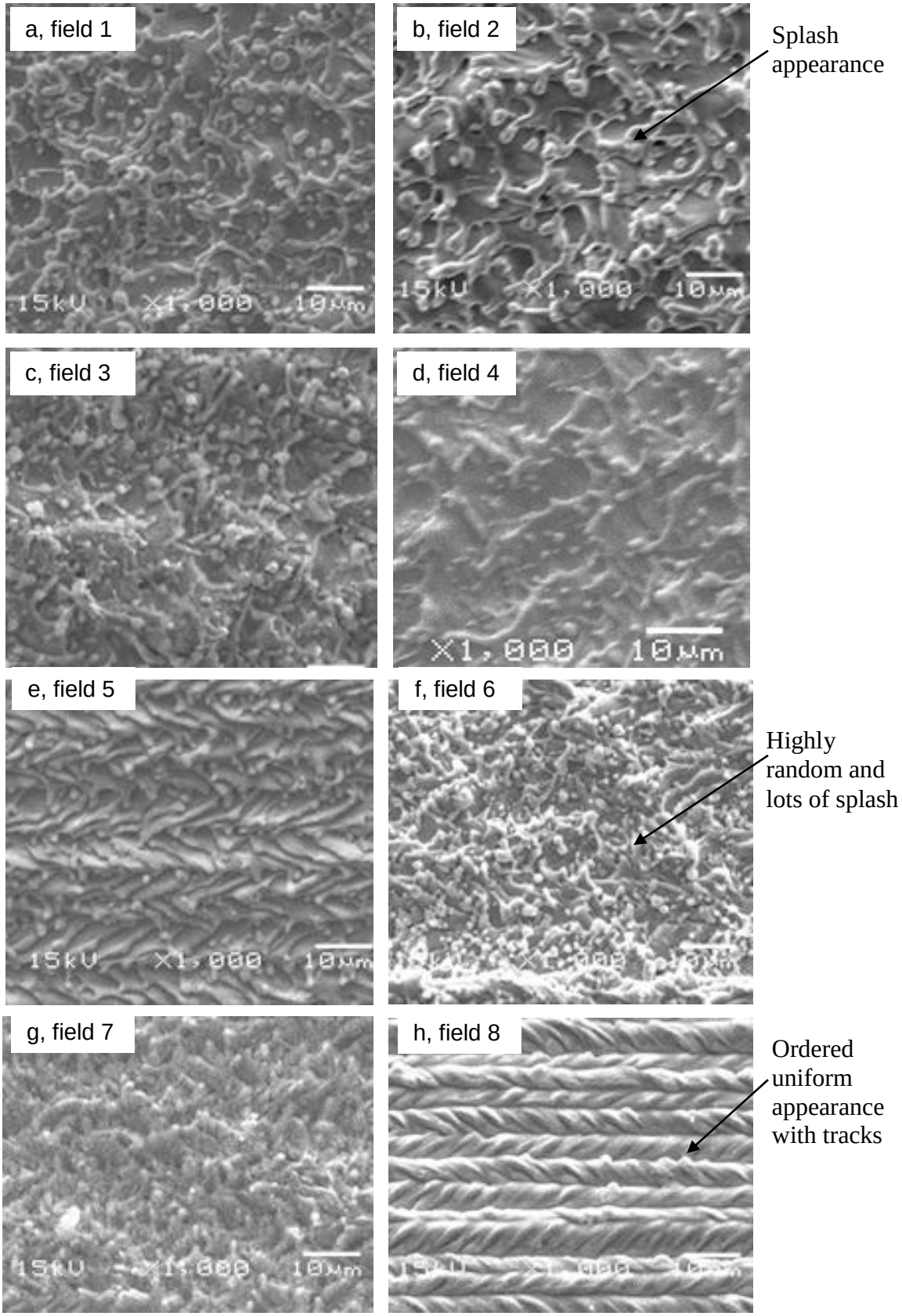

Figure 13. SEM images of laser machined fields 1 (a), 2 (b), 3 (c), 4 (d), 5 (e), 6 (f), 7 (g), and 8 (h)

4.1.2.2 X-ray Diffraction Studies

The XRD traces for the laser machined fields 1 to 8 are shown in figure 14**.** All fields exhibited a high background noise compared to the as-received material in figure 12a. The diffraction profiles show the presence of a clear amorphous phase in the 2θ range of 30-50^{o}. Each of the diffraction profiles matches that of the as-received material with only broad peaks and no sharp individual peaks. This suggests that all eight laser machining settings used in the second set of experiments did not affect the non-crystalline morphology of the Vitreloy1b amorphous alloy. These results suggest that the hypothesis was correct and by increasing the peak power whilst maintaining the same pulse width the thermal load can be reduced and in turn prevent crystallisation from occurring.

a, field 1

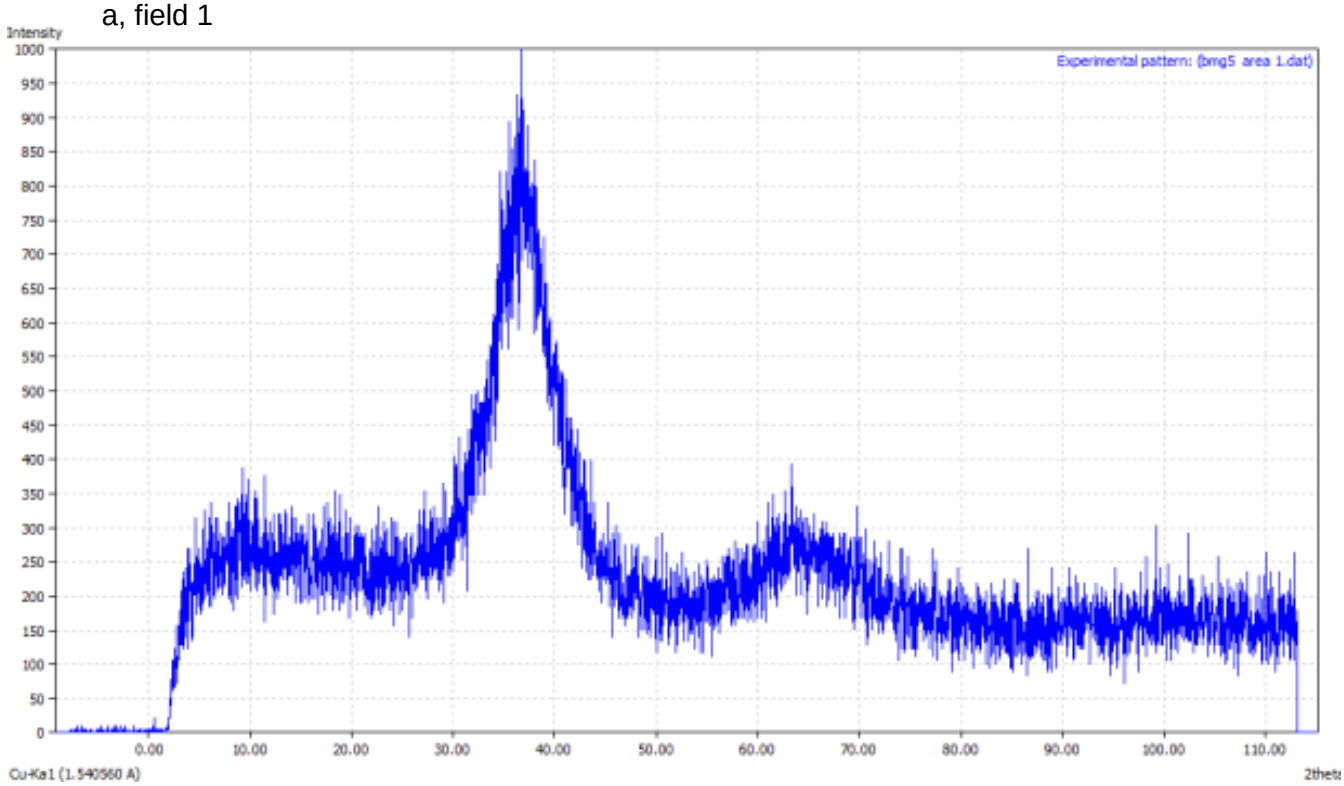

b, field 2

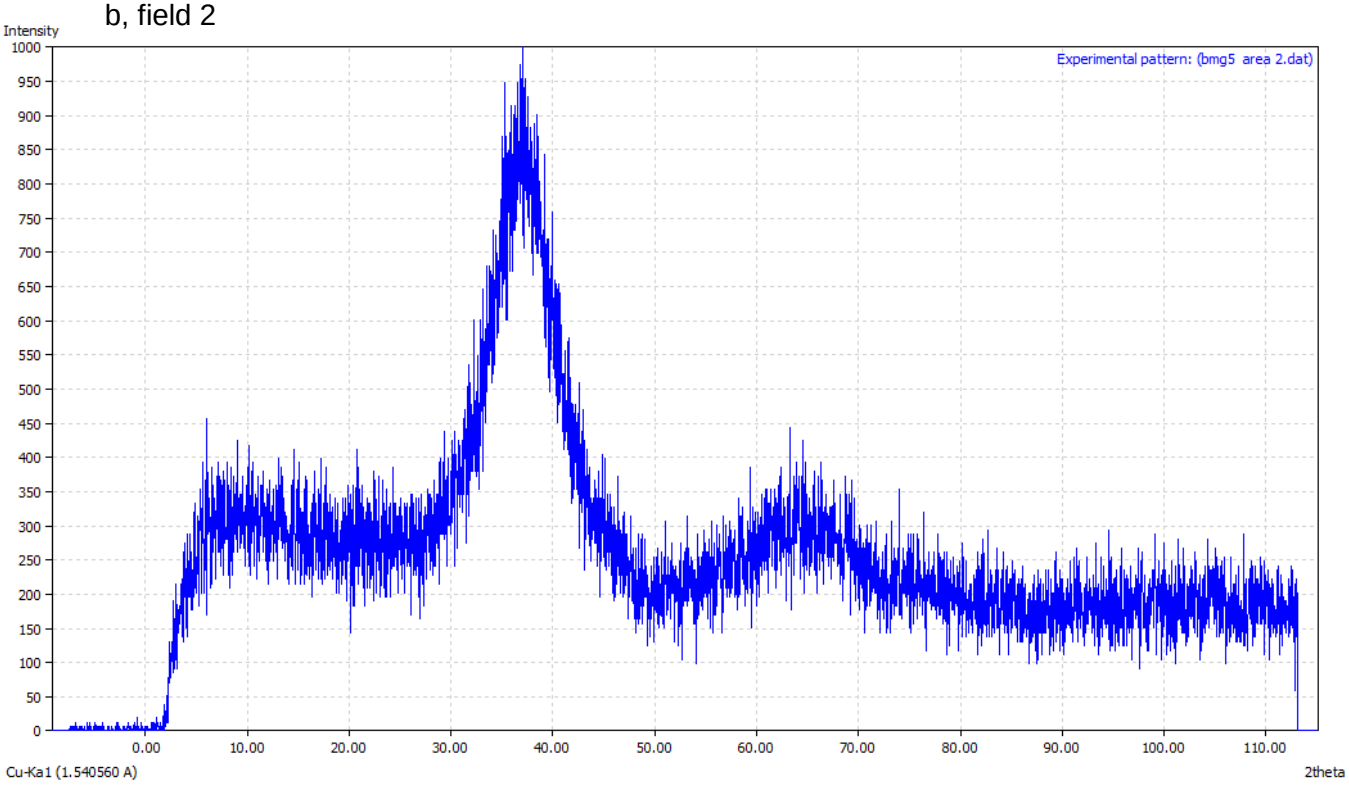

c, field 3

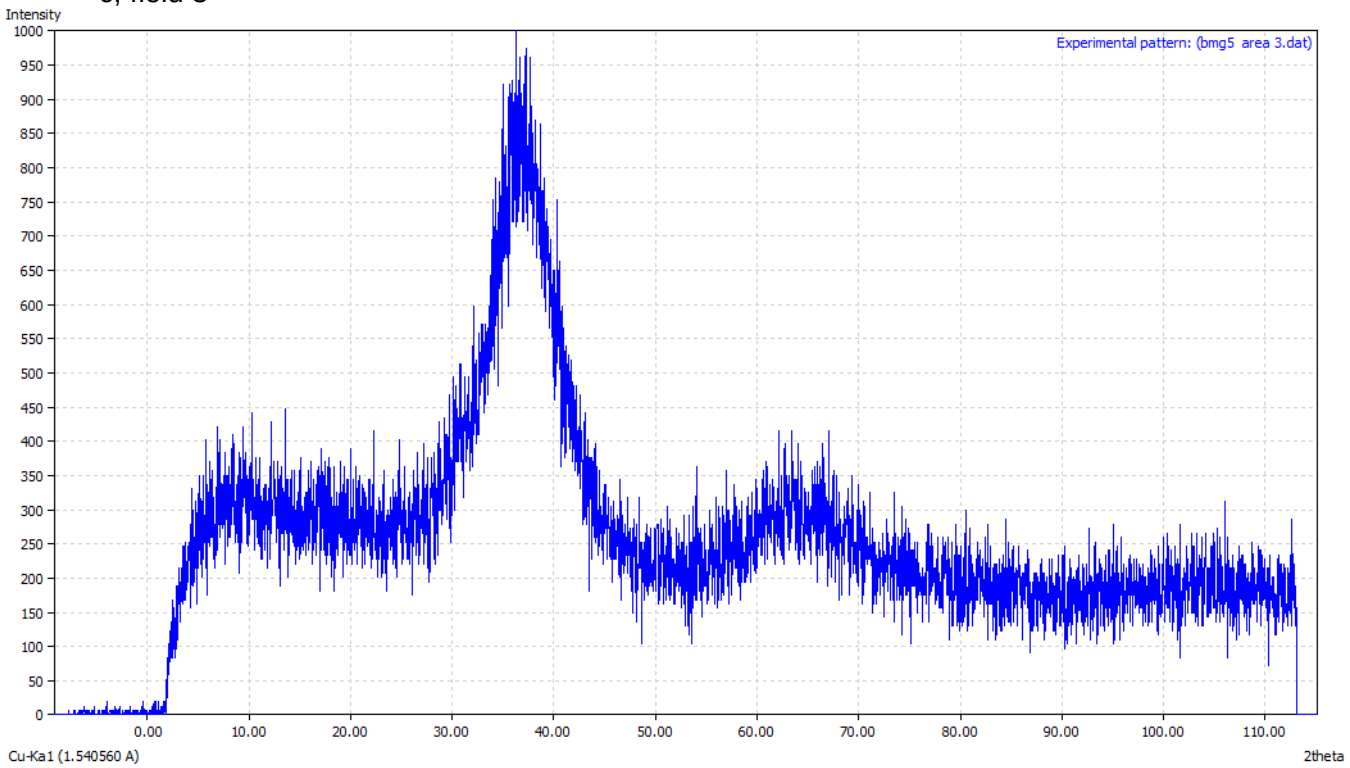

d, field 4

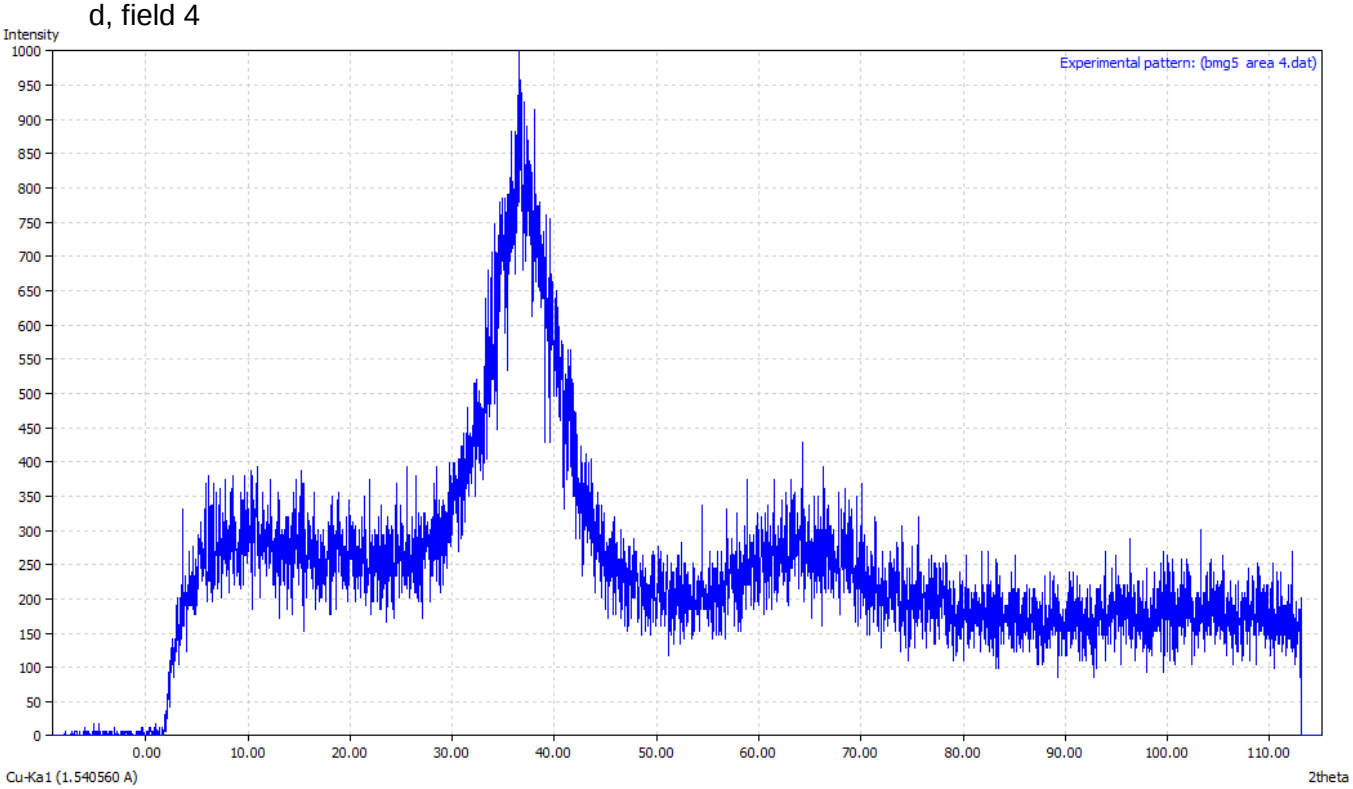

e, field 5

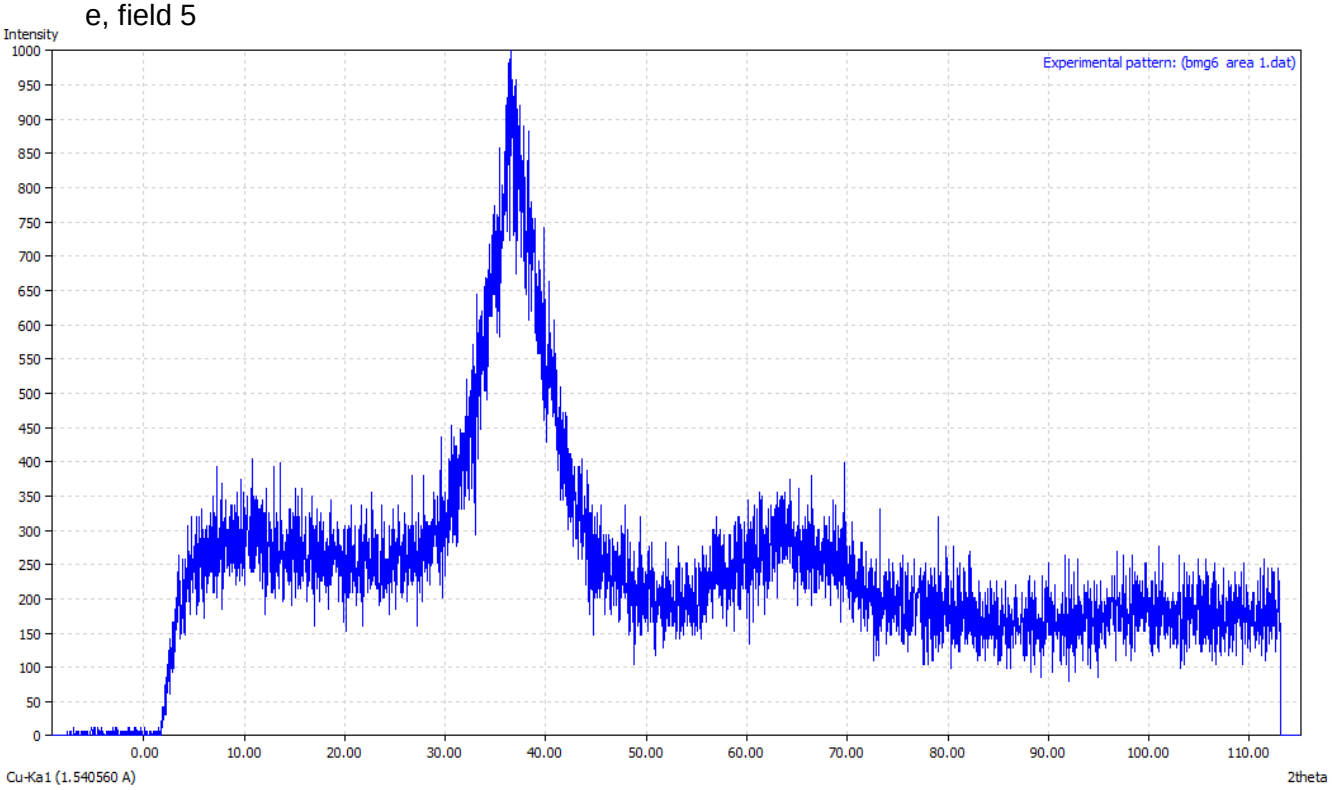

f, field 6

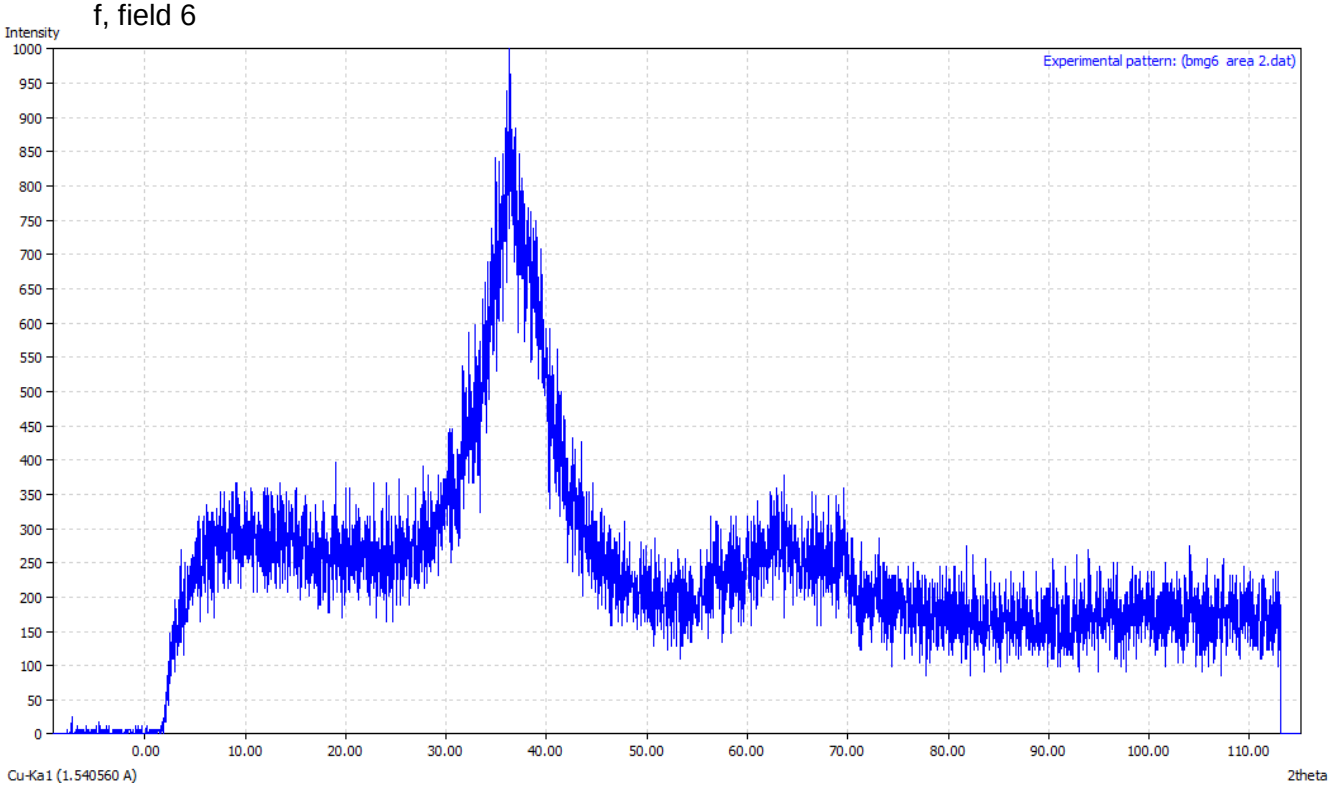

g, field 7

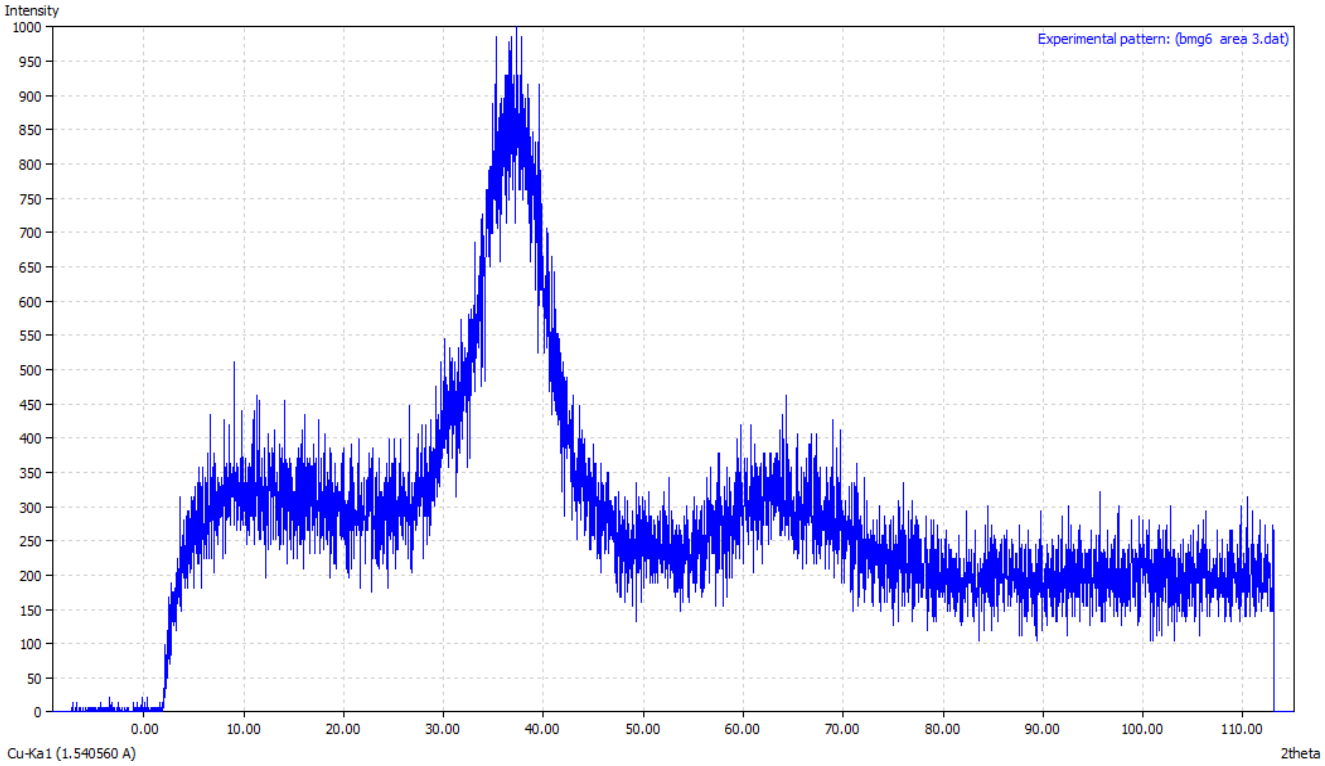

h, field 8

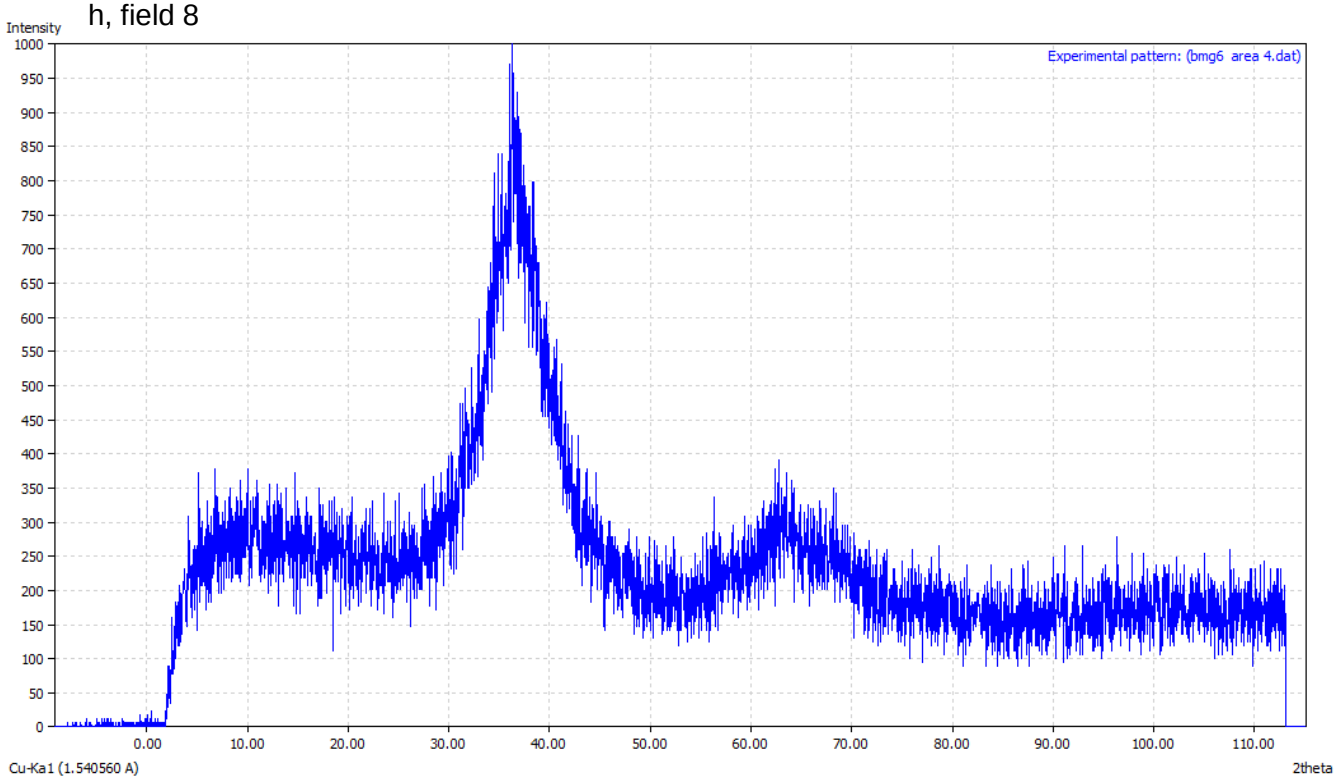

Figure 14. XRD pattern for laser machined fields 1 (a), 2 (b), 3 (c), 4 (d), 5 (e), 6 (f), 7 (g), and 8 (h)

4.1.2.3 Surface Roughness

Table 4 provides the surface roughness measurements for the eight laser machined fields. The lowest surface roughness was achieved by fields 5 and 8 with roughnesses of 0.37 and 0.26 μm respectively. Evidently these two fields were the two which showed the most uniform surface topography when characterised using SEM.

The two fields with the highest surface roughness were fields 3 and 6 with Ra roughness measurements of 0.9 and 0.82 μm. Predictably, SEM revealed these two fields to have the most random and ragged surface topography.

Table 7. Taylor-Hobson surface roughness measurements for sample eight laser machined fields

Field	Surface roughness Ra (μm)
1	0.58
2	0.75
3	0.90
4	0.58
5	0.37
6	0.82
7	0.59
8	0.26

4.2 Hot plate (conventional) annealing

4.2.1 First set of hot plate annealing experiments

The annealing conditions used to conduct the first set of experiments are shown in table 8. The temperature selected for this set of experiments was 380^{o}C, towards the lower end of the SCLR for Vitreloy1b. The time before crystallisation at lower temperatures is

longer in comparison to a higher temperature. A total time of 960 seconds was also selected in order to preserve the amorphous phase.

Table 8. Annealing conditions for first set of experiments

Run	Temperature (^{o}C)	Total Annealing Time (seconds)
1	380	20
2	380	60
3	380	140
4	380	240
5	380	360
6	380	960

4.2.1.1 Surface Topography

Figure 15 shows the SEM images following each annealing run. Figure 15a corresponds to field 1 produced in the first set of laser machining experiments. Thus its surface topography is as described in the previous section. Comparing figure 15b after 20 seconds of annealing at 380 to the pre-annealed microstructure in figure 15a it is clear that no microstructural changes have occurred. The series of parallel tracks formed by the sequence of single craters during laser machining remains evidently present. A similar story continues for the following annealing runs. After a total annealing time of 960 seconds the craters remain visible and unchanged.

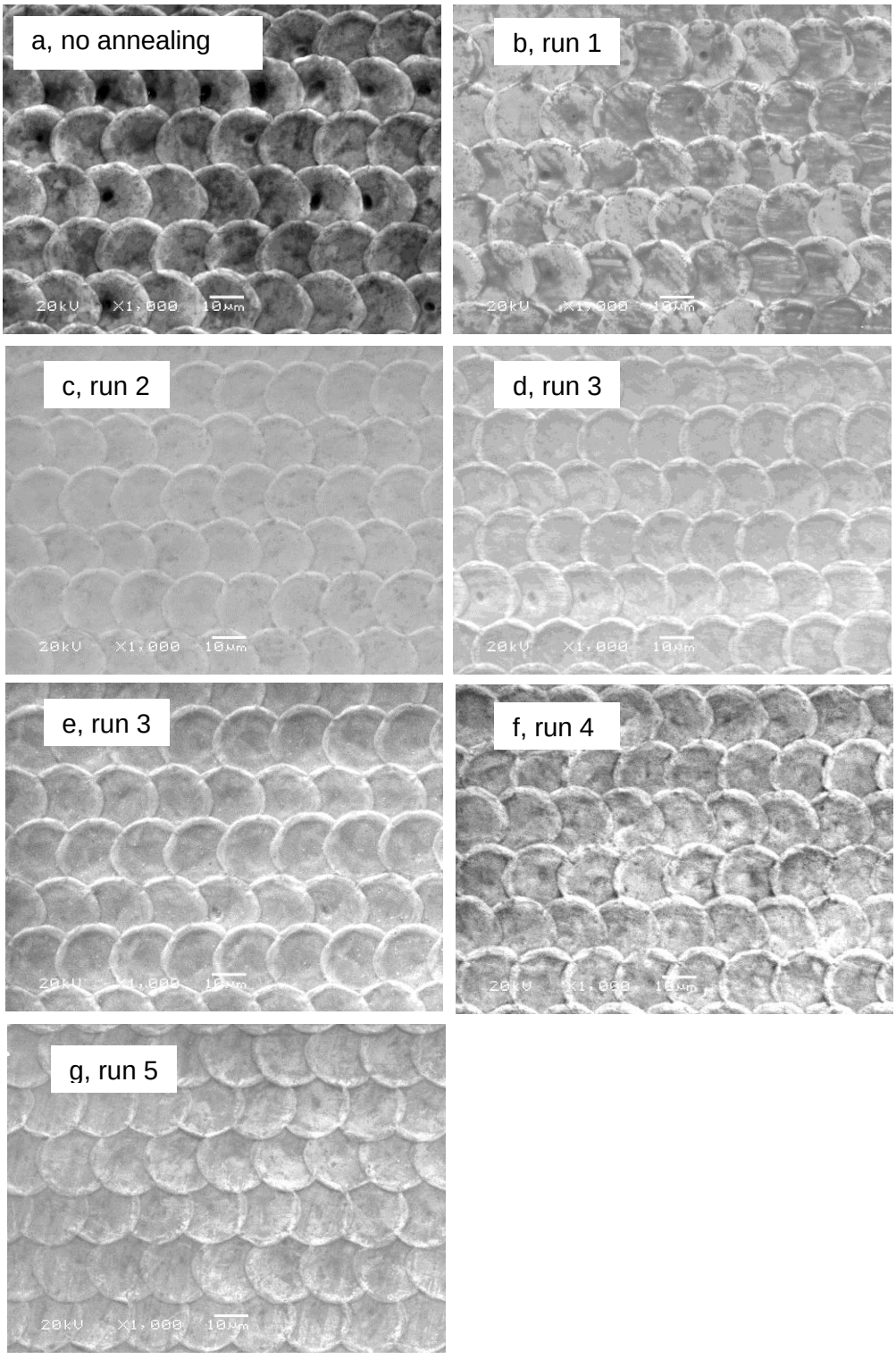

Figure 15. SEM images of field 1 after each annealing run: (a) no annealing, (b) run 1, (c) run 2, (d) run 3, (e) run 4, (f) run 5 and (g) run 6

4.2.1.2 X-ray Diffraction Studies

Figure 16 displays the XRD traces following each annealing run. Figure 16a displays the trace for field 1 before annealing. As described previously some minor crystallisation has occurred, particularly in the range of 27 ^{o}. The subsequent XRD traces for runs 1 to 5 all depict broad peaks and apart from some signs of noise show no change from the pre-annealed sample suggesting that no further crystallisation is occurring. The XRD trace of run 6 on the other hand shows a very sharp peak in the range 37 ^{o} and suggests signs of crystallisation, as shown in figure 16g.

a, no annealing

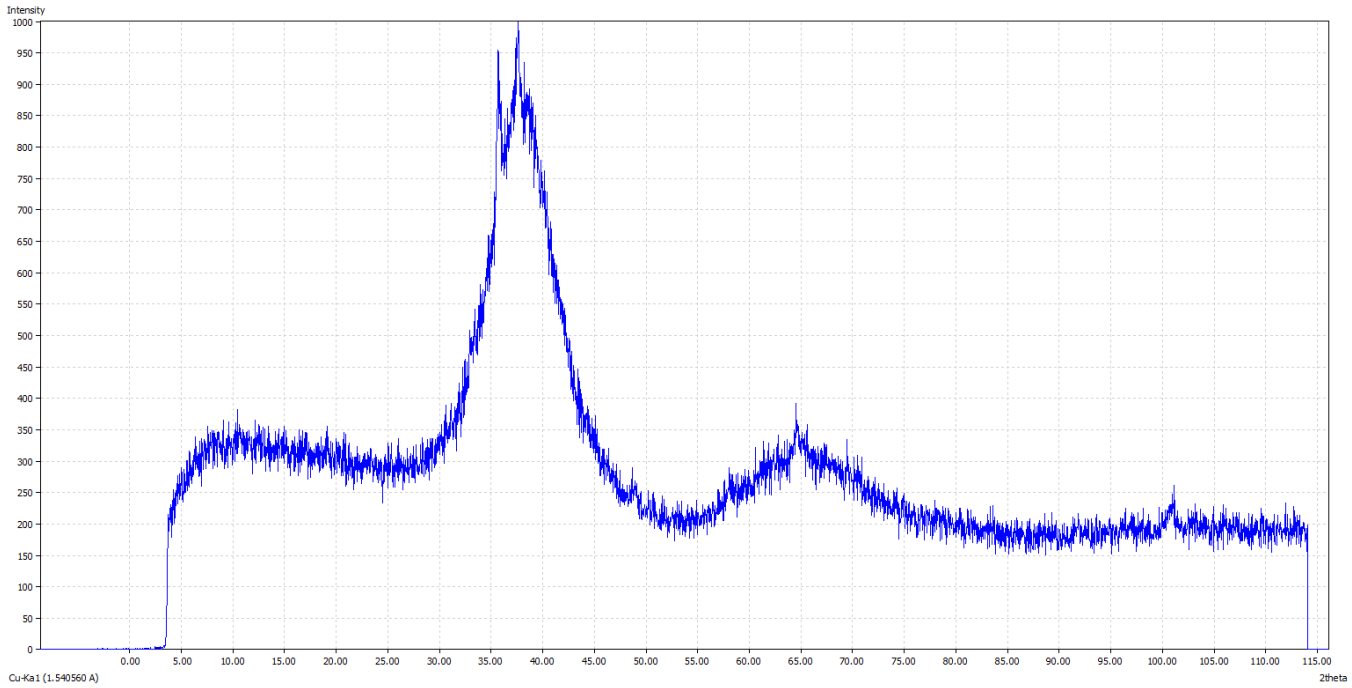

b, run 1

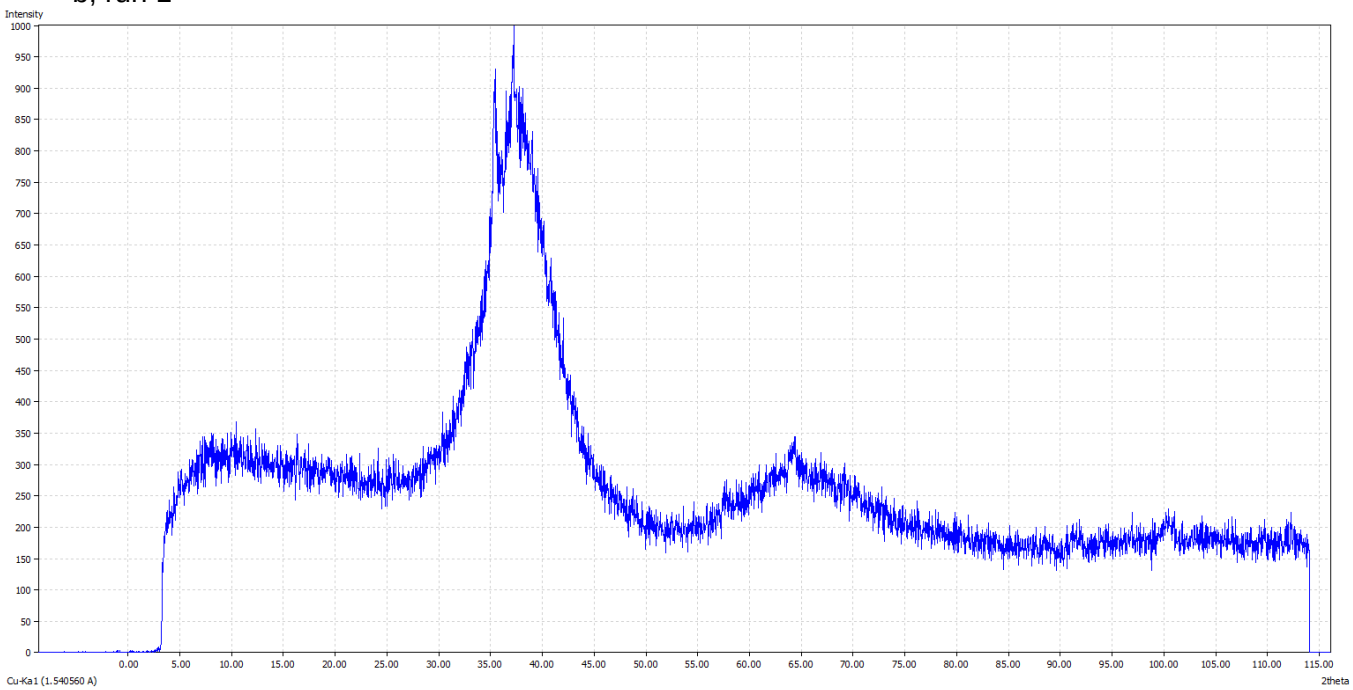

c, run 2

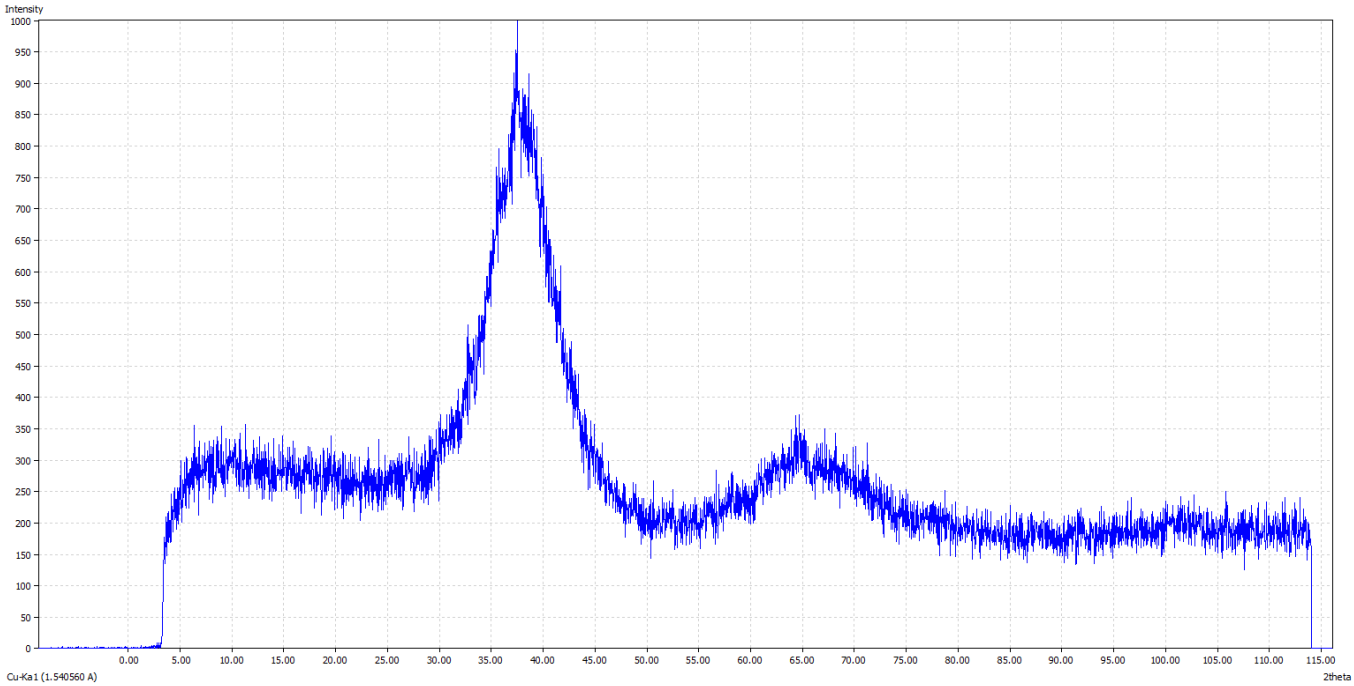
Intensity
1000
950
900
850
800
750
700
650
600
550
500
450
400
350
300
250
200
150
100
50
0
0.00 5.00 10.00 15.00 20.00 25.00 30.00 35.00 40.00 45.00 50.00 55.00 60.00 65.00 70.00 75.00 80.00 85.00 90.00 95.00 100.00 105.00 110.00 115.00
Cu-Ka1 (1.540560 A)
2theta

d, run 3

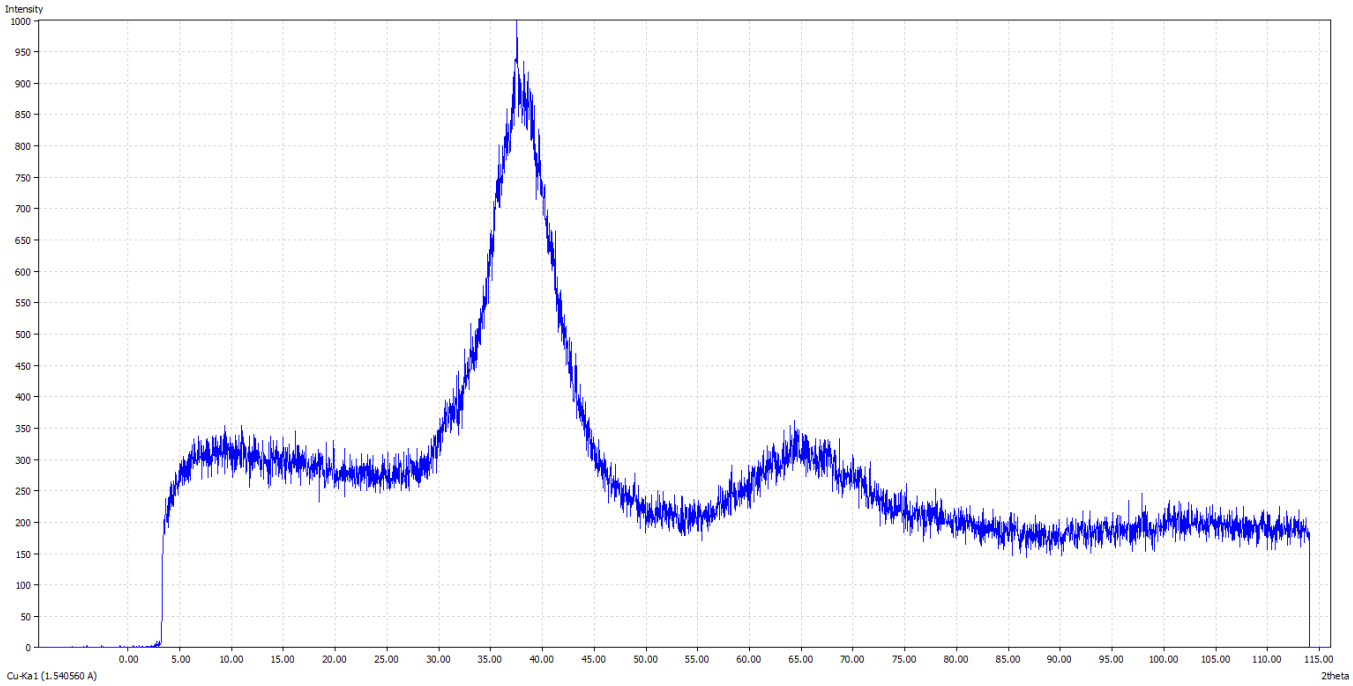
Intensity
1000
950
900
850
800
750
700
650
600
550
500
450
400
350
300
250
200
150
100
50
0
0.00 5.00 10.00 15.00 20.00 25.00 30.00 35.00 40.00 45.00 50.00 55.00 60.00 65.00 70.00 75.00 80.00 85.00 90.00 95.00 100.00 105.00 110.00 115.00
Cu-Ka1 (1.540560 A)
2theta

e, run 4

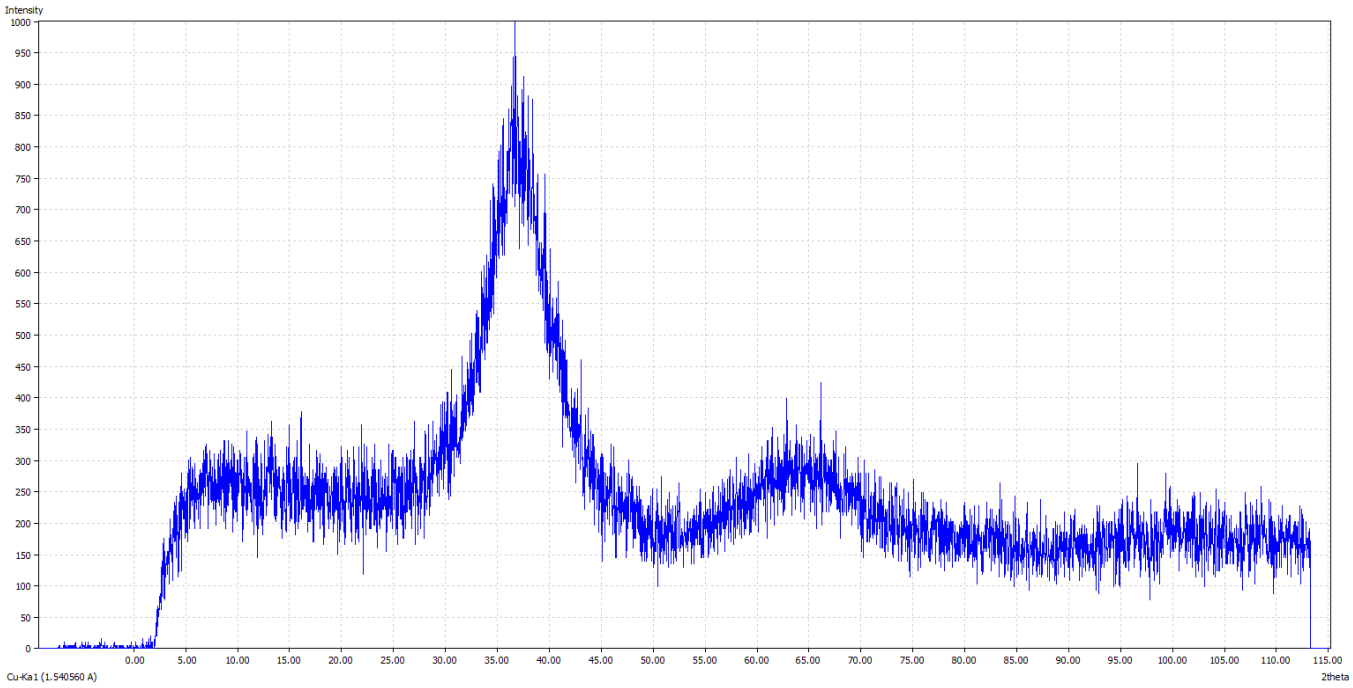
Intensity
1000
950
900
850
800
750
700
650
600
550
500
450
400
350
300
250
200
150
100
50
0
0.00
5.00
10.00
15.00
20.00
25.00
30.00
35.00
40.00
45.00
50.00
55.00
60.00
65.00
70.00
75.00
80.00
85.00
90.00
95.00
100.00
105.00
110.00
115.00
Cu-Ka1 (1.540560 A)
2theta

f, run 5

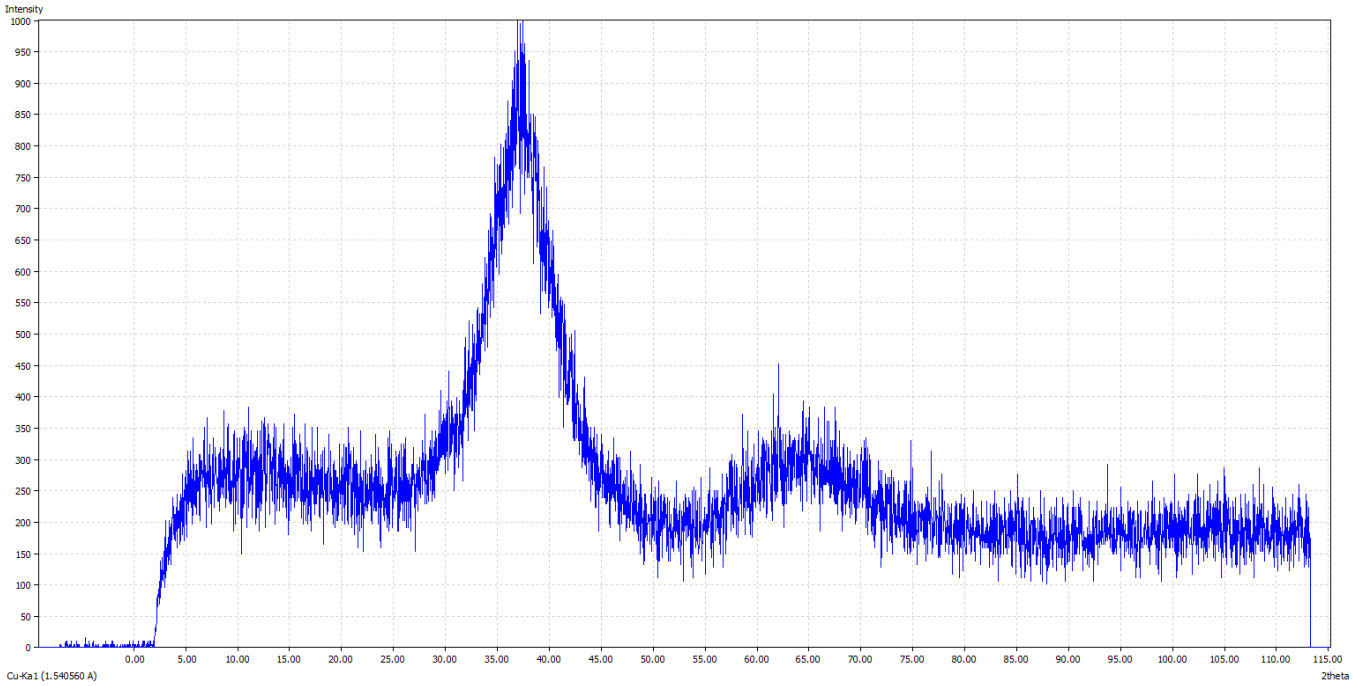
Intensity
1000
950
900
850
800
750
700
650
600
550
500
450
400
350
300
250
200
150
100
50
0
0.00
5.00
10.00
15.00
20.00
25.00
30.00
35.00
40.00
45.00
50.00
55.00
60.00
65.00
70.00
75.00
80.00
85.00
90.00
95.00
100.00
105.00
110.00
115.00
Cu-Ka1 (1.540560 A)
2theta

g, run 6

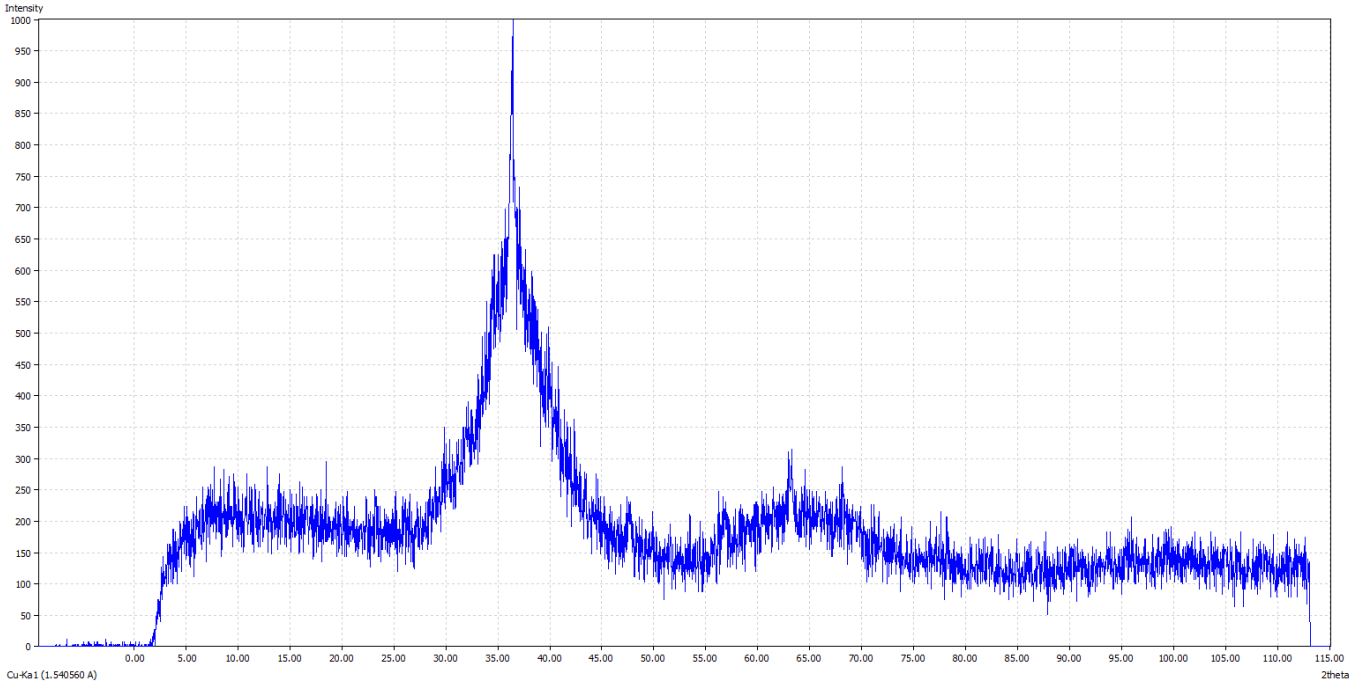

Figure 16. XRD pattern for field 1 after each annealing run: (a) no annealing, (b) run 1, (c) run 2, (d) run 3, (e) run 4, (f) run 5, (g) run 6

4.2.1.3 Surface Roughness

The surface roughness measurements following each annealing run is shown in Table 6. The surface roughness changes very little between no annealing and run 5. However, following run 6 the roughness increases by 0.04 μm. This result is fairly insignificant, however further chemical analysis would be beneficial to identify if any crystalline phases have been formed. Unfortunately, due to time constraints this was not achievable.

Table 9. Taylor-Hobson surface roughness measurements for field 1 after each annealing run

Run	Total Annealing Time (seconds)	Surface Roughness (μm)
No annealing	0	0.22
1	20	0.22
2	60	0.22
3	140	0.21
4	240	0.22
5	360	0.22
6	960	0.26

4.2.2 Second set of hot plate annealing experiments

The annealing conditions used in the second set of experiments are shown in Table 7. A temperature of 400^{o}C was used and a total time of 1000 seconds was selected in order to preserve the amorphous phase.

Table 10. Annealing conditions for second set of experiments

Run	Temperature (^{o}C)	Total Annealing Time (seconds)
1	400	40
2	400	100
3	400	340
4	400	640
5	400	1000

4.2.2.1 Surface Topography

The SEM images for the second set of experiments are shown in Figure 17. Figure 17a shows the surface topography for field 2 in the first set of laser experiments with highly overlapped craters and a sequence of clearly visible parallel tracks. Observing the subsequent SEM images following annealing figures 17b-f the images show no changes to the surface topography.

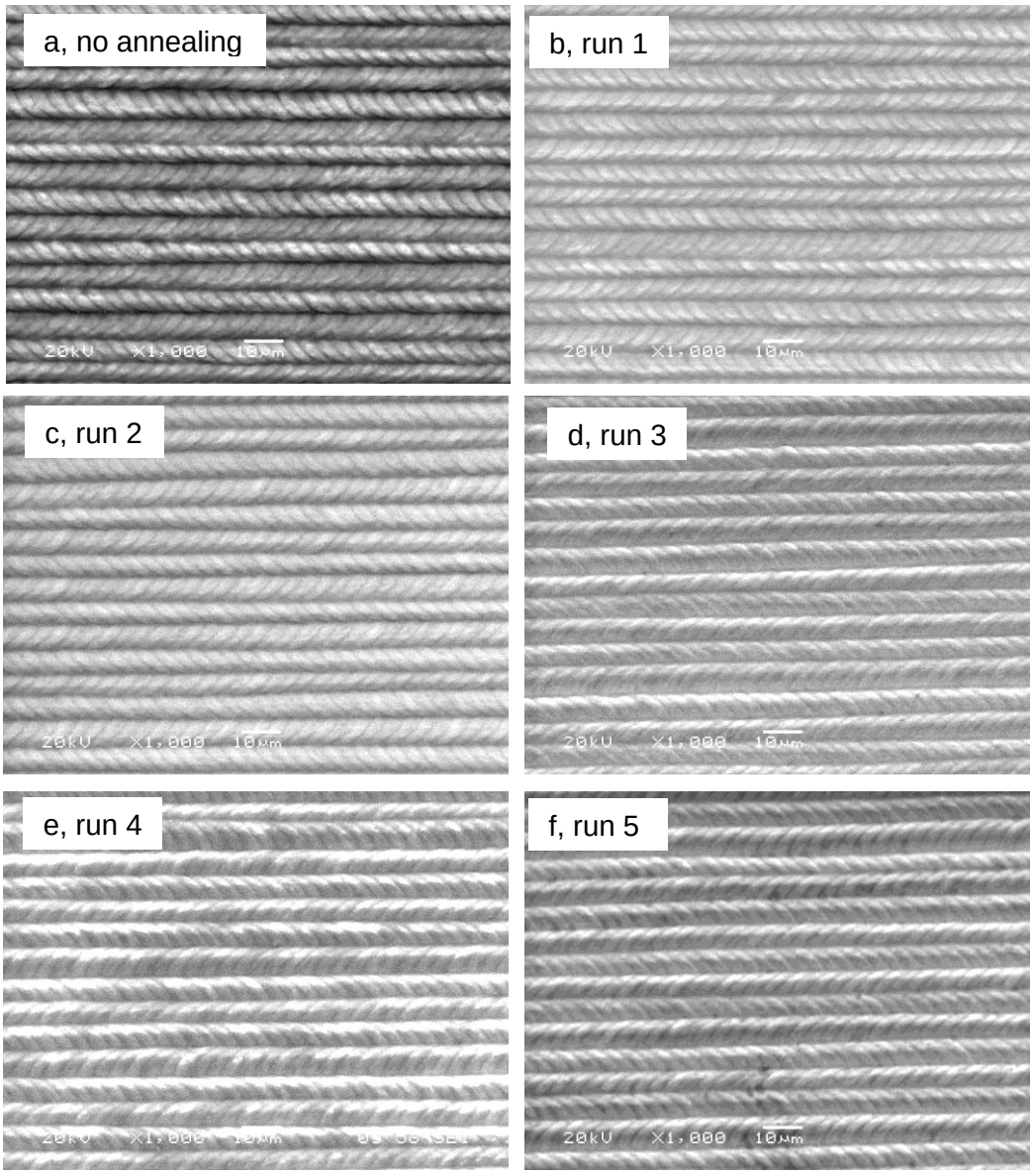

Figure 17. SEM images of field 2 after each annealing run: (a) no annealing, (b) run 1, (c) run 2, (d) run 3, (e) run 4 and (f) run 5

4.2.2.2 X-ray Diffraction Studies

Figure 18 displays the XRD traces for the second set of experiments. Figure 18a corresponds to the crystalline morphology produced by the laser machining in the first set of experiments. Each of the following figures 18b-f shows little or no change to the crystalline morphology. Apart from some noise the peaks remain predominantly broad suggesting further crystalline has not been caused by the annealing.

a, no annealing

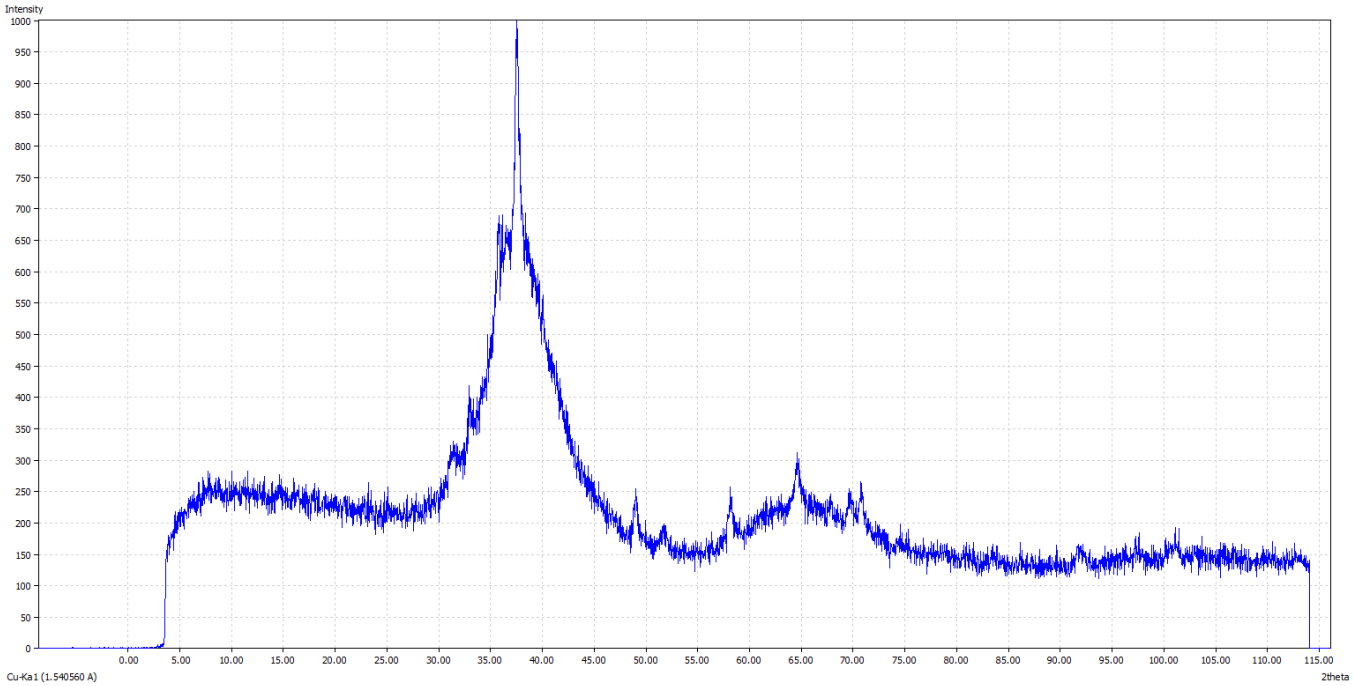

b, run 1

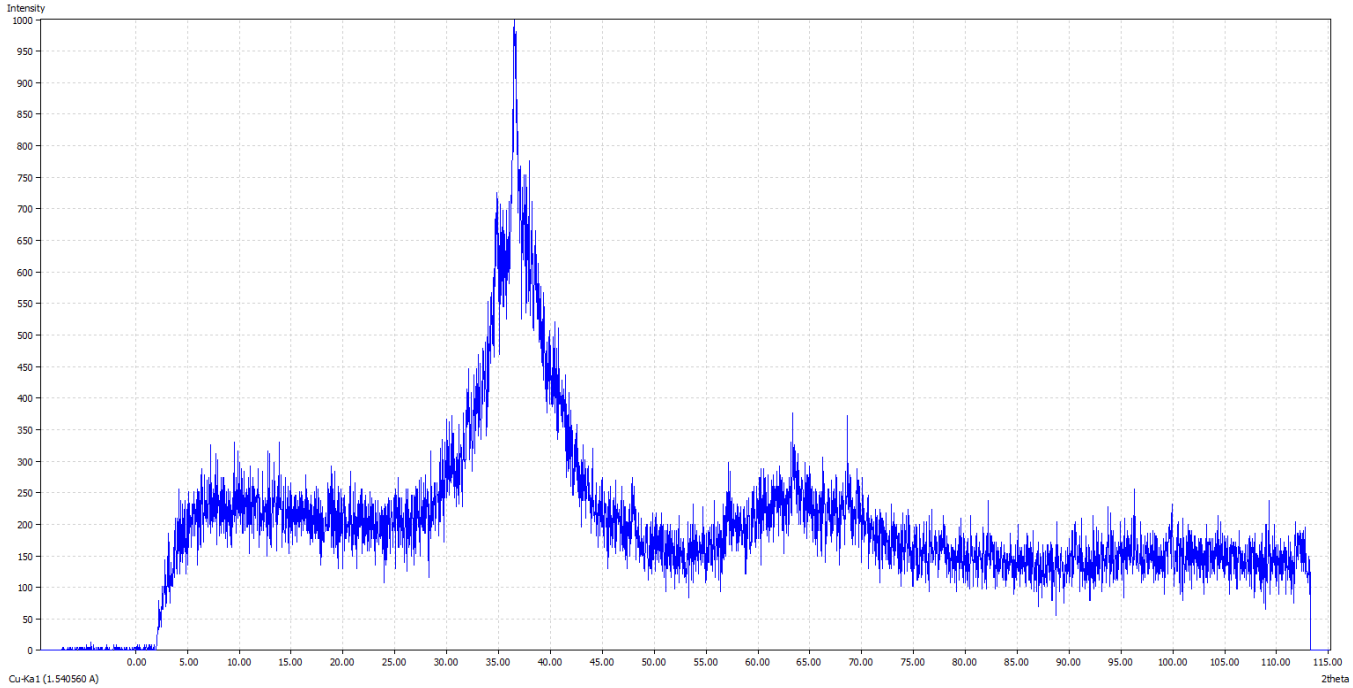

c. run 2

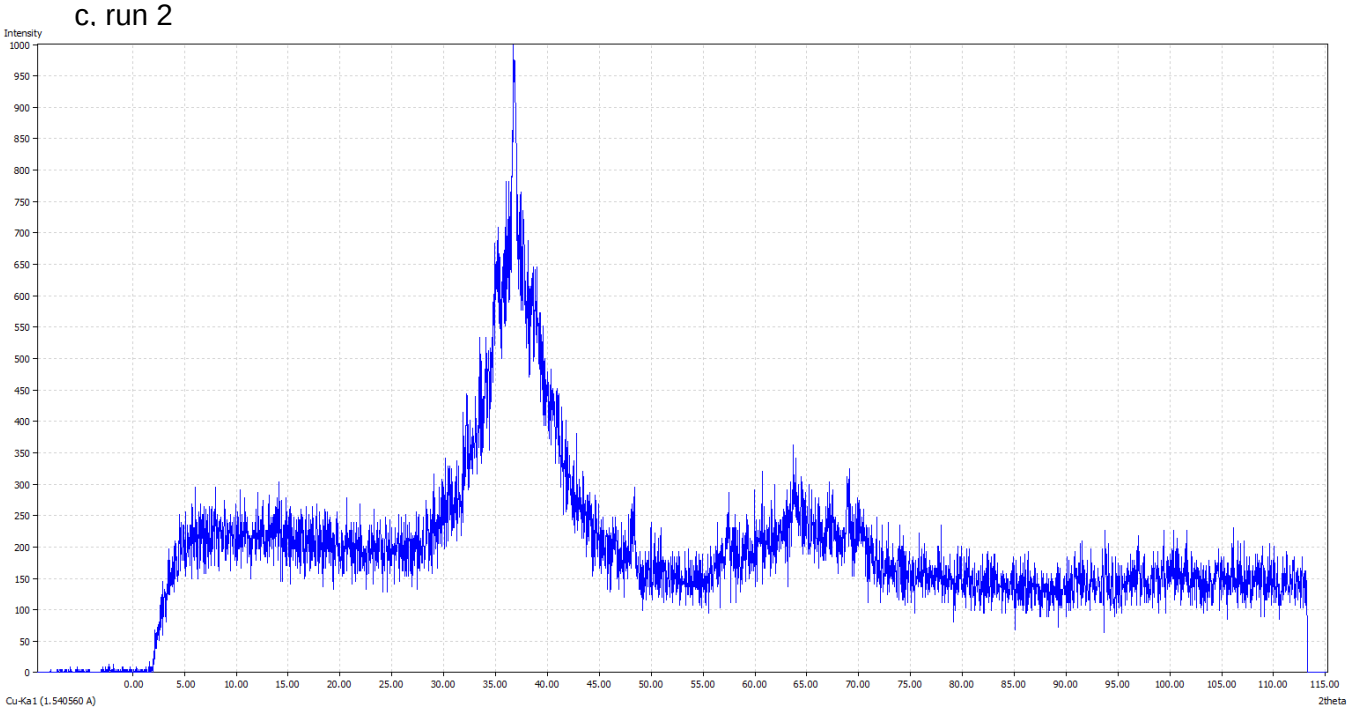
Intensity
1000
950
900
850
800
750
700
650
600
550
500
450
400
350
300
250
200
150
100
50
0
0.00
5.00
10.00
15.00
20.00
25.00
30.00
35.00
40.00
45.00
50.00
55.00
60.00
65.00
70.00
75.00
80.00
85.00
90.00
95.00
100.00
105.00
110.00
115.00
Cu-Ka1 (1.540560 A)
2theta

d, run 3

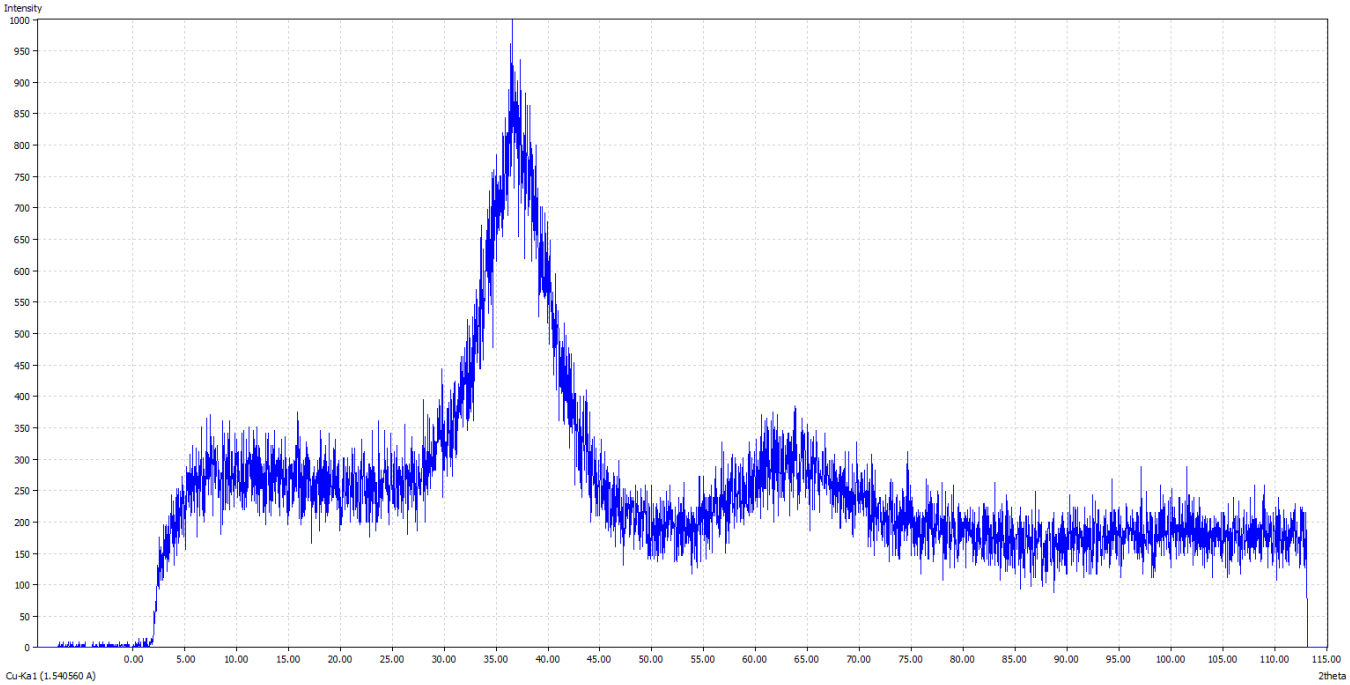
Intensity
1000
950
900
850
800
750
700
650
600
550
500
450
400
350
300
250
200
150
100
50
0
0.00
5.00
10.00
15.00
20.00
25.00
30.00
35.00
40.00
45.00
50.00
55.00
60.00
65.00
70.00
75.00
80.00
85.00
90.00
95.00
100.00
105.00
110.00
115.00
Cu-Ka1 (1.540560 A)
2theta

e, run 4

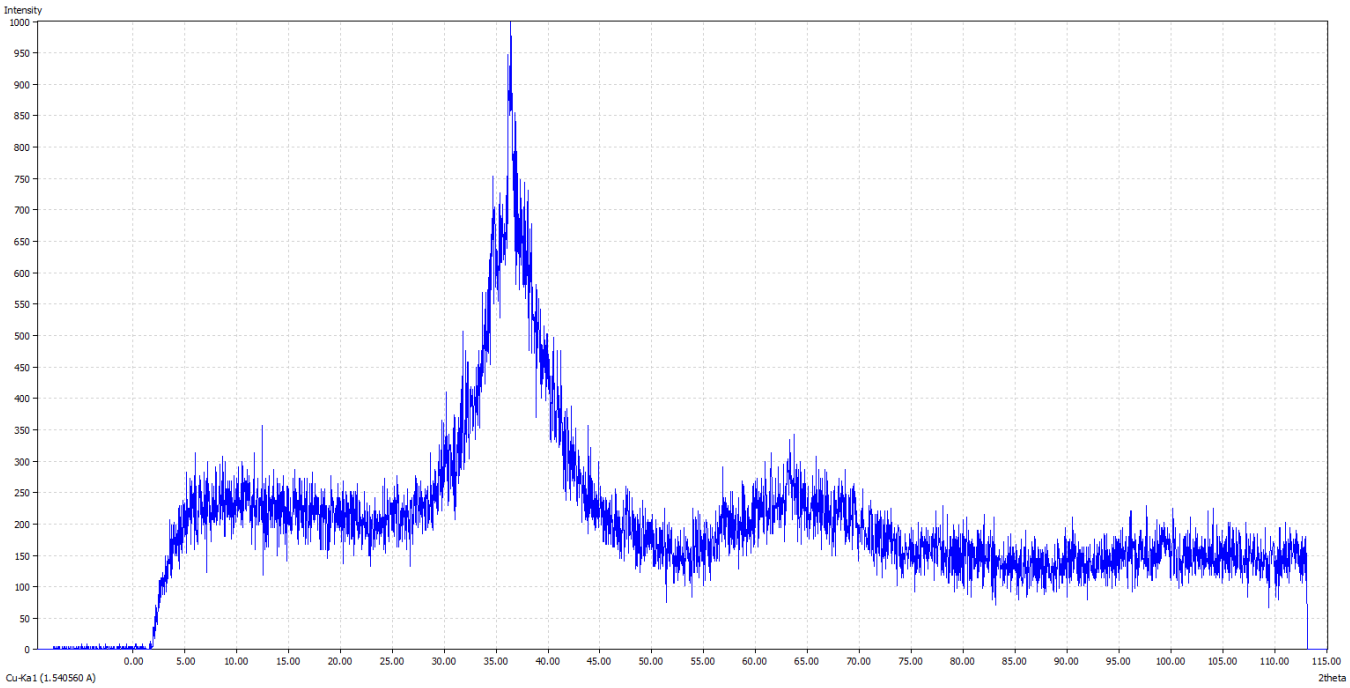

f, run 5

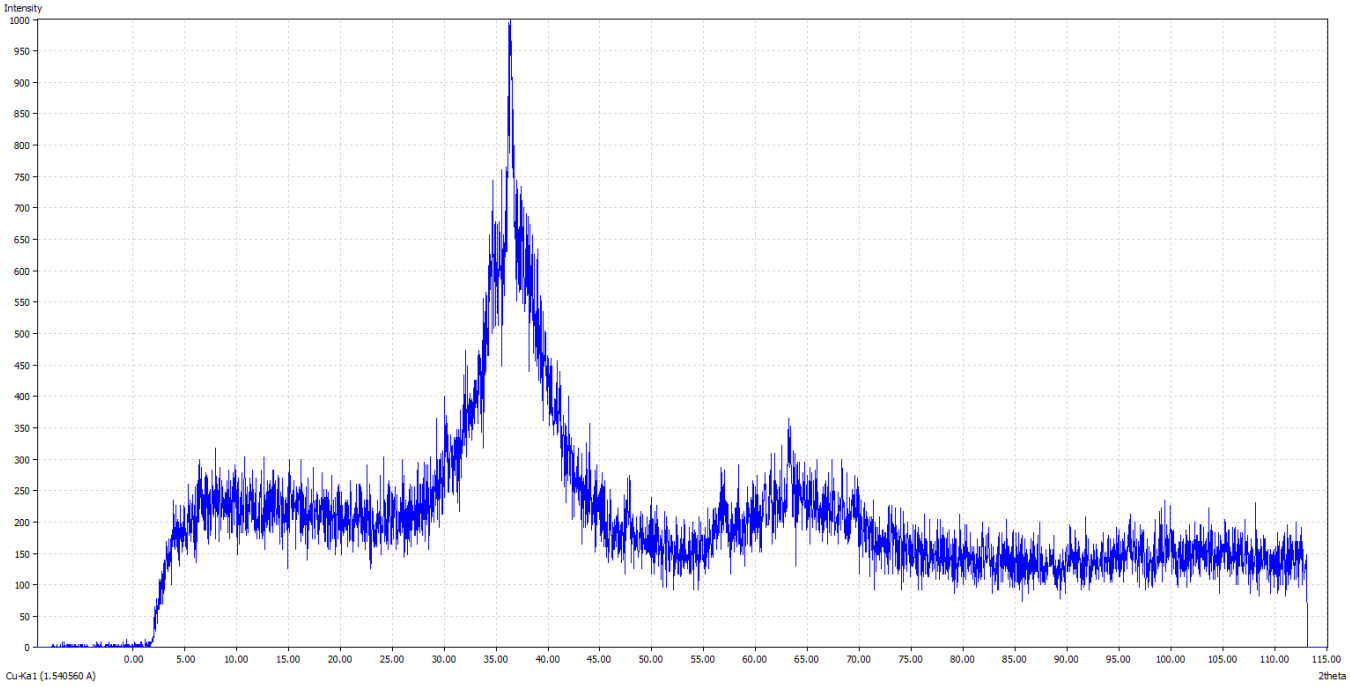

Figure 18. XRD pattern for field 2 after each annealing run: (a) no annealing, (b) run 1, (c) run 2, (d) run 3, (e) run 4 and (f) run 5

4.2.2.3 Surface Roughness

The surface roughness following each annealing run is shown in table 11. A pre-annealed roughness of 0.16 Ra µm was observed followed by an instant drop of 0.02 µm to 0.14 Ra µm. Following a total annealing time of 1000 seconds the roughness was measured at 0.17 Ra µm an increase of 0.01 µm.

Table 11. Taylor-Hobson surface roughness measurements for field 2 following each annealing run

Run	Surface Roughness (µm)
No annealing	0.16
1	0.14
2	0.14
3	0.14
4	0.15
5	0.17

4.3 In-situ hot stage optical microscopy

4.3.1 Experiment 1

Table 12 shows the temperatures and times at which each optical image was taken during the first hot stage experiment. A maximum temperature of 440^{o}C near the T_x for Vitreloy1b was used in order to create maximum viscous flow.

Table 12. Shows the temperatures and times at which each photograph was taken using the infinity 2 camera for experiment 1

Image	Temperature (^{o}C)	Total Time (seconds)
A	27	0
B	440	0
C	440	30
D	440	60
E	440	240
F	440	300
G	440	360
H	440	420

4.3.1.1 Surface Topography

The optical images taken during the first experiment are shown in Figure 19. Figure 19a shows the Vitreloy1b sample at 27^{o}C before annealing. Within this optical image the dark area represents the corner section of a protrusion created following the hot embossing using an aluminium mould with a 10kg indentation. A faint line leading from the bottom corner shows one edge of the replicated indent. The surface surrounding the protrusion shows a random arrangement and is non-uniform with several peaks and troughs. Unfortunately for all of these experiments scale bars are not present for the optical images however 3D Taylor-Hobson surface analysis is used to determine the size features.

Figures 19b to h show the subsequent images during the annealing of the Vitreloy1b sample. For each image it is clear that no changes to the shape or size of the protrusion occur. The only changes observed are in the colour of the material which gradually changes from a light grey colour before annealing to a bright pink colour after 420 seconds of annealing.

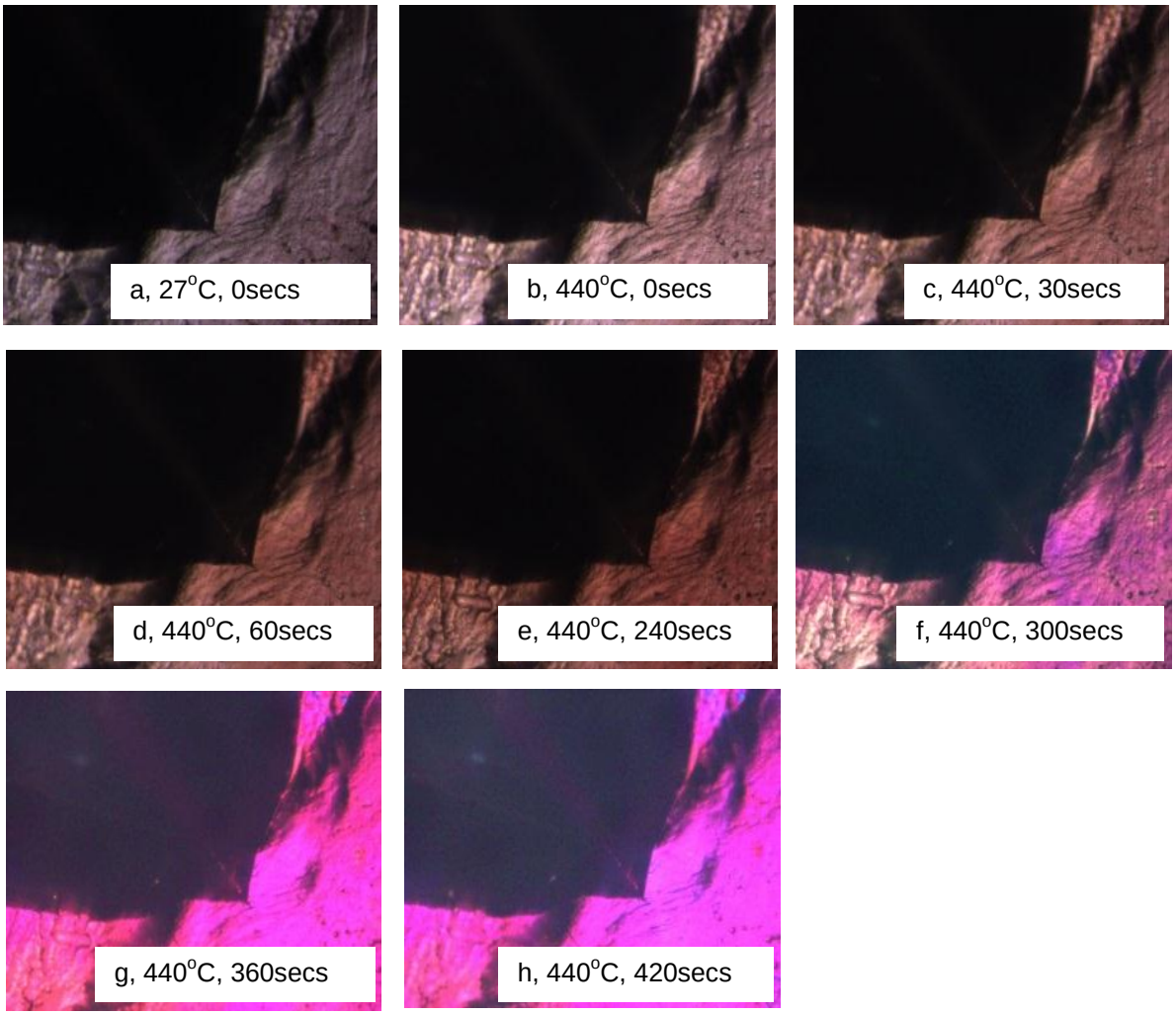

Figure 19. Optical images of Vitreloy1b alloy for experiment 1

4.3.1.2 3D Surface Roughness

Figure 20 shows the net shape analysis for the first in-situ hot stage experiment. Figure 20a shows the 3D Taylor-Hobson analysis of the aluminium mould used to create the BMG protrusion. A clear indent was created using a 10kg load. The width of this indent is approximately 600 µm and the maximum depth was calculated at 90.2 µm.

Unfortunately a 3D analysis of the Vitreloy1b sample was not performed immediately following hot embossing thus it is difficult to compare the effects. However the analysis

following annealing shown in Figure 20b shows that the embossing did create a protrusion and the width of this protrusion after annealing was approximately 580 µm and the maximum height 92.5 µm.

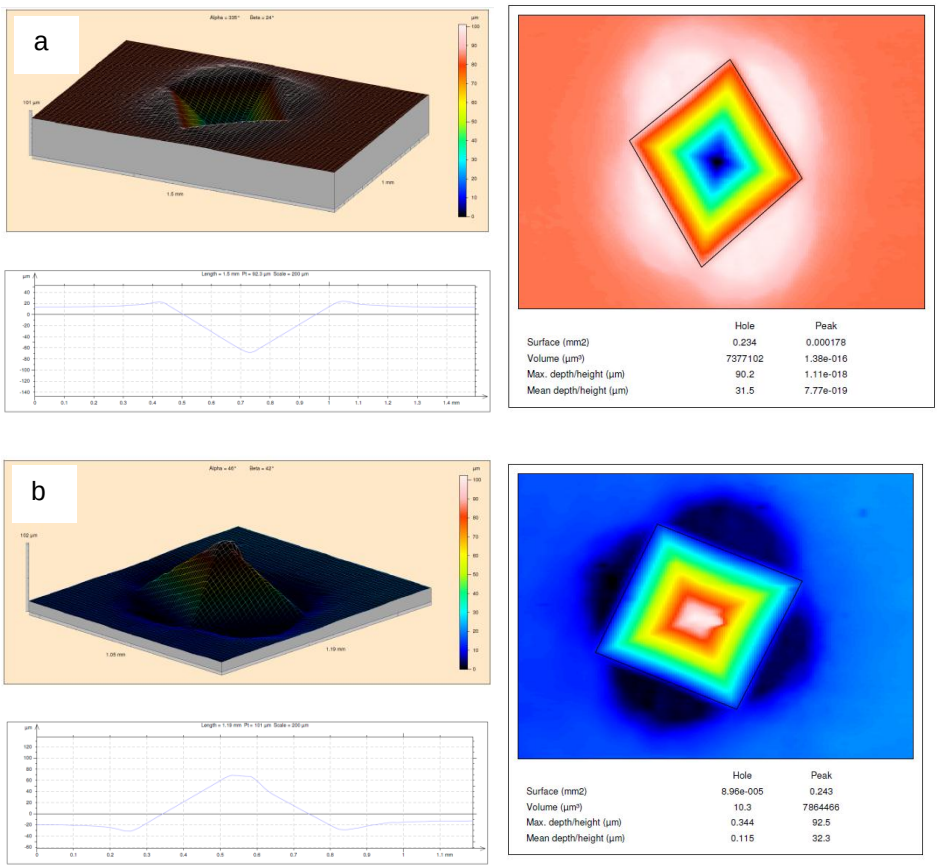

Figure 20. 3D Taylor-Hobson surface roughness measurements: (a) aluminium mould with 10kg indent, (b) Vitreloy1b sample with protrusion following annealing

4.3.2 Experiment 2

Table 13 shows the temperatures and times at which each optical image was taken during the second experiment. This experiment used an aluminium mould with a 1kg indent to create the Vitreloy1b sample tested. A high maximum temperature of 450^{o}C was used for this experiment and a maximum time of 660seconds.

The literature suggests that using such high temperatures and long durations the Vitreloy1b alloy will experience full crystallisation. However it was of scientific curiosity within this study to observe any changes to the surface topography even in the event of crystallisation.

Table 13. Shows the temperatures and times at which each photograph was taken using the infinity 2 camera for experiment 2

Image	Temperature (^{o}C)	Total Time (seconds)
A	40	0
B	450	0
C	450	60
D	450	120
E	450	180
F	450	240
G	450	360
H	450	420
I	450	480
J	450	540
K	450	600
I	450	660

4.3.2.1 Surface Topography

Figure 21 shows optical images of the annealed Vitreloy1b alloy for the second experiment. Figure 21a depicts the Vitreloy1b sample following hot embossing at a temperature of 40^{o}C. A black protrusion is seen within the centre of the image. From each corner of this protrusion a faint line is observed. These lines represent the edges of the protrusion and thus the pyramid shape created following hot embossing. A light area is observed at the centre of the protrusion suggesting the protrusion has a flat tip rather than a sharp point. Several other light areas are observed on the protrusion signifying the sides of the protrusion are not perfectly smooth. Figure 21 shows similar behaviour

to that observed in figure 19. As time increases, no obvious changes to the shape of the protrusion or surrounding microstructure are observed except a change in colour from light grey to pink/purple.

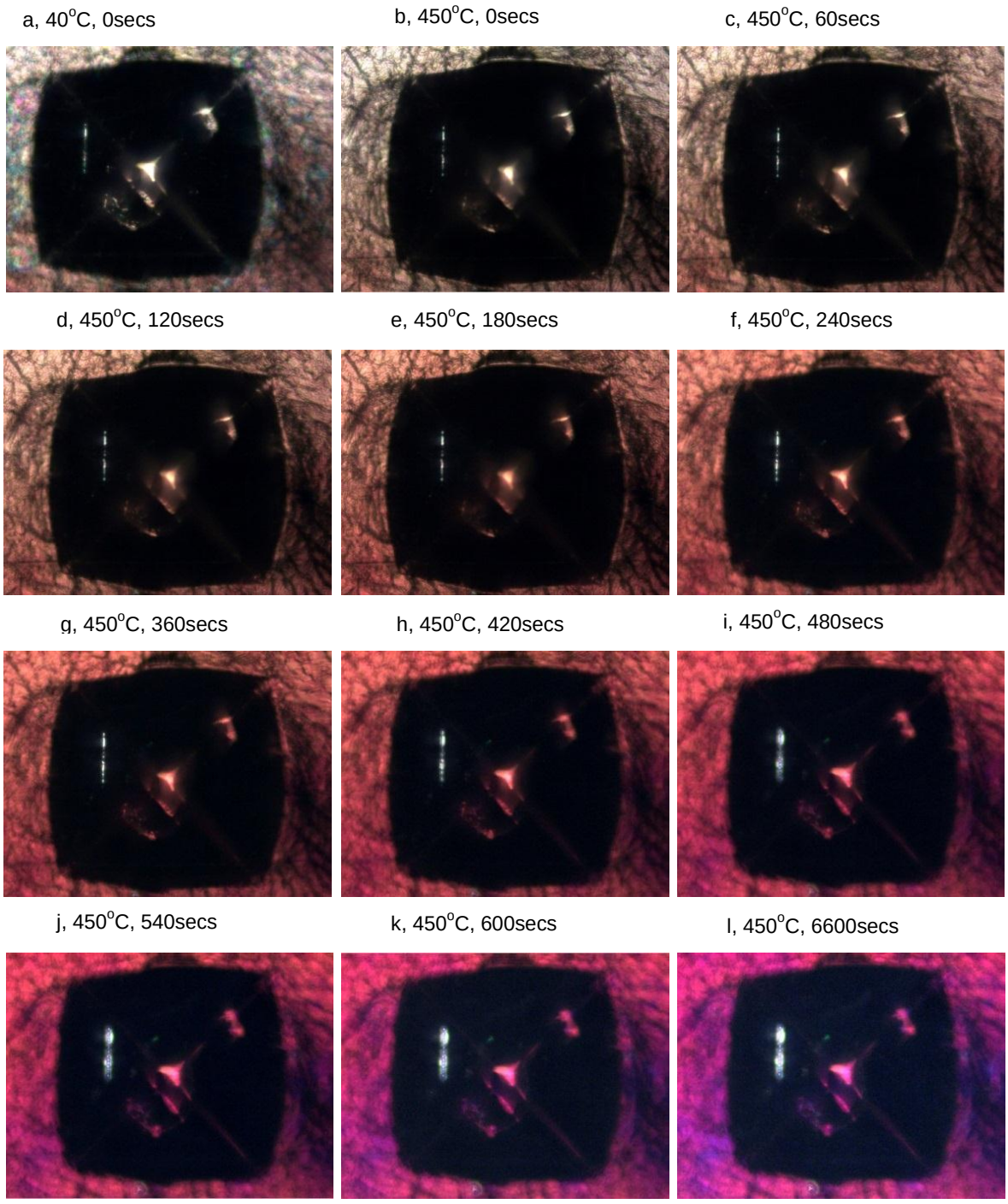

Figure 21. Optical images of Vitreloy1b alloy for experiment 2

4.3.2.2 3D Surface Roughness

Figure 22a shows the net shape analysis for the 1kg indented aluminium mould. It shows that an indentation with width of 174 µm and maximum depth of 25.4 µm was created. Again unfortunately a 3D analysis of the Vitreloy1b sample was not performed before annealing so it is difficult to compare the effects. The net shape analysis after annealing is shown in Figure 22b. A protrusion is observed with a width of 179 µm and a maximum height of 26.2 µm. Thus if perfect replication is assumed an increase in the width of the protrusion of 5 µm and an increase in height of 1.2 µm was observed.

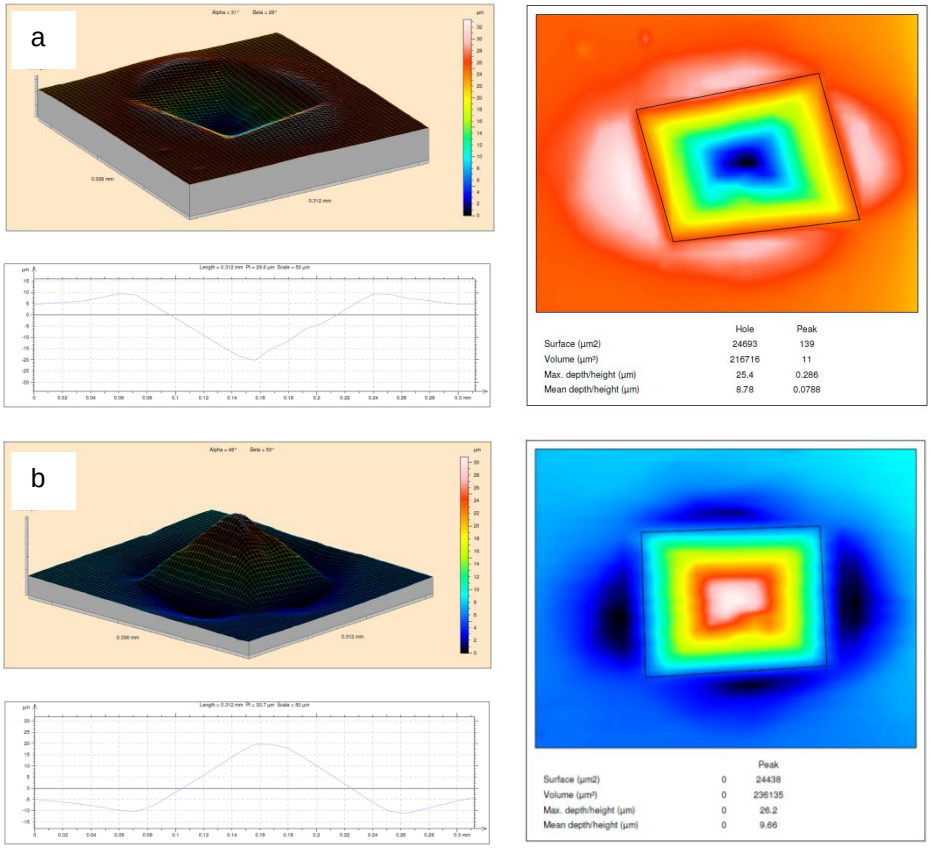

Figure 22. 3D Taylor-Hobson surface roughness measurements: (a) aluminium mould with 1kg indent, (b) Vitreloy1b samples with protrusion following embossing

4.3.3 Experiment 3

Table 11 shows the temperatures and times at which each photograph was taken during the third experiment. The sample used within this experiment was created from embossing the Vitreloy1b alloy into an aluminium mould with a 0.05kg indentation. A maximum temperature of 450^{o}C was used in order to create maximum viscous flow and a total time of 480seconds.

Table 14. Shows the temperatures and times at which each photograph was taken using the infinity 2 camera for experiment 3

Image	Temperature (^{o}C)	Total Time (seconds)
A	22	0
B	450	0
C	450	60
D	450	120
E	450	180
F	450	240
G	450	300
H	450	360
I	450	420
J	450	480

4.3.3.1 Surface Topography

Figure 23 shows optical images for the third experiment. Figure 23a shows a protrusion in the centre of the image with a white area in the centre of the protrusion. This suggests that the tip of the protrusion is flat rather than pointed. Some surface imperfections can be seen around the outside of the protrusion which may be due to insufficient polishing of the Vitreloy1b alloy before embossing. A similar story to experiments 1 and 2 is observed for the subsequent annealing images where again the shape of the protrusion

again does not change. Regrettably some focus issues and stage movement was experienced when taking the optical images for this experiment.

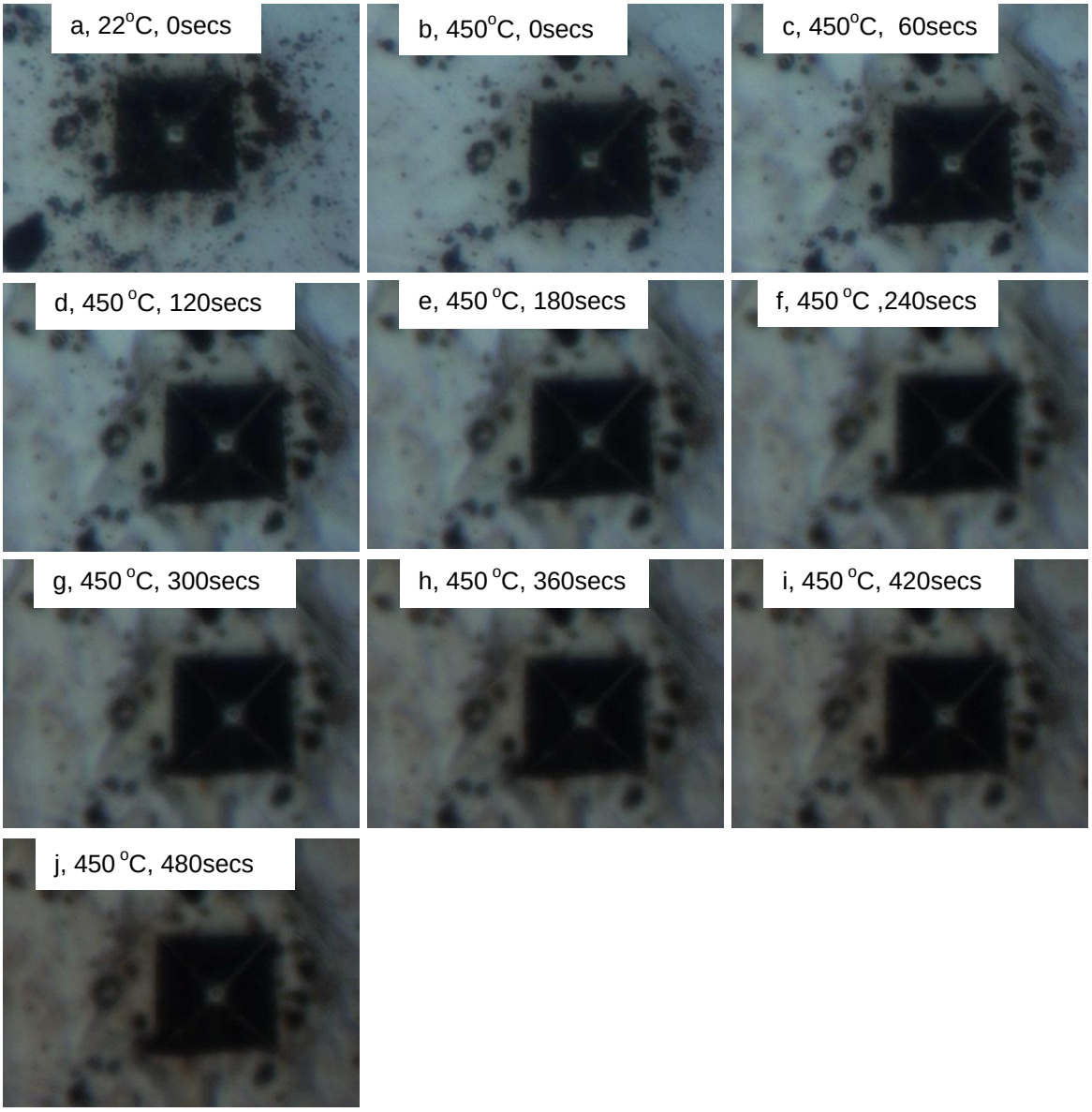

Figure 23. Optical images of Vitreloy1b alloy for experiment 3

4.3.3.2 3D Surface Roughness

Figure 24a shows the net shape analysis for the 0.05kg indented aluminium mould with a width of 70 µm and maximum depth of 6.49 µm. The analysis shows that the sides of the indent are not flat and the edges are in fact somewhat squashed.

Figure 24b shows the resulting Vitreloy1b sample following hot embossing and before annealing. It shows a protrusion with a width of 46 µm and maximum height of 4.59 µm. The analysis also shows a protrusion with a different shape to the indent. This suggests that the replication was not highly accurate. The difference in width between the indent and protrusion is 24 µm and the difference in maximum depth/height is 1.9 µm.

Figure 24c shows the protrusion following annealing. It shows that the width of the protrusion is 48 µm and the maximum height 4.31 µm. This represents an increase in 2 µm width from the original embossing and a reduction in height of 0.28 µm.

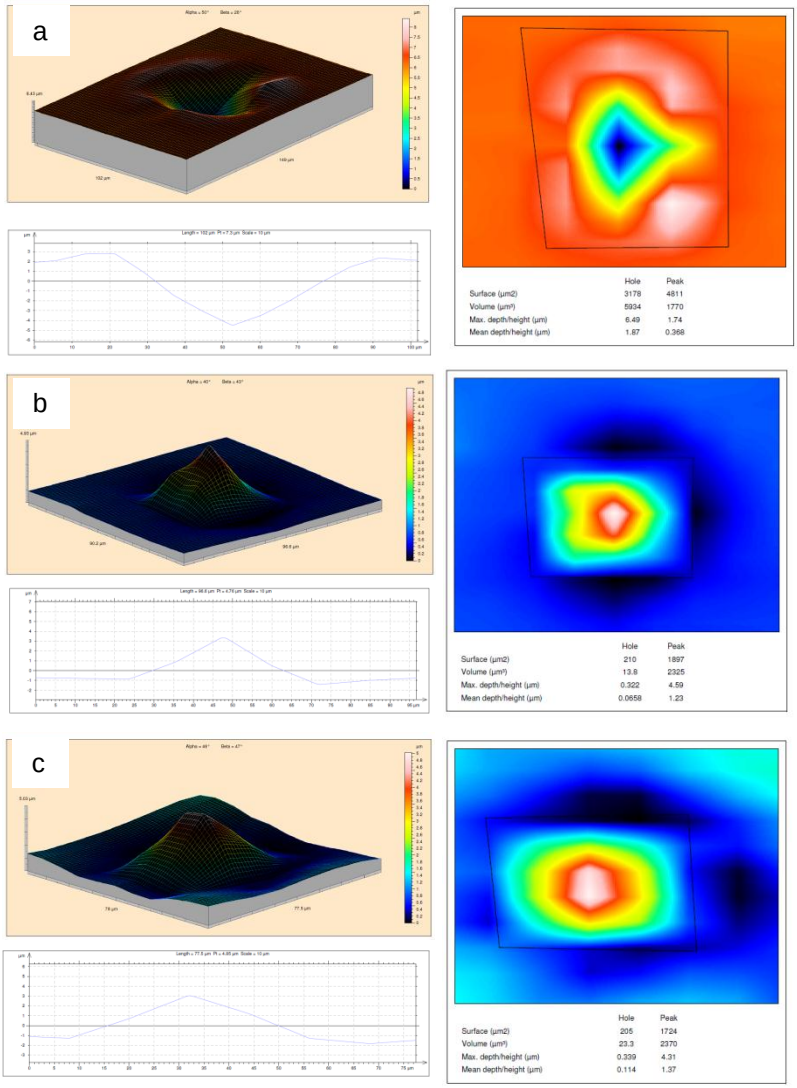

Figure 24. 3D Taylor-Hobson surface roughness measurements: (a) aluminium mould with 0.05kg indent, (b) Vitreloy1b sample with protrusion following embossing (c) Vitreloy1b sample with protrusion following annealing

4.3.4 Master table of results

Table 15. A master table of results for the in-situ hot stage experiments showing the differences in the depth of the original mould material and the height of each protrusion

	Width of indent µm	Depth of indent µm	Height of protrusion µm
Experiment 1			
Aluminium mould with 10 kg	600	90.2	
Vitreloy 1b alloy following annealing	580		92.5
Experiment 2			
Aluminium mould with 1 kg indent	174	25.4	
Vitreloy 1b alloy following annealing	179		26.2
Experiment 3			
Aluminium mould with 0.05 kg indent	70	6.49	
Vitreloy 1b alloy following embossing	46		4.59
Vitreloy 1b alloy following annealing	48		4.31

Figures 19, 21 and 23 show very little in terms of changes to the shape and size of each protrusion and the table 15 confirms this. Unfortunately, surface roughness measurements were not taken after the embossing stage in experiments 1 and 2 and thus the results are more difficult to interpret. It can be said however that if perfect replication of the indent occurred following embossing the height of the protrusion for each of these experiments did not decrease.

In experiment 3 the surface roughness measurements reveal a small decrease of 0.28 µm in the height of the protrusion following annealing. However, this is not visible in the

optical images. A more detailed explanation regarding these results is written in the following section.

5. DISCUSSION

5.1 Effect of laser machining

In the present study, it was observed that material removal occurred following ns pulsed laser ablation to the Vitreloy1b amorphous alloy shown in figures 11 a-c, figures 13 a-b and figures 13 e-h. The SEM images reveal that each field has its own unique set of features created by the different laser parameters. Changing these parameters will lead to changes in:

1. Thermal load
2. Shape and size of each crater
3. Amount of material removal
4. Surface roughness

In regards to the thermal load, the first set of annealing experiments caused some crystallisation to Vitreloy1b alloy. Whereas the second set of experiments showed negligible thermal effects and the material remained amorphous. The differences in the laser machining response can be attributed to the high peak powers used in the second set of experiments. It has been shown that increasing the peak power whilst maintaining the same pulse width can reduce the thermal load experienced by the material [75]. When using high peak powers the majority of the material is vaporised /ablated quickly meaning there is large exposed surface area for which cooling can take place. This means less heat is dissipated into the bulk of the material and the thermal load is reduced. When using lower peak powers on the other hand, less material is vaporised directly and molten material remains near the surface held by surface tension forces [78]. The heat on the surface dissipates into the bulk via heat diffusion thus increasing

the thermal load and causing the crystallisation behaviour observed in the first set of experiments.

The peak power of field 2 in the first set of experiments is similar to that of field 1 in the second. However, the differences in thermal diffusion can be explained by the lower pulse frequency and the higher track distance used in the second set of experiments. Field 2 in first set of experiments has a track distance of 6µm and a frequency of 250 kHz whereas field 1 in the second experiment has a track distance of 10 µm and frequency of 100 kHZ. A lower track distance suggests that more heat is subjected to the same area on the Vitreloy1b surface therefore the material experiences more heat dissipation. Additionally and high pulse frequency rate suggests that more pulses are exerted onto the material over a certain time which will also increase the thermal load.

The conditions for ns laser machining are summarized in figure 25 [84].The absorbed energy from each ns pulse melts and heats the material to a temperature where the atoms gain sufficient energy to become gaseous. At this temperature there is enough time for a thermal wave to propagate. Subsequent evaporation occurs from the liquid state of the material and molten material is ejected from the cavity by vapour and plasma pressure in the form of drops. Some of these drops fall back onto the surface and create debris spoiling the surface. A closely related occurrence is the formation of a recast layer after the heat has dissipated into the material which can be seen in figure 25.

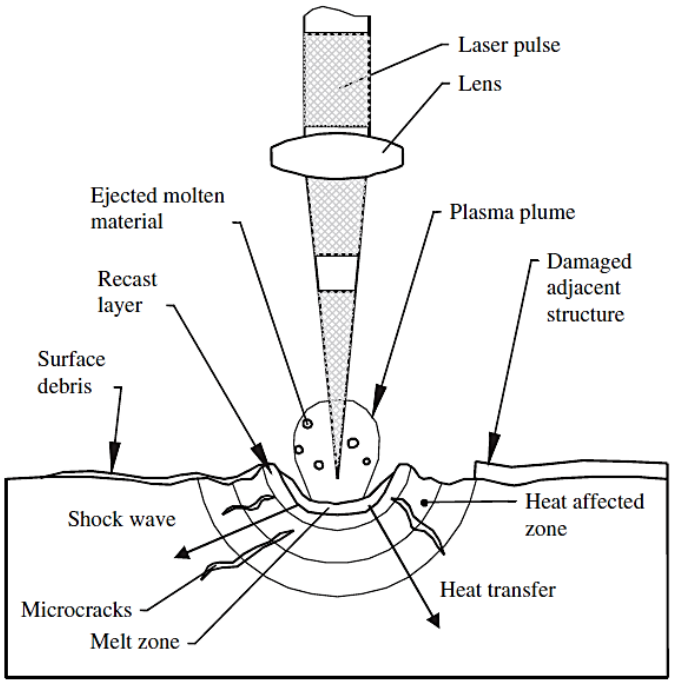

Figure 25. Nanosecond and microsecond laser machining [78]

The secondary effects associated with ns and longer pulses include a heat-affected zone, recast layer, microcracks and debris caused by the ejection of material [78]. In this study material ejection from the crater is particularly noticeable in figures 11 a and b where large craters can be observed. Additionally very little re-deposited material is observed around the edges of these craters. Figures 11c, 13e and 13h on the other hand display more re-deposited material around the edges of each crater. This can be explained by more concentrated heating and therefore more molten material is partially ejected by vapour and plasma pressure. Similar behaviour has been observed in the laser machining of Ni-based BMGs [17].

Figures 13 a, b, c, d, f, and g show a different surface morphology altogether. Instead they show behaviour which can be explained by the laser parameters used to create

these fields. This study proposes that the short pulse lengths reduce the amount of material removal and thus tracks are not so visible in the second set of experiments. Furthermore, the higher laser power intensity used results in greater material splashing and builds a ragged recast layer. Future research should focus on finding the best compromise of parameters to produce a surface roughness on the nanometer scale instead of the micron scale witnessed in this study.

Although relatively small, there are also differences in the resulting surface roughness. When comparing the best results from the two sets of experiments there is a 0.1 µm difference. For the first set the best Ra is 0.16 µm and for the second set of results 0.26 µm. Those fields where the most splashes observed correspond to those with the largest surface roughness whereas those fields with the most uniform structure show the least amount of debris material around each crater.

Previous studies have shown that fs and ps lasers could be successfully used to ablate the surface of BMGs with negligible thermal effects [17, 19-21]. However only minimal research has been conducted using ns and ms onto BMGs [17, 18]. In order to understand further and be able to machine very smooth surfaces without affecting the short-range atomic ordering of the Vitreloy1b alloy, a systematic approach towards ns machining onto amorphous alloys is required to find the optimal laser settings.

5.2 Effect of annealing

This study showed that the surface roughness of Vitreloy1b samples created by laser machining did not change after 2 annealing trials using a hot plate setup. Kumar et al. on the other hand showed that features imprinted into a Pt-based alloy could be erased

under the action of surface tension forces during annealing in the SCLR[1]. Several possible explanations for the differences seen in results are discussed in this section.

The first explanation looks at the different material viscosities between the two materials used within each study. Kumar et al calculated that the viscosity of the Pt-based alloy at their annealing temperature of 270^{o}C was in the range of 1-4 10^{7} Pa s. Whereas the viscosities of the Vitreloy1b alloy used within this study were 2-3 10^{10} Pa s at 380^{o}C and 7-8 10^{9} Pa s at 400^{o}C. (These viscosities were calculated using figure 4). Figure 4 shows that lower viscosities are associated with improved mould filling. It is therefore likely that the temperatures used to conduct these annealing experiments do not lower the viscosity enough for any smoothing behaviour to occur. Instead the sluggish kinetics associated with high viscosities prevent the material from flowing and having a smoothening effect.

The SEM images for these experiments reveal no changes to the colour of the Vitreloy1b surface up to temperatures of 400^{o}C. This suggests that oxidation effects have not taken place when processing the Zr-based alloy in air. The negligible oxidation effects observed at this temperature may also explain why no further crystallisation was observed when performing hot plate annealing.

Low annealing temperatures were chosen for this study in order to avoid crystallisation and retain the short range atomic ordering due to the availability and cost of the samples. Future studies may benefit from using higher temperatures nearer the T_x where the viscosities are comparable to that of the Pt-based alloy.

Another justification for no smoothening effect may be the experimental setup. The laboratory hot plate setup may not have been completely accurate. Although a thermocouple was used to measure the temperature of the steel block, the fast heat cube did experience some issues during practice experiments whereby it was fluctuating on and off. An infrared thermocouple may have improved accuracy and enabled faster temperature readings of the surface of the steel block. Furthermore, the cooling of the Vitreloy1b samples after each annealing run may have affected the results. The method of cooling used for this study involved placing the annealed samples immediately onto an aluminium block which was half submerged in cold water. This may have cooled the material quickly and prevented any smoothening behaviour to take effect. Further experimental analysis would be beneficial to see if the quick cooling of samples changes the viscous flow of the material.

A further factor which needs to be considered is whether or not the presence of some crystalline phases caused by laser machining affected the annealing runs. Although the XRD analysis shown in the results section figures 16 and 18 show no changes to the crystalline structure further analysis is needed to understand if the presence of some crystalline phases could affect the flow behaviour of the material when reheated to within the SCLR.

An analysis of the Vitreloy1b amorphous alloy with a fully amorphous microstructure heated to 440^{o}C using the same experimental setup would be beneficial to identify if the hot plate annealing technique is viable to observe any smoothening effect.

5.3 Hot embossing replication

Unfortunately 3d Taylor-Hobson analysis was only performed after embossing for experiment 3; therefore it is difficult to discuss the replication ability. Figures 24 a and b show the indentation before embossing for experiment 3 and the protrusion on the Vitreloy1b following embossing. The 3D Taylor-Hobson analysis shows before embossing the maximum depth of the mould was 6.49 µm whereas the height of the protrusion following embossing measured 4.59 µm. Thus a difference in replicated height of 1.9 µm was observed.

Using the same Vitreloy1b material used within this study and a similar TPF processing previous studies have reported replication of feature sizes down to 30nm (TPF of BMG). The study suggests that in order to replicate features with high aspect ratios high temperatures near the T_x and high pressures are required in order to maximise mould filling.

5.4 Effect of In-situ hot stage microscopy

For the in-situ hot stage microscopy, testing was performed at higher temperatures (440^{o}C and 450^{o}C) nearer the T_x. The viscosity for Vitreloy1b at 440^{o}C is 8-9 10^7 Pa s and 2-4 10^7 Pa s at 450^{o}C calculated using figure 4. These viscosities are much closer to the viscosity of the material used within the Kumar et al study. By increasing the annealing temperature this also decreases the time before crystallisation therefore shorten the available processing time.

The optical images, shown in figures 19, 21 and 23 show that for each of the 3 experiments no visual changes to the shape or size of each protrusion occurred as a function of time.

These findings may be explained due to oxidation effects. At the higher temperatures used in these experiments clear changes to the colour of the Vitreloy1b alloy were observed (figures 19 and 21). Several previous studies have shown that when processing Zr-based alloys within air they show a low resistance to oxidation [68, 85]. It has also been reported that some materials experience a change in colour following annealing which is associated with oxidation [68].

This study proposes that the presence of oxidation caused by heating the Vitreloy1b alloy at high temperatures increased the viscosity of the surface material and therefore prevented any smoothening behaviour. A study which investigated the influence of changing the oxygen content of a $Zr_{65}Al_{7.5}Cu_{17.5}Ni_{10}$ amorphous alloy found that even small increases in oxygen content (more than 1 at.%) lead to increases in the viscosity[86].

Additionally, this study proposes that the oxidation may have also affected the materials susceptibility to crystallisation. Unfortunately, XRD analysis was not performed on the samples following hot stage microscopy so this cannot be guaranteed. Future studies should focus on this in order to validate oxidation. If oxidation has occurred the XRD trace is likely to show peaks representative of ZrO_2. Several studies, including a study investigating Vitreloy1b have shown that the presence of crystalline precipitates

increase the material viscosity [87, 88] . This increase in viscosity may also be accountable for no observed smoothening behaviour.

Comparing the Vitreloy1b alloy used in this study to the Pt-based alloy in the Kumar et al study these alloys have been shown to have a good resistance to oxidation [34, 68]. [15] In addition a further study which looked at the smoothening behaviour of a Pt-based amorphous alloy and a Zr-based amorphous alloy showed that the Pt-based alloy could be automatically smoothed during TPF. The study suggests that the effectiveness of the smoothening process depends on oxide removal which is determined by the relationship between the time scale for surface oxidation and the inverse strain rate. In order for a smooth surface the contamination time needs to be longer than the timescale for oxide removal. They suggest that this requirement is not fulfilled by the Zr-based alloy which shows a fast oxidation rate.

Finally, a decrease in height of 0.28 μm was observed in experiment 3 following annealing. This may suggest that some smoothening behaviour took place. However this decrease in height is not a resounding result and further experiments using smaller protrusions would be highly beneficial towards further understanding.

6. CONCLUSIONS

This study demonstrated that ns pulse laser machining is a viable method for micromaching Zr-based bulk metallic glasses whilst retaining the highly desirable amorphous structure. The longer pulses associated with ns processing maybe beneficial over ultra-short pulses such as femto and pico-second lasers because ns pulses can remove larger amounts of material and can be performed at much lower costs.

In order to understand fully the laser-material effects more experiments are necessary. In particular these experiments should focus on optimising the parameters in order to increase the material removal rate, improve machining times and produce smoother surfaces.

Additionally this study performed two annealing techniques to Vitreloy1b samples within the SCLR. It was shown that the hot plate annealing could be performed without causing crystallisation however no smoothening effect was observed due to the high viscosity of the alloy at the temperatures tested.

The second method explored the use of in-situ hot stage microscopy. This study revealed that oxidation occurs when heating the Vitreloy1b sample in air and this may have affected the viscous flow of the material. One of the experiments showed a decrease in the height of a protrusion by 0.28µm following annealing. This suggests some smoothening behaviour took place however further research with the use of smaller features is needed to validate this process.

7. FUTURE WORK

Future work should focus on optimising the laser machining parameters to create a system whereby changes to the surface integrity can be controlled whilst ensuring the highly desirable amorphous structure is retained.

Repeated testing of the in-situ hot stage microscopy trails performed in this study would be beneficial. However these trials should ensure that 3D Taylor-Hobson surface roughness measurements are taken at all stages in order to analyse any shape changes. XRD analysis should also be performed before and after each experiment to ensure the material remains amorphous.

Furthermore, in-situ hot stage microscopy trials under vacuum should be studied. These trials would eliminate the issues associated with oxidation of the Vitreloy1b alloy and may allow the smoothening effect to be observed.

8. LIST OF REFERENCES

[1] G. Kumar and J. Schroers, "Write and erase mechanisms for bulk metallic glass," *Applied Physics Letters,* vol. 92, pp.031901-1 -031901-3, Jan 21 2008.

[2] W. H. Wang, C. Dong, and C. H. Shek, "Bulk metallic glasses," *Materials Science & Engineering R-Reports,* vol. 44, pp. 45-89, Jun 2004.

[3] A. Inoue, "Stabilization of metallic supercooled liquid and bulk amorphous alloys," *Acta Materialia,* vol. 48, pp. 279-306, 2000.

[4] J. Schroers, Q. Pham, and A. Desai, "Thermoplastic Forming of Bulk Metallic Glass - A Technology for MEMS and Microstructure Fabrication," *Microelectromechanical Systems, Journal of,* vol. 16, pp. 240-247, 2007.

[5] J. Schroers, B. Lohwongwatana, W. L. Johnson, and A. Peker, "Precious bulk metallic glasses for jewelry applications," *Materials Science and Engineering a-Structural Materials Properties Microstructure and Processing,* vol. 449, pp. 235-238, Mar 2007.

[6] J. Schroers, "The superplastic forming of bulk metallic glasses," *Jom,* vol. 57, pp. 35-39, May 2005.

[7] J. Schroers, Q. Pham, A. Peker, N. Paton, and R. V. Curtis, "Blow molding of bulk metallic glass," *Scripta Materialia,* vol. 57, pp. 341-344, Aug 2007.

[8] Y. Kawamura, H. Kato, A. Inoue, and T. Masumoto, "Effects of extrusion conditions on mechanical properties in Zr-Al-Ni-Cu glassy powder compacts," *Materials Science and Engineering a-Structural Materials Properties Microstructure and Processing,* vol. 219, pp. 39-43, Nov 1996.

[9] D. J. Sordelet, E. Rozhkova, P. Huang, P. B. Wheelock, M. F. Besser, M. J. Kramer, M. Calvo-Dahlborg, and U. Dahlborg, "Synthesis of Cu47Ti34Zr11Ni8 bulk metallic glass by warm extrusion of gas atomized powders," *Journal of Materials Research,* vol. 17, pp. 186-198, Jan 2002.

[10] Y. Saotome, K. Itoh, T. Zhang, and A. Inoue, "Superplastic nanoforming of Pd-based amorphous alloy," *Scripta Materialia,* vol. 44, pp. 1541-1545, 2001.

[11] Y. Saotome, S. Miwa, T. Zhang, and A. Inoue, "The micro-formability of Zr-based amorphous alloys in the supercooled liquid state and their application to micro-dies," *Journal of Materials Processing Technology,* vol. 113, pp. 64-69, 2001.

[12] P. Sharma, N. Kaushik, H. Kimura, Y. Saotome, and A. Inoue, "Nano-fabrication with metallic glass - an exotic material for nano-electromechanical systems," *Nanotechnology,* vol. 18, Jan 2007.

[13] J. P. Chu, H. Wijaya, C. W. Wu, T. R. Tsai, C. S. Wei, T. G. Nieh, and J. Wadsworth, "Nanoimprint of gratings on a bulk metallic glass," *Applied Physics Letters,* vol. 90, pp. 034101, Jan 2007.

[14] C. E. Packard, J. Schroers, and C. A. Schuh, "In situ measurements of surface tension-driven shape recovery in a metallic glass," *Scripta Materialia,* vol. 60, pp. 1145-1148, 2009.

[15] G. Kumar, P. A. Staffier, J. Blawzdziewicz, U. D. Schwarz, and J. Schroers, "Atomically smooth surfaces through thermoplastic forming of metallic glass," *Applied Physics Letters,* vol. 97, pp. 101907, 2010.

[16] M. Bakkal, A. J. Shih, S. B. McSpadden, C. T. Liu, and R. O. Scattergood, "Light emission, chip morphology, and burr formation in drilling the bulk

metallic glass," *International Journal of Machine Tools and Manufacture,* vol. 45, pp. 741-752, 2005.

[17] I. Quintana, T. Dobrev, A. Aranzabe, G. Lalev, and S. Dimov, "Investigation of amorphous and crystalline Ni alloys response to machining with micro-second and pico-second lasers," *Applied Surface Science,* vol. 255, pp. 6641-6646, 2009.

[18] H. Lin, C. Lee, T. Hu, C. Li, and J. C. Huang, "Pulsed laser micromachining of Mg–Cu–Gd bulk metallic glass," *Optics and Lasers in Engineering,* vol. 50, pp. 883-886, 2012.

[19] X. Wang, P. Lu, N. Dai, Y. Li, C. Liao, Q. Zheng, and L. Liu, "Noncrystalline micromachining of amorphous alloys using femtosecond laser pulses," *Materials Letters,* vol. 61, pp. 4290-4293, 2007.

[20] W. Jia, Z. Peng, Z. Wang, X. Ni, and C. y. Wang, "The effect of femtosecond laser micromachining on the surface characteristics and subsurface microstructure of amorphous FeCuNbSiB alloy," *Applied Surface Science,* vol. 253, pp. 1299-1303, 2006.

[21] F. Ma, J. Yang, Z. Xiaonong, C. Liang, and H. Wang, "Femtosecond laser-induced concentric ring microstructures on Zr-based metallic glass," *Applied Surface Science,* vol. 256, pp. 3653-3660, 2010.

[22] W. Klement, R. H. Willens, and P. Duwez, "Non-Crystalline Structure in Solidified Gold-Silicon Alloys," *Nature,* vol. 187, pp. 869-870, 1960 1960.

[23] D. Turnbull, "Under Whar Conditions Can A Glass Be Formed," *Contemporary Physics,* vol. 10, p. 473, 1969.

[24] H. S. Chen and D. Turnbull, "Formation, Stability and Structure of Palladium-Silicon Based Alloy Glasses," *Acta Metallurgica,* vol. 17, pp. 1021-&, 1969.

[25] H. S. Chen, "Thermodynamic considerations on the formation and stability of metallic glasses," *Acta Metallurgica,* vol. 22, pp. 1505-1511, 1974.

[26] H. W. Kui, A. L. Greer, and D. Turnbull, "Formation of Bulk Metallic0Glass by Fluxing," *Applied Physics Letters,* vol. 45, pp. 615-616, 1984 1984.

[27] A. J. Drehman, A. L. Greer, and D. Turnbull, "Bulk formation of a metallic glass: Pd40Ni40P 20," *Applied Physics Letters,* vol. 41, pp. 716-717, 1982.

[28] A. Inoue, T. Zhang, and T. Masumoto, "Al-La-Ni Amorphous-alloys with a Wide Supercooled Liquid Region," *Materials Transactions Jim,* vol. 30, pp. 965-972, Dec 1989.

[29] A. Inoue, K. Ohtera, K. Kita, and T. Masumoto, "New Amorphous Mg-Ce-Ni Alloys with High-Strength and Good Ductility," *Japanese Journal of Applied Physics Part 2-Letters,* vol. 27, pp. L2248-L2251, Dec 1988.

[30] A. Inoue, T. Zhang, and T. Masumoto, "Amorphous-alloys with High Glass-transition Temperature and Significant Supercooled Liquid Region," *Materials Transactions Jim,* vol. 31, pp. 177-183, Mar 1990.

[31] A. Peker and W. L. Johnson, "A Highly Processable Metallic-Glass - Zr41.2Ti13.8Cu12.5Ni10.0Be22.5," *Applied Physics Letters,* vol. 63, pp. 2342-2344, Oct 1993.

[32] V. Ponnambalam, S. J. Poon, and G. J. Shiflet, "Fe-based bulk metallic glasses with diameter thickness larger than one centimeter," *Journal of Materials Research,* vol. 19, pp. 1320-1323, May 2004.

[33] Z. P. Lu, C. T. Liu, J. R. Thompson, and W. D. Porter, "Structural amorphous steels," *Physical Review Letters,* vol. 92, pp. 049901, Jun 2004.

[34] J. Schroers and W. L. Johnson, "Highly processable bulk metallic glass-forming alloys in the Pt-Co-Ni-Cu-P system," *Applied Physics Letters,* vol. 84, pp. 3666-3668, May 2004.
[35] A. Inoue, N. Nishiyama, K. Amiya, T. Zhang, and T. Masumoto, "Ti-Based Amorphous Alloys with a Wide Supercooled Liquid Region," *Materials Letters,* vol. 19, pp. 131-135, Apr 1994.
[36] Y. C. Kim, W. T. Kim, and D. H. Kim, "A development of Ti-based bulk metallic glass," *Materials Science and Engineering: A,* vol. 375–377, pp. 127-135, 2004.
[37] A. Inoue, W. Zhang, T. Zhang, and K. Kurosaka, "High-strength Cu-based bulk glassy alloys in Cu-Zr-Ti and Cu-Hf-Ti ternary systems," *Acta Materialia,* vol. 49, pp. 2645-2652, Aug 2001.
[38] C. L. Dai, H. Guo, Y. Shen, Y. Li, E. Ma, and J. Xu, "A new centimeter-diameter Cu-based bulk metallic glass," *Scripta Materialia,* vol. 54, pp. 1403-1408, Apr 2006.
[39] J. F. Li, D. Q. Zhao, M. L. Zhang, and W. H. Wang, "CaLi-based bulk metallic glasses with multiple superior properties," *Applied Physics Letters,* vol. 93, pp. 171907, Oct 2008.
[40] B. Zhang, D. Q. Zhao, M. X. Pan, W. H. Wang, and A. L. Greer, "Amorphous metallic plastic," *Physical Review Letters,* vol. 94, May 2005.
[41] A. Inoue, A. Kato, T. Zhang, S. G. Kim, and T. Masumoto, "Mg-Cu-Y Amorphoys-alloys with High Mechanical Strengths Produced by a Metallic Mold Casting Method," *Materials Transactions Jim,* vol. 32, pp. 609-616, Jul 1991.
[42] H. Ma, J. Xu, and E. Ma, "Mg-based bulk metallic glass composites with plasticity and high strength," *Applied Physics Letters,* vol. 83, pp. 2793-2795, Oct 2003.
[43] J. Schroers, B. Lohwongwatana, W. L. Johnson, and A. Peker, "Gold based bulk metallic glass," *Applied Physics Letters,* vol. 87, Aug 2005.
[44] R. Busch, "The thermophysical properties of bulk metallic glass-forming liquids," *Jom-Journal of the Minerals Metals & Materials Society,* vol. 52, pp. 39-42, Jul 2000.
[45] D. Turnbull, "Under What Conditions Can A Glass Be Formed," *Contemporary Physics,* vol. 10, p. 473, 1969.
[46] A. Inoue, "High-Strength Bulk Amorphous-Alloys with Low Critical Cooling Rates," *Materials Transactions Jim,* vol. 36, pp. 866-875, Jul 1995.
[47] A. L. Greer, "Confusion by design," *Nature,* vol. 366, pp. 303-304, 1993.
[48] C. A. Angell, "Formation of Glasses from Liquids and Biopolymers," *Science,* vol. 267, pp. 1924-1935, Mar 1995.
[49] W. L. Johnson, "Bulk glass-forming metallic alloys: Science and technology," *Mrs Bulletin,* vol. 24, pp. 42-56, Oct 1999.
[50] J. Schroers, "Bulk metallic glasses," *Physics Today,* vol. 66, pp. 32-37, 2013.
[51] J. Das, M. B. Tang, K. B. Kim, R. Theissmann, F. Baier, W. H. Wang, and J. Eckert, "“Work-Hardenable” Ductile Bulk Metallic Glass," *Physical Review Letters,* vol. 94, p. 205501, 2005.
[52] J. Schroers and W. L. Johnson, "Ductile Bulk Metallic Glass," *Physical Review Letters,* vol. 93, p. 255506, 2004.

[53] Y. H. i. Liu, G. Wang, R. J. Wang, D. Q. Zhao, M. X. Pan, and W. H. Wang, "Super Plastic Bulk Metallic Glasses at Room Temperature," *Science*, vol. 315, pp. 1385-1388, 2007.

[54] L. Y. Chen, Z. D. Fu, G. Q. Zhang, X. P. Hao, Q. K. Jiang, X. D. Wang, Q. P. Cao, H. Franz, Y. G. Liu, H. S. Xie, S. L. Zhang, B. Y. Wang, Y. W. Zeng, and J. Z. Jiang, "New Class of Plastic Bulk Metallic Glass," *Physical Review Letters*, vol. 100, p. 075501, 2008.

[55] K. F. Yao, F. Ruan, Y. Q. Yang, and N. Chen, "Superductile bulk metallic glass," *Applied Physics Letters*, vol. 88, 2006.

[56] B. E. Schuster, Q. Wei, M. H. Ervin, S. O. Hruszkewycz, M. K. Miller, T. C. Hufnagel, and K. T. Ramesh, "Bulk and microscale compressive properties of a Pd-based metallic glass," *Scripta Materialia*, vol. 57, pp. 517-520, 2007.

[57] C. A. Volkert, A. Donohue, and F. Spaepen, "Effect of sample size on deformation in amorphous metals," *Journal of Applied Physics*, vol. 103, 2008.

[58] J. F. Loffler, "Bulk metallic glasses," *Intermetallics*, vol. 11, pp. 529-540, Jun 2003.

[59] R. D. Conner, A. J. Rosakis, W. L. Johnson, and D. M. Owen, "Fracture toughness determination for a beryllium-bearing bulk metallic glass," *Scripta Materialia*, vol. 37, pp. 1373-1378, 1997.

[60] J. Schroers and N. Paton, "Amorphous metal alloys form like plastics," *Advanced Materials & Processes*, vol. 164, pp. 61-63, Jan 2006.

[61] A. Inoue and T. Zhang, "Fabrication of Bulky Zr-Based Glassy Alloys by Suction Casting onto Copper Mold," *Materials Transactions Jim*, vol. 36, pp. 1184-1187, Sep 1995.

[62] J. Schroers, "Processing of Bulk Metallic Glass," *Advanced Materials*, vol. 22, pp. 1566-1597, Apr 2010.

[63] J. P. Patterson and D. R. H. Jones, "Molding of a Metallic Glass," *Materials Research Bulletin*, vol. 13, pp. 583-585, 1978.

[64] Y. Saotome, K. Imai, S. Shioda, S. Shimizu, T. Zhang, and A. Inoue, "The micro-nanoformability of Pt-based metallic glass and the nanoforming of three-dimensional structures," *Intermetallics*, vol. 10, pp. 1241-1247, Nov-Dec 2002.

[65] T. Waniuk, J. Schroers, and W. L. Johnson, "Timescales of crystallization and viscous flow of the bulk glass-forming Zr-Ti-Ni-Cu-Be alloys," *Physical Review B*, vol. 67, May 2003.

[66] J. Schroers, T. Nguyen, S. O'Keeffe, and A. Desai, "Thermoplastic forming of bulk metallic glass - Applications for MEMS and microstructure fabrication," *Materials Science and Engineering a-Structural Materials Properties Microstructure and Processing*, vol. 449, pp. 898-902, Mar 2007.

[67] G. Kumar, A. Desai, and J. Schroers, "Bulk Metallic Glass: The Smaller the Better," *Advanced Materials*, vol. 23, pp. 461-476, 2011.

[68] J. Schroers, "On the formability of bulk metallic glass in its supercooled liquid state," *Acta Materialia*, vol. 56, pp. 471-478, 2008.

[69] G. Kumar, H. X. Tang, and J. Schroers, "Nanomoulding with amorphous metals," *Nature*, vol. 457, pp. 868-872, 2009.

[70] Y. Saotome, K. Itoh, T. Zhang, and A. Inoue, "Superplastic nanoforming of Pd-based amorphous alloy," *Scripta Materialia*, vol. 44, pp. 1541-1545, May 2001.

[71] Y. Saotome, T. Hatori, T. Zhang, and A. Inoue, "Superplastic micro/nano-formability of La60Al20Ni10Co5Cu5 amorphous alloy in supercooled liquid

state," *Materials Science and Engineering a-Structural Materials Properties Microstructure and Processing*, vol. 304, pp. 716-720, May 2001.

[72] M. S. Lou, J. C. Chen, and C. M. Li, "Surface roughness prediction technique for CNC end-milling," *Journal of Industrial Technology*, vol. 15, 1998.

[73] N. Zhang, J. S. Chu, C. J. Byrne, D. J. Browne, and M. D. Gilchrist, "Replication of micro/nano-scale features by micro injection molding with a bulk metallic glass mold insert," *Journal of Micromechanics and Microengineering*, vol. 22, 2012.

[74] M. Bakkal, A. J. Shih, S. B. McSpadden, C. T. Liu, and R. O. Scattergood, "Light emission, chip morphology, and burr formation in drilling the bulk metallic glass," *International Journal of Machine Tools & Manufacture*, vol. 45, pp. 741-752, Jun 2005.

[75] X. Liu, D. Du, and G. Mourou, "Laser ablation and micromachining with ultrashort laser pulses," *IEEE Journal of Quantum Electronics*, vol. 33, pp. 1706-1716, 1997.

[76] M. Sorescu, "Comparative characterization of the irradiation effects induced in metallic glasses by pulsed laser and alpha particle beams," *Journal of Alloys and Compounds*, vol. 284, pp. 232-236, 1999.

[77] W. Li, R. Minev, S. Dimov, and G. Lalev, "Patterning of amorphous and polycrystalline Ni78B14Si8 with a focused-ion-beam," *Applied Surface Science*, vol. 253, pp. 5404-5410, 2007.

[78] P. V. Petkov, S. S. Dimov, R. M. Minev, and D. T. Pham, "Laser milling: Pulse duration effects on surface integrity," *Proceedings of the Institution of Mechanical Engineers, Part B: Journal of Engineering Manufacture*, vol. 222, pp. 35-45, 2008.

[79] M. F. Ashby, *Materials Selection in Mechanical Design*. Oxford: Pergamon Press, 1992.

[80] http://liquidmetal.com/our-products/product-parts/. (2013, 30/08/13). *What We Sell*.

[81] P. Vettiger, G. Cross, M. Despont, U. Drechsler, U. Durig, B. Gotsmann, W. Haberle, M. A. Lantz, H. E. Rothuizen, R. Stutz, and G. K. Binnig, "The "millipede" - Nanotechnology entering data storage," *Ieee Transactions on Nanotechnology*, vol. 1, pp. 39-55, Mar 2002.

[82] M. Wollgarten, S. Mechler, E. Davidov, N. Wanderka, and M. P. Macht, "Decomposition and crystallization of Pd40Cu30Ni10P20 and Zr46.8Ti8.2Cu7.5Ni10Be27.5 metallic glasses," *Intermetallics*, vol. 12, pp. 1251-1255, 2004.

[83] J. Lendvai, J. Gubicza, J. L. Lábár, and Z. Kuli, "Effect of crystallization on the deformation behavior of a Zr-based bulk metallic glass," *International Journal of Materials Research* vol. 100, pp. 439-442, 2009

[84] D. T. Pham, S. S. Dimov, C. Ji, P. V. Petkov, and T. Dobrev, "Laser milling as a 'rapid' micromanufacturing process," *Proceedings of the Institution of Mechanical Engineers, Part B: Journal of Engineering Manufacture*, vol. 218, pp. 1-7, 2004.

[85] M. Bakkal, T. Liu, C., T. Watkins, R., R. Scattergood, O., and A. Shih, J., "Oxidation and crystallization of Zr-based bulk metallic glass due to machining," *Intermetallics*, vol. 12, pp. 195-204, 2004.

[86] A. Kubler, J. Eckert, A. Gebert, and L. Schultz, "Influence of oxygen on the viscosity of Zr65Al7.5Cu17.5Ni10 metallic glasses in the undercooled liquid region," *Journal of Applied Physics*, vol. 83, pp. 3438-3440, 1998.

[87] J. Lendvai, D. Fátay, and J. Gubicza, "Indentation creep study on a Zr-based bulk metallic glass containing nano-quasicrystals," *Materials Science and Engineering: A*, vol. 483–484, pp. 607-610, 2008.

[88] M. Yan, J. F. Sun, and J. Shen, "Isothermal annealing induced embrittlement of Zr41.25Ti 13.75Ni10Cu12.5Be22.5 bulk metallic glass," *Journal of Alloys and Compounds*, vol. 381, pp. 86-90, 2004.